POLITECNICO
MILANO 1863

SCUOLA DI INGEGNERIA INDUSTRIALE
E DELL'INFORMAZIONE

A fundamental analysis of transport properties of gas diffusion layers in CO_2 electroreduction

TESI DI LAUREA MAGISTRALE IN
CHEMICAL ENGINEERING
INGEGNERIA CHIMICA

Author: **Davide Cavuto**

Student ID: 989934
Advisor: Matteo Maestri
Co-advisor: Kaustav Niyogi
Academic Year: 2022-2023

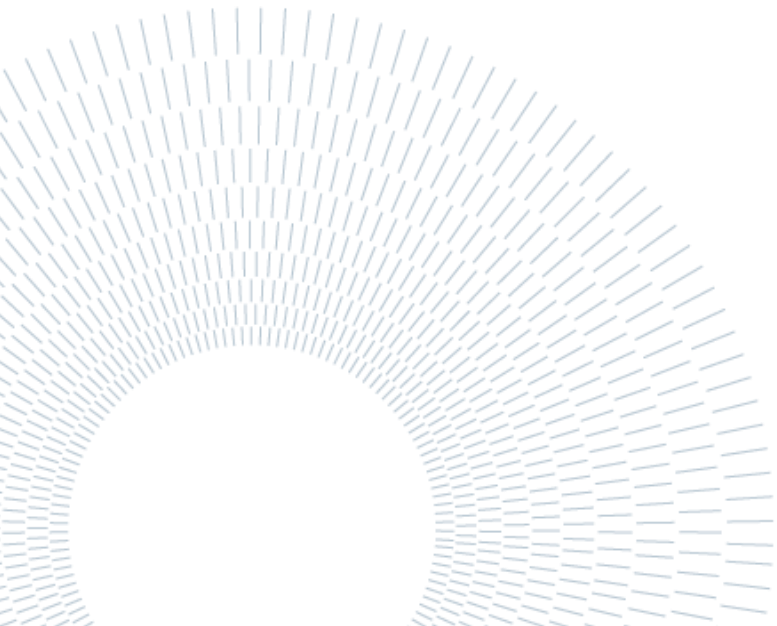

Abstract

CO_2 electroreduction offers a promising route to efficiently produce fuels and chemicals while reducing the burden of greenhouse gas emissions associated with carbon-intensive industrial processes. Among the possible configurations of the electrochemical reactor needed for improving the reduction reaction process economics, the Gas diffusion electrode (GDE) has recently demonstrated superior performance compared to other architectures. Nevertheless, despite the improvement in the maximum current density and product selectivity achieved, there still exist many challenges that prevent vapor-fed CO_2 electrolyzers to be a commercially viable technology. As an example, the structure of gas diffusion layer has to be optimized in order to reduce transport limitations and degradation tendencies such as flooding, that arise when operating the electrolytic cell at high current densities over industrially relevant prolonged duration. Acknowledging this, in this work the transport processes through the gas diffusion layer are investigated by virtually reconstructing a realistic mesoscale geometry of the porous electrode and running computational fluid dynamics simulations on it. The 3D numerical simulations carried out over virtually reconstructed and morphologically validated geometries are used to systematically analyse the effect of microstructural parameters on the transport properties. The simulations reveal that the effective thermal/electrical conductivity ratio in the solid phase and the effective diffusivity ratio in the gas phase can be described exclusively as a function of the porosity of the media. The derived engineering correlations show that empirical correlations for generic porous media such as the Bruggeman correlation, used in the context of gas diffusion electrodes macroscopic modelling, predict inaccurate values of the effective transport properties, especially in the case of diffusivity. Finally, exploiting the concept of hierarchical multiscale modelling, the CFD-derived correlations are integrated in a 1D reactive macroscopic model for CO_2 electroreduction to CO using Ag catalyst. The cell performances predicted using the new transport correlation at high voltage significantly deviates form the results obtained using the Bruggeman correlation, highlighting the importance of using multiscale analysis derived correlations over empirically-derived ones for macroscopic modelling of the electrolyzer cell. The results of this study are particularly relevant in the understanding of gas diffusion layer structure-dependent properties and as such they are helpful when engineering vapor fed electrolyzers.

Key-words: CO_2 electroreduction, Multiscale modelling, Gas diffusion layer, Effective transport properties

Abstract in italiano

L'elettroriduzione della CO_2 costituisce una promettente tecnologia utilizzata per la produzione di carburanti e sostanze chimiche dal valore aggiunto che nel contempo risulti utile a ridurre le emissioni di gas serra provenienti da processi industriali ad alto impatto ambientale. Il reattore elettrochimico dove avviene la reazione di riduzione della CO_2 può essere realizzato in diverse configurazioni. Tra queste, quella con elettrodo a diffusione gassosa (GDE) si dimostra la più performante. Tuttavia, nonostante il miglioramento ottenuto in termini di densità di corrente massima e selettività, l'impiego commerciale di questi reattori è ancora limitato dalla presenza di diverse problematiche. Ad esempio, è importante ottimizzare la struttura del gas diffusion layer per ridurre le limitazioni da trasferimento di materia e il flooding, particolarmente rilevanti quando si opera a densità di corrente elevate per tempi prolungati e rilevanti dal punto di vista industriale. Tenendo a mente ciò, nel seguente studio si analizzano i fenomeni di trasporto che avvengono all'interno del gas diffusion layer, ricostruendo una realistica geometria virtuale del suddetto mezzo poroso e effettuando simulazioni fluidodinamiche su di esso. Le simulazioni numeriche tridimensionali, effettuate sulle geometrie virtuali precedentemente ricostruite e validate, sono usate per analizzare l'effetto dei parametri microstrutturali sulle proprietà di trasporto. I risultati delle simulazioni rivelano che le proprietà di trasporto effettive quali conduttività nel solido e diffusività nel gas, possono essere espresse esclusivamente in funzione della porosità del mezzo. Vengono quindi derivate delle correlazioni ingegneristiche che rivelano come la correlazione di Bruggeman, utilizzata nei modelli macroscopici dei gas diffusion electrodes, fornisca delle previsioni inaccurate delle proprietà di trasporto effetive, specie nel caso della diffusività. Infine, sfruttando un approccio di modellazione multiscala di tipo gerarchico, le correlazioni sono integrate in un modello macroscopico che simula l'elettroriduzione della CO_2 a CO, ottenuta per mezzo di un catalizzatore a base di argento. Quando i risultati ottenuti ad alto voltaggio sono confrontati con le previsioni del modello che implementa le correlazioni di Bruggeman, si notano delle differenze nella quantità di CO prodotta, a prova di come sia importante utilizzare delle correlazioni sviluppate ad-hoc piuttosto che modelli empirici per mezzi porosi. I risultati del seguente studio sono particolarmente utili nella comprensione delle proprietà di trasporto dei gas diffusion layer e, come tali, risultano utili nell'ingegnerizzare electrolyzers a feed gassosa.

Parole chiave: Elettroriduzione della CO_2, Modellazione multiscala, Gas diffusion layer, Proprietà di trasporto effettive

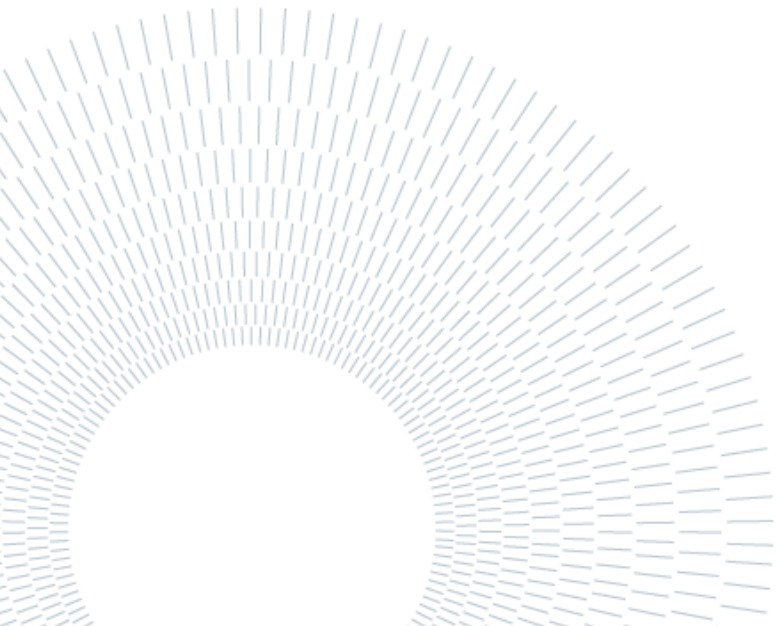

Contents

1 Introduction

Due to the intense exploitation of non-renewable resources readily available in nature, the ecosystem of the planet earth is threatened by increases in the global average temperature far beyond what its homeostasis capacity can sustain. There is scientific consensus in recognizing the cause of this phenomenon in the accumulation of greenhouse gases into the atmosphere, in particular of carbon dioxide. In response to this existential threat to humanity, different actions have been put in place. Notably, the emergence of innovative technologies that effectively mitigate greenhouse gas emissions while concurrently generating fuels and chemicals has gained significant attention. One such technology is CO_2 electroreduction. By targeting point source emissions, primarily from industrial activities, or by capturing and utilizing CO_2 already present in the atmosphere, CO_2 electroreduction offers a valuable means of counterbalancing climate change. Hence, advancing our fundamental understanding of physical and chemical phenomena occurring within CO_2 electrolyzer is of utmost importance to bring it to industrially relevant scales, and will constitute the primary motivation of the current work. Particularly, the gas diffusion layer (GDL), which constitutes an important component of vapor fed CO_2 electrolyzer will be analyzed in its structure- transport property relationship from a fundamental standpoint, meaning that the transport behavior of GDLs will be linked to their microstructural features using numerical modeling and simulations. This work is subdivided as follows.

In the following introduction, a brief perspective on what brought us to the seemingly irreversible circumstances above-mentioned is provided. Being presented as one possible solution, the CO_2 electroreduction technology is introduced and extensively discussed in different aspects (reactor configurations, gas diffusion electrode, working principles, gas diffusion layer manufacturing). The introductory part is concluded explaining how the principles of multiscale modeling and hierarchical approach, constituting the methodologies employed by the current work, can benefit the fundamental understanding of the gas diffusion electrodes. The motivation section follows, where the remaining challenges of CO_2 electrolysis are reviewed. With respect to these challenges it is clarified the relevance of carrying out the numerical study

conducted. Then, in the theoretical background section, the physical-chemical principles governing electrolytic cell are covered. Transport phenomena digressions will cover the main part of the conducted work while thermodynamics and reaction kinetics features will mainly address important concepts needed in the macroscopic modeling of electrochemical systems. In the methods section, the details of the followed numerical procedure are thoroughly discussed with a focus on how the geometries are created, validated and used for deriving the sought correlations. Details on the macroscopic model used for testing the correlations are also discussed. At last, in the results section, the output of the applied methodology is unveiled. The findings are commented and compared with the existing literature results, highlighting the limitations and the strengths of the conducted work.

1.1. The big picture

1.1.1. How did we end up here

With the purpose of reconstructing the history of the complex relationship between energy and its harnessing by humanity, one may get discouraged by the words of the Nobel Prize Richard P. Feynman on what energy actually is: "It is important to realize that in physics today, we have no knowledge of what energy is" [1]. Fortunately, energy does not require to be fully understood in order to be used. Indeed if this was not the case we would not use it on a daily basis. What we have learnt (and what we are still learning) thanks to its manifestations, is to formulate some laws about its properties (e.g. conservation and degradation) which then helps us in designing methods to convert energy from one form to another. After all, men's ability of transforming energy has been long recognized as a metric for civilization progress [2].

Concerning energy conversion capabilities and to prove how much this factor is important in driving the dynamics of societal evolution, Vaclav Smil in his inspiring book "*How The World Really Works*" conceives a mental experiment [3]. He imagines an extraterrestrial civilization visiting the earth every time "something interesting happens", which is, every time humans learn how to convert and use a new form of energy. Playing this game, it turns out that first traces of fossil fuels consumption (apart from biomass) date back to the beginning of the 17th century, by the united kingdom which started to use coal for heating purposes. The situation was more or less stagnant for approximately two centuries and a half. In fact, by 1850 only 7% of the energy consumption was obtained

by coal (the remaining being obtained by draft animals, human muscles and waterwheels/windmills). The coal powered steam engine then started to slowly spread, and by 1900 (in just 50 years) half of the primary energy was provided by coal. Continuing the escalation, by 1950, the 75% of the primary energy is provided by fossil fuels and nowadays, this amount is stabilized around this percentage (say the total energy consumption increases but this is due to both renewable and non-renewable sources increasing exploitation). These trends can be visualized in Figure 1.1, where the relative quotas of the different energy sources employed are reported [4].

Of course, in terms of absolute consumption there were no less drastic changes. In 2021, the total primary energy consumption was estimated to be 176431 TWh, compared with 5653 TWh of the pre-industrial level [4]. If per capita figures are considered, assuming a population of approximately 1 billion people in 1800 [5] and 8 billion in 2021, we get a change in primary energy utilized per capita from about 20 to 80 GJ/capita.

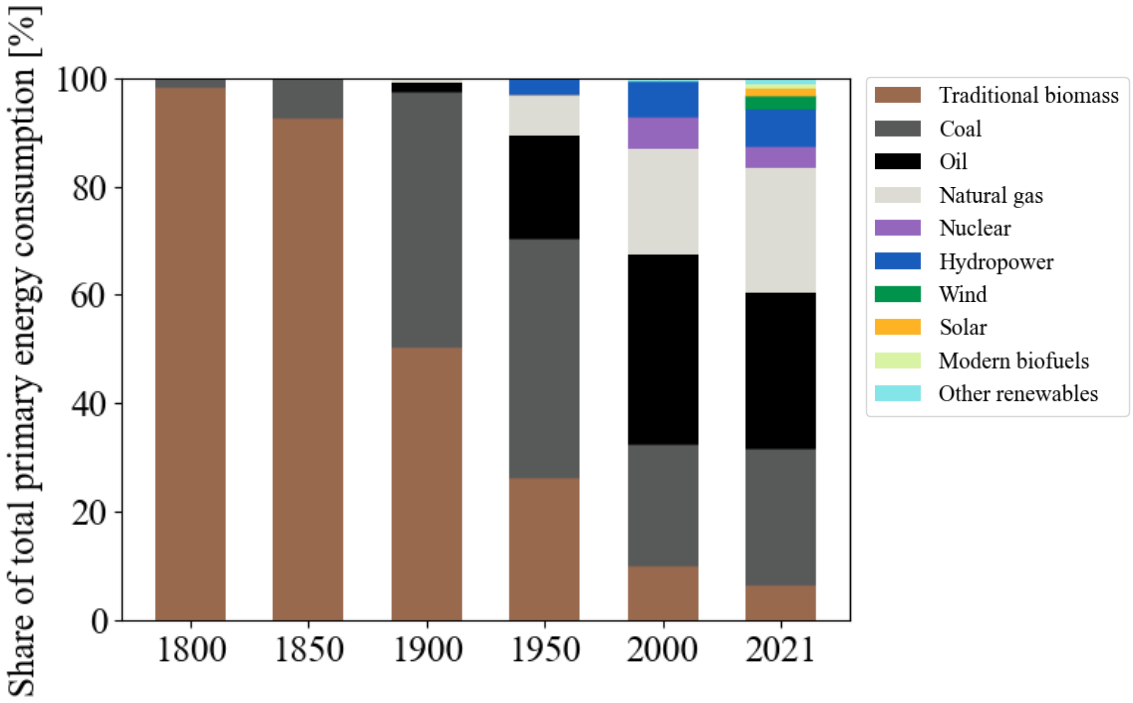

Figure 1.1 Global primary energy consumption by source, from pre-industrial to modern era. Adapted from *[4]*.

The discrepancy would get even larger if we consider rather than primary energy (which does not take into account energy conversion losses), the actual useful energy (remaining energy after its conversion in to an useful form, e.g. heat, electricity, mechanical work and so on). This effect is due to the fact that our ability of efficiently

converting energy from one form to another, a process which by the second law of thermodynamics is associated to unavoidable losses, has improved through the years, going from rudimental stoves and steam engines, to modern gas and steam turbines (simply stated today we can extract more useful energy from a fixed amount of primary energy than we could at the beginning of the industrial revolution).

A question arising spontaneously now is, how are we using this energy, what are the energy sinks of the modern society ?

In simple terms, energy has been the key ingredient, together with human ingenuity, for improving the total material wealth and well-being of humanity. Reduction in the hours of physical labor, longer times for leisure, better and variegated eating, mass-scale travel and transport, instant communication and advanced medical treatments are just few of the many advancements that without an intensive energetic exploitation would not have been possible. Today we have also a quantitative proof of how energy consumption affects the quality of life. For instance, Fragaszy et al. [6], correlated the Human Development Index (HDI), a metric drafted by the United Nations for measuring the quality of life taking into account life expectancy, education and the gross national income per capita, with power utilization (kW) per capita (Figure 1.2). The figure clearly shows a positive correlation between well-being and energy consumed by a community.

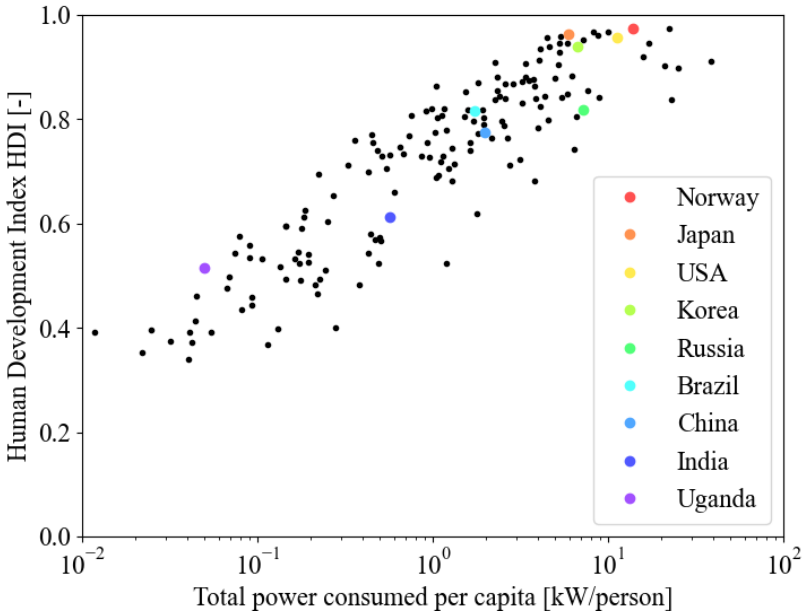

Figure 1.2 Human Development Index vs power consumption per capita. The communities which consumes higher amount of energy are unequivocally wealthier. Adapted from *[6]*.

Other works try to develop indices on their own, e.g. Cesar et al. [7], define a quality of life index on the basis of variables affected by energy consumption but not directly determined by it, such as Improved Water Access, Life Expectancy at Birth, Infant Mortality Rate and Mean Years of Schooling.

Whatever the metric being used, the results are quite explicative. Planet earth provides us with plenty (but limited) resources, and as the dominant inhabitants of it, humans have had the natural tendency of exploiting these assets for a better living, with all the consequences on the environment that this behavior is responsible for. Even if the main concern here is about environmental issues, these cannot be decoupled from the other two of the three pillars of sustainability [8] as environmental sustainability for sure has an effect on economic and social sustainability.

In this scenario, to analyze the possibility of counteracting this tendency from an engineering perspective, it may be possible to make use of the Kaya identity [9], a simple equation used to analyze the factors that contribute to changes in carbon dioxide emissions. According to Equation 1.1 in fact, as far as population and wealth growth are considered, the only way emissions can be reduced, is by reducing the last term, related to the CO_2 emitted per energy unit produced.

$$CO_2 = Population \frac{Energy}{Population} \frac{CO_2}{Energy} \tag{1.1}$$

As a consequence, to decrease this term it is possible both to improve the efficiency of energy conversion systems and to increase the share of renewable energy in the so called energy mix. Nevertheless, using renewable energy sources comes with nontrivial challenges as their "low densities of power […], together with their stochasticity, imply the introduction of renewed approaches to the use of energy" [10]. Trying to accomplish this goal, say trying to find new ways to "treat" energy, is, without any doubt, one of the most complex tasks humankind has ever faced.

1.1.2. Nature does not help

Up to now we got a sense on why the worldwide energy consumption has vertiginously increased from preindustrial levels, but we have not yet clarified why this energy surplus have come from fossils. What makes them so appealing ? The answer comes from an interplay of factors, we will now briefly analyze.

Before coal, the main fuels used for addressing the primary needs of humans were biomass derived. Coal was readily available for being burnt, but its first utilizations (even before the industrial revolution) led to concerns about its detrimental health effects which eventually delayed its adoption [11]. Then, as a direct consequence of the population growth, wood shortage obliged advanced countries as UK to give a second chance to fossils, and this decision was crucial in changing the scenario of many aspects of industrial activities, iron making and transportations just to cite some. For transportation purposes, coal was particularly appealing for its high energy density. A quick comparison of Higher Heating Value (HHV) between the most common energy carriers will now clarify why fossils dominate in this sense (Table 1). By looking at the table it is straightforward to understand why coal originally substituted biomass for transatlantic crossing, and why nowadays there are no natural gas or battery-powered flight (even though batteries are not included in the table, please consider that in 2020, Li-ion batteries had a volumetric energy density around 1620 MJ/m^3 [12]).

Table 1 Energy density for common fuels *[13]*.

	Hydrogen	**Natural gas**	**Gasoline**	**Kerosene**	**Diesel**	**Coal**	**Wood**
Density [kg/m^3]	0.09	0.747	744	790	836	800-900	600-900
HHV [MJ/kg]	142.2	54	46.5	46.4	45.8	24-35	20
HHV [MJ/m^3]	12.8	40.3	34596	36656	38288	19200-31500	12000-18000
Aggregation state @NTP	G	G	L	L	L	S	S

Despite the fact that oil-derived fuels are more energetic than coal, the main reasons that contributed to the success of the former energy carriers are in turns their aggregation state, the ease of production (especially if compared with coal), storing and transportation (as liquids can be easily pumped through mile-long pipelines without employing human labor) [3]. In this, the expansion of the transportation services and the invention of the internal combustion engine played a paramount role as it is made clear by Carrà "the marriage between oil and cars […] generated the biggest productive activity present on the planet, which is oil refining" [10]. Also, we can think on how easily we can access to useful energy using these sources. How easily we can convert the

chemical energy within them, in more practical forms of energy like heat and mechanical work. The result is that, as in the words of Prof. Thomas F. Jaramillo of the Stanford University, "We have to remember this key set of attributes, really, any future energy technology needs to compete with this. If it doesn't it is going to be a tall order to get a massive shift in the right direction" [14].

Ultimately, the wide variety of non energy-related products that can be obtained by coupling oil refinery and petrochemical processes have strongly contributed to the development of the oil & gas industry. The International Energy Agency (IEA) estimates that the chemical and petrochemical industry accounts for 14% (13 million barrels per day) and 8% (300 billion cubic meters) of the total primary demand for oil and natural gas respectively [15]. So in fact, as pointed out by the IEA itself in the report, it is not wise to consider these products as decoupled from the energy consumption. Raw materials embody energy within them and through their utilization we are literally consuming energy: "The essential truth missing from economic education is that energy is the stuff of the universe, that all matter is also a form of energy, and that the economic system is essentially a system for extracting, processing and transforming energy as resources into energy embodied in products and services." [16]. Accordingly, the material wells associated to the former activities take the names of plastics, fertilizers, fibers, detergents, dyes, resins, rubber, paints & coatings, adhesives, pesticides and so on [17].

Witnessing the wonders of coal, oil and natural gas, we may think to blame nature for having provided us with such polyvalent but at the same time controversial means, we may end up saying that nature does not help. But is this really the objective truth ? Have fossils been the only viable path for securing the high living standards we are used to in the 21st century, and if so, are fossils still the unique solution for maintaining and improving them? We are presently exploring possible solutions to provide an answer. What we know for sure, is that "The high degree of the global dependence on fossil carbon and the enormous scale of the fuel-dominated global energy system mean that the unfolding energy transition […] will be a gradual, prolonged affair" [18], that is, the timescale of this transition will be comparable to those of the transitions we have mentioned in chapter 1.1.1. But at least, do we have a starting point for where to look for our solutions?

1.1.3. The sun as the prime mover

The earth can be considered from a thermodynamic point of view an open system with respect to energy, meaning that energy is allowed to enter and escape from it. Earth

is constantly subjected to an incoming energy flux from the sun, the solar constant, roughly equal to 1367.5 W/m^2 ($\pm$ 4% to account for seasonal changes) [19]. Nevertheless if we want this value to be averaged on the total earth surface, it must be cut down at first due the spherical shape of the earth, meaning that the radiation strikes its surface from different angles and then by the fact that only half of the globe is lit. Doing the computation we get a value of 340 W/m^2, correspondent to 170000 TW ca. Part of this power is further curtailed (by the presence of the atmosphere) so that a fraction of it actually reaches the sea level. There, plants and cyanobacteria absorb 90 TW ca, to perform photosynthesis, responsible for carbon fixation in the form of sugars and for oxygen evolution [10].

With so much energy at stake, it is fair to state that our expertise in extracting energy from the sun will constitute one milestone in our path for decarbonizing anthropic activities. In a seminar on catalysis for sustainable energy, Jens Nørskov, professor of catalysis at the Technical University of Denmark, states clearly that if we want somehow to store the energy incoming from the sun, "by far the most efficient way of storing it is by storing it in chemical bonds" [20]. He also points out that, all in all, that is what nature has done by herself in millions of years for producing fossil fuels.

Once organisms capable of fixing carbon like some species of bacteria, freshwater algae and higher land plants die, the resulting biomass is deposited in anaerobic bottom water of deep lakes. The macromolecules that once constituted these organisms are degraded into their corresponding monomeric units, which being not stable, are transformed by bacterial enzymes into polymer-like materials as humic substances. These substances then get converted in kerogen, a solid organic matter made up of polycondensed aromatic rings with lateral aliphatic chains. Oil and gas are then the result of the thermal degradation of kerogen, which mainly consist in driving, thanks to high temperatures beneath the ground (80-150°C), cracking reactions of the mentioned structure [21].

We arrive then to a crucial point of the discussion. Nature has provided us with a framework for fuels production (see Figure 1.3). The raw materials are water and carbon dioxide which, by coincidence, it is also the "bad" molecule to be removed. It is up to us and our creativity, to take this process and profoundly alter the transformations involved, making sure they take few minutes rather than millions of years. Finding the ideal candidate for the black box content would imply at first terminating our long lasting reliance on fossil fuels and at second capturing and fixing carbon in its most oxidized state, decreasing the burden of greenhouse gases emissions in to the atmosphere.

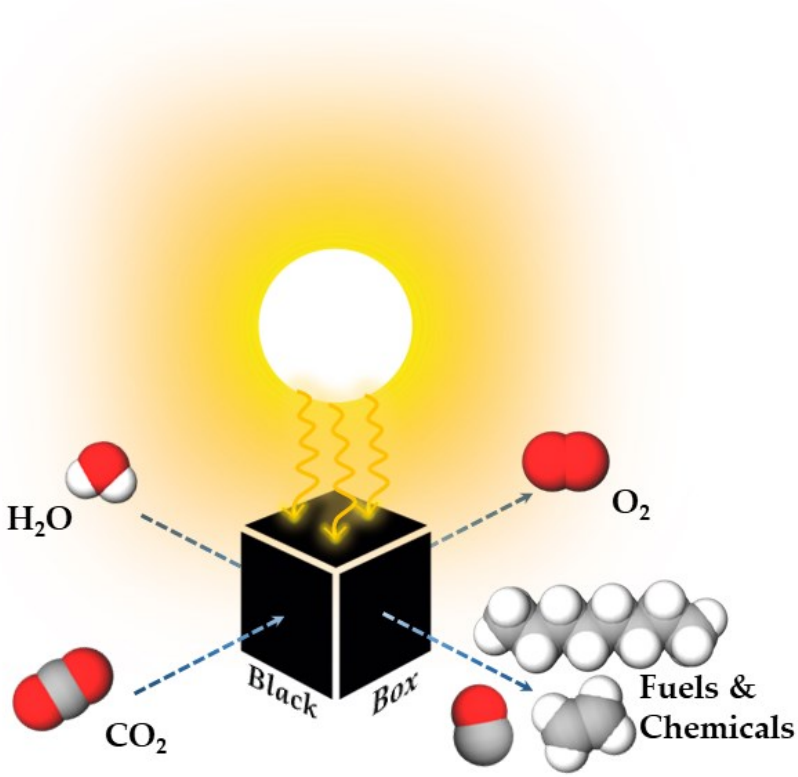

Figure 1.3 Black Box: the elementary framework provided by nature for CO_2 conversion.

Thinking to oil and more in general to fossils as being englobed in the control volume of a material balance it is clear that, due to finiteness of fossils reserves and since the rate at which the fossils are formed is significantly lower than the rate at which they are extracted and used, these assets at our disposal are facing a relentless depletion (after all this is the definition of non-renewable energy source). To address this issue, it is necessary to focus on the production rate and make significant changes to its time scales.

When such changes of time scales are required, catalysis engineering may help in finding a viable path for activating carbon dioxide.

1.1.4. Shrinking time scales with catalysis

As defined by the Nobel prize Wilhelm Ostwald, a catalyst is a substance which changes the reaction rate of a chemical transformation, without being consumed during the process [22]. The working principle of catalysts can be conveniently compared to that of a printing press, "A printing press takes in reactant, paper and ink, goes through a

cycle of steps, and produces a product: a printed page. The printing press is not changed during the process" [23]. Actually, even if it is not of primary concern for this work, we know that as printing press gets ruined over time, also catalysts, heterogeneous ones in particular, face deactivation during their operational lifetime.

In chemical reactions the observed effects deriving from the utilization of catalysts are typically reduction in activation barriers, with consequent increase in the reaction rate, fixed certain operating conditions. We talk then of homogeneous and catalytic pathways as different paths across the potential energy surface (PES), that link reactants to products (Figure 1.4).

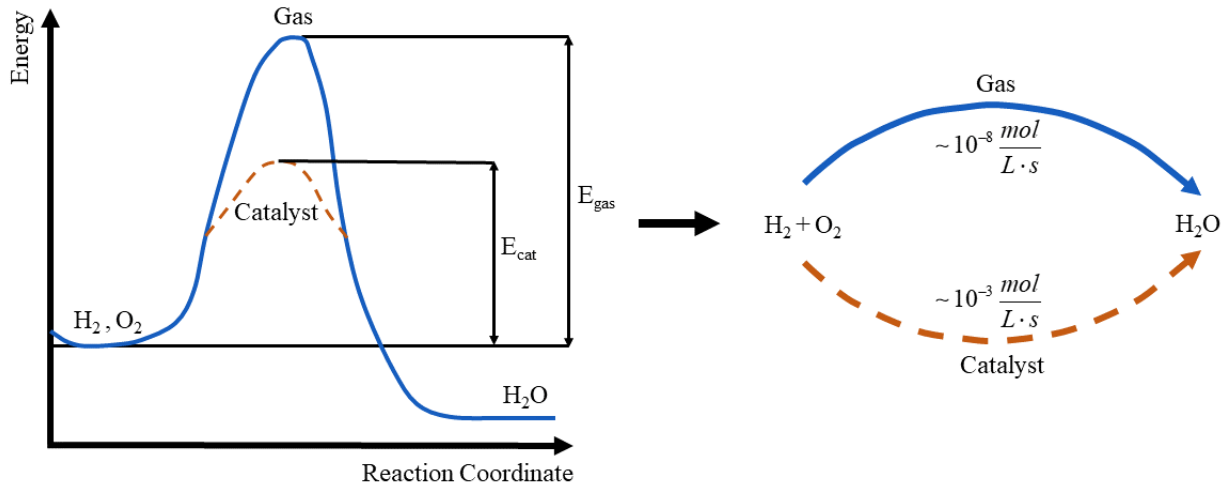

Figure 1.4 Different reaction pathways for hydrogen oxidation. Adapted from *[124]*, rate values taken from *[23]* at 780 K.

In the case of carbon dioxide, the interest is in reducing carbon from its most oxidized state (+4), to higher energy products. Reduction is readily translated in a transfer of electrons into the carbon atom. Many catalytic pathways are available for achieving this goal. From a taxonomical point of view, they can all be classified in the following categories [24]:

- Thermal activation of CO_2 on metal sites;
- Thermal activation of CO_2 on acid/base sites;
- Photochemical activation of CO_2;
- Plasma activation of CO_2;

- Electrochemical activation of CO_2.

Among these, our focus is upon the last category, in particular on the CO_2 electrocatalytic reduction reaction. The reasons why the latest method is attractive from an industrial point of view are multiple: it can be conducted at ambient conditions, the electrons are directly used for product formation and it is versatile both in terms of scaling-up (as distributed systems) and of range of products formed [25]. At the same time, major challenges need to be solved before this technology reaches the industrially relevant technology readiness level.

An important message to be conveyed at this stage, is that none of the mentioned 5 pathways alone, with the underlying technologies, will constitute the final and unique solution for capturing and recycling CO_2. In fact, in order to reduce and eventually close the gap between climate goals (e.g. Paris Agreement) and emissions, "A mix of technology and policy options" [26] will be of vital importance. Therefore, we believe that is important to create and spread the consciousness that CO_2 electroreduction will be just a small, yet important piece of the bigger puzzle of the net zero goal.

1.2. CO_2 electroreduction

It is a good moment for unveiling the content of the black box previously mentioned, as from now on it will consist of a carbon dioxide electrolyzer.

1.2.1. CO_2 recycling in the net zero paradigm and economics

According to the international energy agency (IEA), the goal of net zero emissions by 2050 can be achieved relying on the following key pillars of decarbonization [27]:

- Energy efficiency: in the buildings (in terms of heating, cooling and appliances energy consumption), transport (in terms of average fuel consumption) and industrial sectors;
- Behavioral change: as active and willing participation of citizens in developing sustainable attitudes and supporting low-carbon technologies;

- Electrification: by directly using low-emissions electricity in place of fossil fuels in transportation (where possible) industry (e.g. electric arc furnace for steel production) and buildings (e.g. heat pumps);
- Renewables: through an almost complete substitution of fossil power generation with solar, wind and dispatchable renewables (hydropower, bioenergy, concentrating solar power and geothermal);
- Hydrogen and hydrogen-based fuels: by initially leveraging on the existing uses of fossil energy with ready infrastructures (e.g. refineries and power plants) and then by an expansion across all end-uses;
- Bioenergy: by employing sustainable sources without negatively impacting biodiversity, for electricity generation, district heat production and high temperature heat production in industry;
- Carbon capture, utilization and storage: by tackling emissions from existing assets, in particular for addressing emissions from the most challenging sectors and by allowing for CO_2 removal from the atmosphere.

In this paradigm, "CO2 recycling can enable the storage of renewable electricity from intermittent sources in a dense and versatile form, provide a renewable carbon feedstock to chemical industries, and add value to CO2 captured at industrial point sources or directly from the air " [28]. This is the idea behind the utilization of CO_2 electrolyzers, located in the broader context of CO_2 recycling technologies (Figure 1.5).

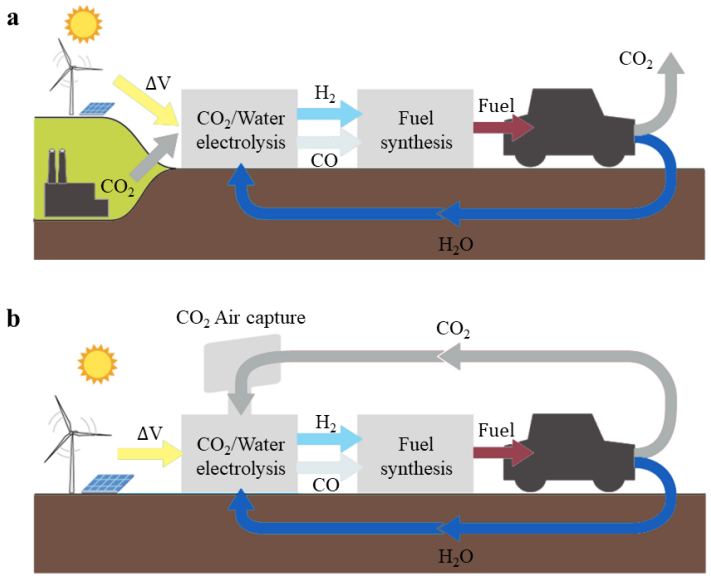

Figure 1.5 CO2 recycling with electrochemical reactors. **a**, From industrial point sources **b**, From direct air capture. Adapted from *[126]*.

Electrochemical reduction of CO2 combines the electrochemical water splitting and subsequent thermal hydrogenation into a single electrochemical process, avoiding also the harsh conditions of temperature and pressure of thermal systems. The consequences are that electrochemical reactions are more suitable to decentralization than the thermal counterparts, and that they can enable rapid on-off switch, as well as rapid change in the production rate, according to the electricity made available from volatile power sources [29].

The versatility, is finally exemplified through the wide range of products that can be synthetized following this route. In Figure 1.5, only one of the possible products is shown (carbon monoxide, coupled with water electrolysis to obtain syngas, from where the organic chemistry is reconstructed). Other chemicals obtained in previous studies (formic acid, methane, ethylene, ethanol, n-propanol, acetaldehyde, propionaldehyde, acetic acid, methanol, ethylene [30]) are reported together with their CO_2 electrochemical reduction reaction, number of electrons required and standard reduction potential in Table 2.

Now, even though it is not one of the main objectives of the current study, analyzing the economic feasibility for the production processes of some of the mentioned product may help to provide a complete and more importantly realistic vision of the technology considered.

That said, it is worth to discuss the results of an economic study [28], that no matter how much concise, gives important indications on future directions to explore.

The starting premise is very simple and it also constitutes the essence of chemical engineering, whose main aim is adding value to raw materials.

A process can be considered economically viable if the products obtained by its operation are more valuable than what has been paid for the raw materials (and for running the process itself). Starting from this principle, assumptions are made and data are collected to quantify the figures (costs and prices) relevant to the study. The accuracy of the predictions are function of the plausibility of the hypotheses formulated and the quality of the collected data.

The main assumption underlying the results about to be presented, is that the cost of producing the chemicals are exclusively due to the expenditures related to the capture of CO_2 (which is the raw material) and of the electrical energy consumption (taken from renewable sources). Simply stated, capital costs are neglected and the products obtained are pure. The assumptions are strong of course, because it is well known that the figure related to the purchase of an electrochemical reactors is one of the main impacting [25].

Table 2 Most reported CO2 electroreduction products, their reaction and standard reduction potential.

Name	Reaction	n e-	Standard reduction potential vs RHE [28]
Carbon monoxide	$CO_2 + 2H^+ + 2e^- \rightleftharpoons CO_{(g)} + H_2O$	2	-0.10
Formic acid	$CO_2 + 2H^+ + 2e^- \rightleftharpoons HCOOH_{(aq)}$	2	-0.12
Methanol	$CO_2 + 6H^+ + 6e^- \rightleftharpoons CH_3OH_{(aq)} + H_2O$	6	0.03
Methane	$CO_2 + 8H^+ + 8e^- \rightleftharpoons CH_{4(g)} + 2H_2O$	8	0.17
Acetic acid	$2CO_2 + 8H^+ + 8e^- \rightleftharpoons CH_3COOH_{(aq)} + 2H_2O$	8	0.11
Acetaldehyde	$2CO_2 + 10H^+ + 10e^- \rightleftharpoons CH_3CHO_{(aq)} + 3H_2O$	10	0.06
Ethylene	$2CO_2 + 12H^+ + 12e^- \rightleftharpoons C_2H_{4(g)} + 4H_2O$	12	0.08
Ethanol	$2CO_2 + 12H^+ + 12e^- \rightleftharpoons C_2H_5OH_{(aq)} + 3H_2O$	12	0.09
Propionaldehyde	$3CO_2 + 16H^+ + 16e^- \rightleftharpoons C_2H_5CHO_{(aq)} + 5H_2O$	16	0.09
n-propanol	$3CO_2 + 18H^+ + 18e^- \rightleftharpoons C_3H_7OH_{(aq)} + 5H_2O$	18	0.10

Moreover, the selectivity towards many of the products listed (especially C_{2+}) [31] is still limited.

Having clarified the nature of the following calculations, the cost of the process in dollars per ton of carbon captured can be approximated with the line of Equation 1.2.

$$Cost\left[\frac{USD}{t_C}\right] = Capture\ Cost + Energy\ \text{cost} \cdot Energy\ content \qquad 1.2$$

having expressed the energy cost in USD/MWh and the energy content in MWh/t_C.

At the time of the study, the carbon capture cost and the cost of electricity from renewable sources were assumed to be of 200 USD/t_C and 50 USD/MWh respectively. Once the data on the energy content and market sizes of the different product are collected, the economic analysis is performed in a very practical way by summarizing the results as seen in Figure 1.6.

Each product is identified on the chart by a set of two coordinates, namely its energy content (x axis) and its price (y axis). The size of the markers represent the market

sizes of the products considered and since they span 4 order of magnitude (from 5.375 Gt_C/y for coal to 0.00012 Gt_C/y for n-propanol) logarithmic scale has been applied to allow for proper visualization.

As far as only the black dashed line is considered, the chart is split in two parts. For the products below the line, their production with CO_2 electrolysis is not economically feasible as their energy content is relatively high, and mostly because of their low price (due to their high availability). The products above the black dashed line instead can be produced with CO_2 electrochemical reduction to obtain a revenue. Among them, ethanol and ethylene are the most interesting for the implementation of mass scale carbon recycling, due to their market size.

The idea is that also other chemicals, here referred to as fine chemicals, as n-propanol and formic acid are economically favourable, but their modest market size prohibits any large scale implementation developed on purpose for recycling gigatons of CO_2.

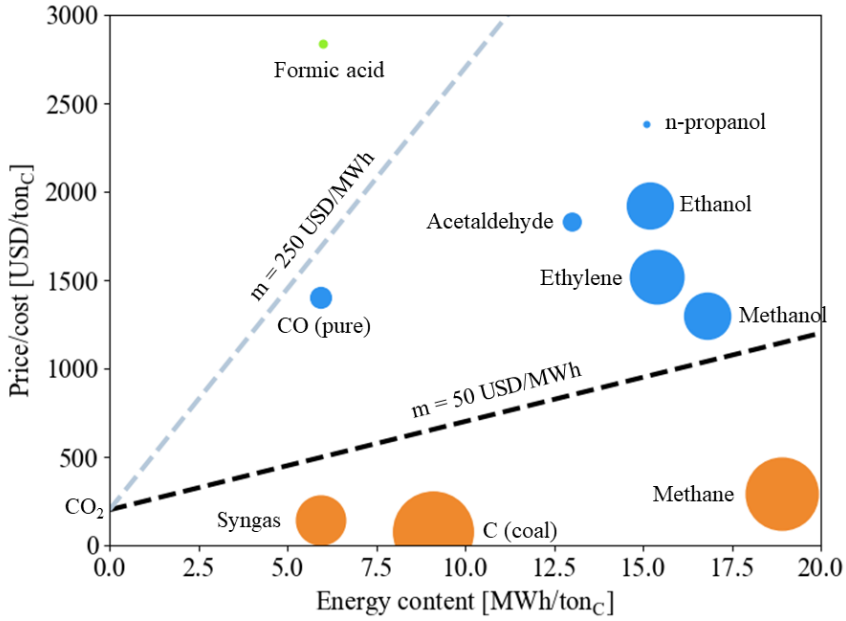

Figure 1.6 Economic analysis. Cost and revenues obtained by producing selected products from CO_2 electroreduction. Black and grey dashed lines are referred to an electricity cost of 50 and 250 USD/MWh respectively. Adapted from *[28]*.

The study dates back to 2019. As an exercise, the cost of electricity has been updated to 250 $/MWh, the Italian 2022 first semester price [32] (the average in the EU was instead 180 $/MWh). The grey dashed line is obtained, showing how the chemicals,

with the only exception of formic acid, are not economically producible. The latter result suggest that, as expected, the feasibility of recycling CO_2 with electrochemical methods strongly depends on our ability to procure cheap renewable electric energy.

As said at the beginning, the conducted study does not take into account major cost figures such as CAPEX and separation costs. Despite this, it is still useful to get important insights on the economics of the process. After all, a legitimate conclusion is that if a product is not economically sustainable under these assumptions, it will be even less when accounting for all the owed expenses.

1.2.2. CO_2 electrolysis, basic traits

In electrochemical systems, whether considering devices utilized for generating electricity (i.e. galvanic cells), or ones used for driving electrochemical reactions through an external electrical power output (i.e. electrolyzers), some indispensable recurring components can be identified. Even if CO_2 electrolyzers make no exception, different configurations of this system can be encountered depending on the application. Therefore in describing these reactors it may be useful to start from their simplest set-up in order to identify and describe the roles of the different components in the most intuitive fashion.

In Figure 1.7 the standard configuration of a CO_2 electrolyzer (the so called H-cell) is reported.

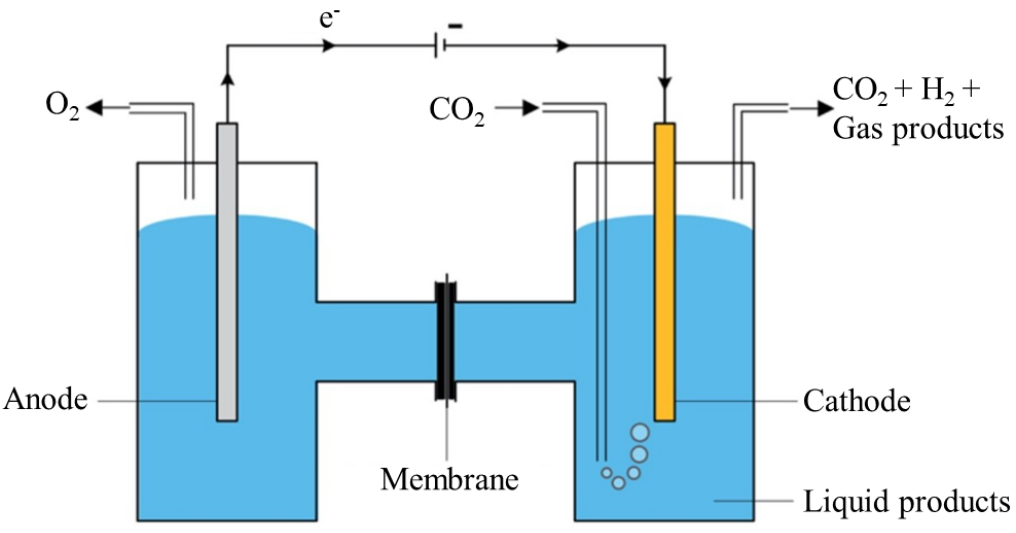

Figure 1.7 CO2 electrolyzer. H-Cell configuration. Adapted from *[35]*.

This configuration is typically used in lab-scale reactors for experimental tests (e.g. testing new electrocatalysts and deriving kinetic data). It barely consists of two metal plates functioning as electrodes for performing the half-cell reactions. The electrodes (cathode and anode) are submerged in electrolytic solutions and are connected electrically through an external circuit consisting of a voltage supply. The electrolytic solution in the tow chambers are not brought in direct contact between them, instead there is a separating membrane (traditionally named salt bridge) which selectively allows ions to cross the two chambers and maintain electroneutrality.

The system works as follows: the gaseous CO_2 is bubbled inside the cathodic chamber and the external power supply establishes a fixed voltage between the two metal plates. The gas is dissolved inside the aqueous solution according to its solubility. After being dissolved it migrates towards the surface of the cathode where a surface reaction occurs. In particular CO_2 is reduced according to the following reactions:

$$xCO_2 + nH^+ + ne^- \rightleftharpoons product + yH_2O \quad 1.3$$

$$xCO_2 + yH_2O + ne^- \rightleftharpoons product + nOH^- \quad 1.4$$

One of the two reactions will predominantly occur according to the choice of the electrolyte, which in turn determines, together with the voltage, the pH of the solution (Equation 1.3 if acidic media is selected, Equation 1.4 otherwise). The ions produced (H^+ or OH^-) will cross the membrane and react on the surface of the anode to be oxidized according to the Oxygen Evolution Reactions (OER):

$$yH_2O \rightleftharpoons \frac{y}{2}O_2 + 2yH^+ + 2ye^- \quad 1.5$$

$$nOH^- \rightleftharpoons \frac{n}{4}O_2 + \frac{n}{2}H_2O + ne^- \quad 1.6$$

The electrons obtained are then transferred by the external circuit towards the cathode in order to further reduce the CO_2.

The system as-described appears to be relatively simple but as soon as a more careful inspection is provided, many phenomena occurring simultaneously are recognized in determining the behavior of the system, making the modeling, and even

before it, the understanding of these systems, arguably complex. The driving forces behind a reaction are dictated by the thermodynamic properties of the electrodes and electrolyte. The reaction rate at the interface, in response to these driving forces, relies on kinetic rate parameters. Furthermore, the transportation of mass through the electrolyte is necessary to deliver reactants to the interface, while electrons must traverse the electrodes [33].

The complexity of the system is further increased when advanced design of the cells are taken into consideration. At first it should be noted that H-cells work typically in a semi-batch configuration, which, evidently, are not suitable for the industrial purposes described in the paragraph 1.2.1. Therefore a switch to continuous operations is needed. The latter statement seems particularly reasonable if considering that the scale-up of flow cells has been already validated in the past with fuel cells and water electrolyzers [34]. Analyzing the realm of continuous electrolyzers, some of the configurations currently available as the result of several years of engineering are those reported in Figure 1.8.

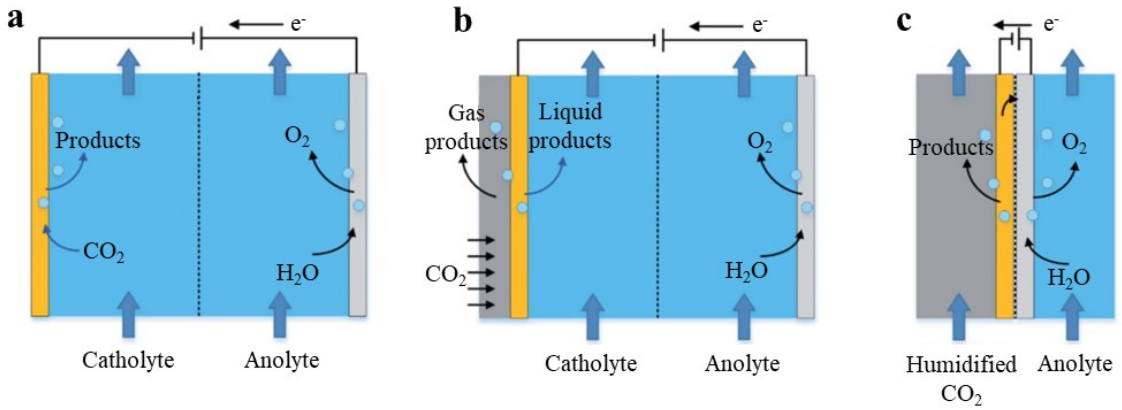

Figure 1.8 CO2 electrolyzer, flow cell set-up. **a**, Two-chamber liquid-fed **b**, Two-chamber liquid-fed with gas diffusion electrode **c**, Vapor-fed zero-gap cell . Adapted from *[35]*.

In the two-chamber liquid-fed cell (Figure 1.8 **a**) the CO2 enters the system as dissolved gas in the catholyte (which has been saturated outside the cell [35]). The two electrolytes are separated by a membrane which as depicted before, allows ion exchange between the two chambers to maintain electroneutrality. The two electrodes are constituted by bare metal plates, also called planar electrodes.

In the two-chamber liquid-fed cell (Figure 1.8 **b**) the carbon dioxide is directly fed with a gaseous stream, which crossing a Gas Diffusion Layer (GDL, not shown in the picture) reacts on the surface of the cathode after having dissolved in the liquid. Even if

more insights on this will be given in chapter 1.2.4, it is not premature to anticipate that what has been just presented is a description of the typical triple-phase boundaries this kind of system give rise to [28]. In this case the triple-phase boundary consists of gaseous CO2, solid electrode (with catalyst upon it) and liquid electrolyte and for this configuration, where the gas diffusion layer and the electrocatalyst are in intimate contact, the assembly takes the name of Gas Diffusion Electrode (GDE).

Another type of GDE is also present in the vapor-fed zero-gap cell (Figure 1.8 **c**), where the catholyte has been completely removed by introducing an Ionic Exchange Membrane (IEM). In this last configuration, the triple-phase boundary is constituted by the gaseous CO_2, the solid catalyst and the ion conducting polymer. As seen in the related figure, the catholyte enters the system in the gas phase, together with the carbon dioxide which is now humidified (the purpose of humidifying the gas is that of keeping the membrane hydrate).

For how these systems have been described, it is quite clear how the complexity of the design causes it to depart from the originally conceived H-cell. In this sense, as far as the three configurations just shown are concerned, the two-chamber liquid-fed cell represents the simplest one while the latter two systems employing a GDE represent the attempts in engineering the flow cell for overcoming the limitations of the former. Since the research efforts in moving in this direction have been fruitful [36], it is worth to further investigate GDEs first of all by understanding the limitations they have been capable to overcome.

1.2.3. Gas diffusion electrode, structure

One of the Key Performance Indicator (KPI) of the electrolysis processes is the partial current density associated to the product of interest. As will be extensively discussed in the chapter 3.4, the partial current density is just a measure of the amount of product obtained when applying a potential difference to the cell (in particular there is a direct relation between the partial current density of a species and its rate of reaction). Since the product of the voltage applied and the current passing inside the cell is a measure of the electrical power the device is draining, it is a necessity to get the highest partial current density (say, the highest amount of product formed) given a certain potential difference applied. So this KPI needs to be maximized. What is in between the voltage and the current density is the total resistance provided by the cell, determined by its thermodynamics, kinetics and transport limitations.

As said previously, in the two-chamber liquid-fed cell, planar electrodes are usually employed, meaning that two simple metal plates are immersed in the liquid solutions. Despite the versatility, which is ideal for rapid and cost-effective experimental tests, the maximum current densities achievable with this set-up are significantly limited [37]. In practice, as discussed before, CO_2 has to be first dissolved in the aqueous electrolyte and then has to move towards the surface of the electrode where it is finally consumed. This is a typical example of transport and reaction in series, where the final rate of CO_2 electrochemical consumption is assumed to be equal to the rate of the slowest process of the series. This means that as soon as the reaction rate (or equivalently the current density) is increased by leveraging on higher voltages, the supply of the dissolved CO_2, say the sum of convective and diffusive fluxes, must be high enough to replenish its concentration on the reactive surface. Evidently the latter condition is not satisfied, due to the poor mass transport to the cathode surface due to the low solubility and diffusivity of CO_2 in water combined with the significant thickness of the mass-transfer boundary layers (60 to 160 μm) [38]. In these conditions the current densities achieved are below 30 mA/cm^2, while the industrial requirement is deemed to be at least 200 mA/cm^2 [39].

A promising solution to this lack of performance is provided by the adoption of gas diffusion electrodes, with which one order of magnitude higher current densities have been obtained [40]. In Figure 1.9 a schematic of the cathode of the CO_2 electrolyzer in the GDE configuration is shown.

GDE are composed of a gas diffusion layer and a catalyst layer (CL) lying between the two flow channels (the gas channel on the right, where the CO_2 is fed and gaseous products are collected and the liquid electrolyte channel on the left, where the catholyte is fed and the liquid products, if any, are leaving the cell). The idea behind the utilization of such articulated structure comes from the necessity of delivering the CO_2 as close as possible to the electrolyte coated catalyst particles in a gaseous form, to minimize the thickness of the diffusion layer. Doing so, the mass-transfer boundary layer has been effectively reduced to 50 nm (from planar electrodes, around three to four order of magnitude lower) [41]. To achieve this, the diffusive path of CO_2 has been constructed with two hydrophobic substrates, the macroporous and microporous layer (their overall thickness ranging from 100 to 500 μm [38]). The macroporous layer serves the functions of mechanically sustaining the cell and conveying the electrons from the current collector (whose aim is to distribute the electric current uniformly [35]) to the microporous layer while providing a path for CO_2 to diffuse. As thoroughly explained in chapter 1.2.5 it is typically constituted of carbon fibers structures (paper or cloth). The microporous layer instead, is the support upon which the catalyst layer is deposited.

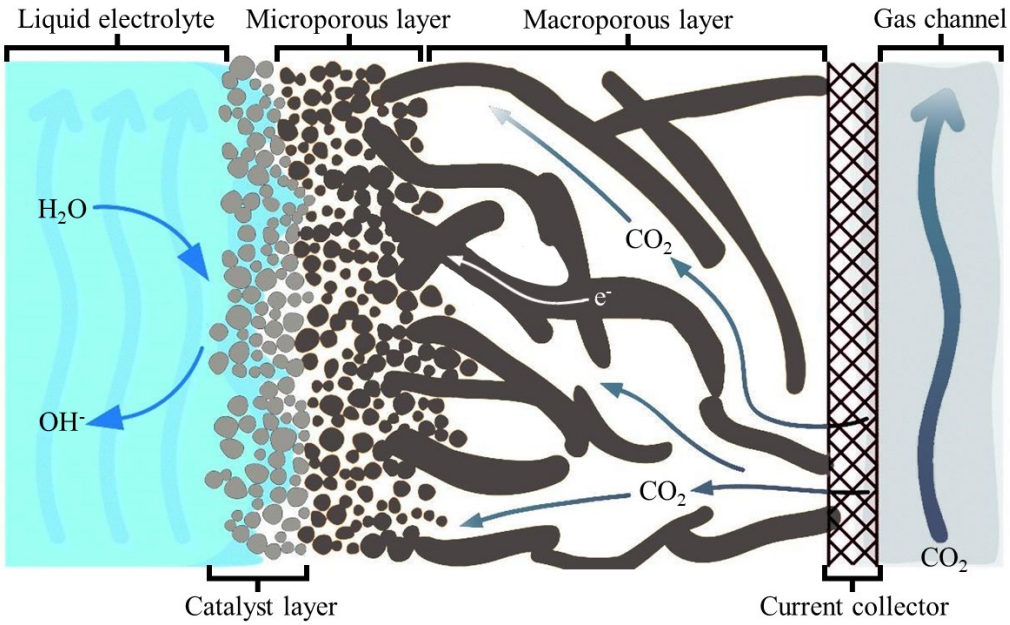

Figure 1.9 Gas diffusion electrode and its main component. Adapted from *[38]*.

Being constituted of carbon black nanoparticles and an hydrophobic polymer, the microporous layer is endowed with an inherently smaller granulometry with respect to the macroporous layer, which is responsible for enhanced electrical connection with the catalyst particle (due to a higher surface area) and flooding prevention [42].

Finally the catalyst layer is composed of a mixture of catalyst nanoparticles and an ionic binder (e.g. Nafion®), which binds the particles to the support while not insulating them [43].

1.2.4. Working principles of gas diffusion electrodes

Having a clear notion about the GDL structure, the phenomena occurring in such a complex system can be described (at least macroscopically) by assuming the cell to be gradually activated in a sequence of steps as follows. At the beginning no voltage is applied to the electrodes, say no electric current is flowing. The whole cell is filled with air at atmospheric pressure. The valves controlling the flow of the gaseous CO_2 (assumed to be pure) and liquid electrolyte are opened to ensure having the desired flowrates and both the flow channels gets filled with the fluid flowing. Due to a gradient in CO_2 concentration between the whole gas diffusion layer (currently filled with air at approximately the same pressure of CO_2) and the flow channel, the carbon dioxide diffuses inside the macroporous, microporous and catalyst layer, filling their pores. Air

counter-diffuses inside the flow channel where it finally gets expelled. If for a moment we imagine an impermeable wall to exist between the liquid channel and the CL, then at steady state the whole GDE, except the liquid electrolyte channel would be filled with CO_2 at atmospheric pressure and no concentration gradient would have existed since CO_2 sinks are not present. But this is not the case as the CO_2 and the liquid electrolyte come in contact inside the CL. Two phenomena are now occurring. The first one: according to the capillary pressure (i.e. the difference between the liquid and the gas pressure), the CL pore size distribution (PSD) and the wettability of the pores, liquid and gas can organize themselves inside the CL according to three different scenario [38] reported in Figure 1.10.

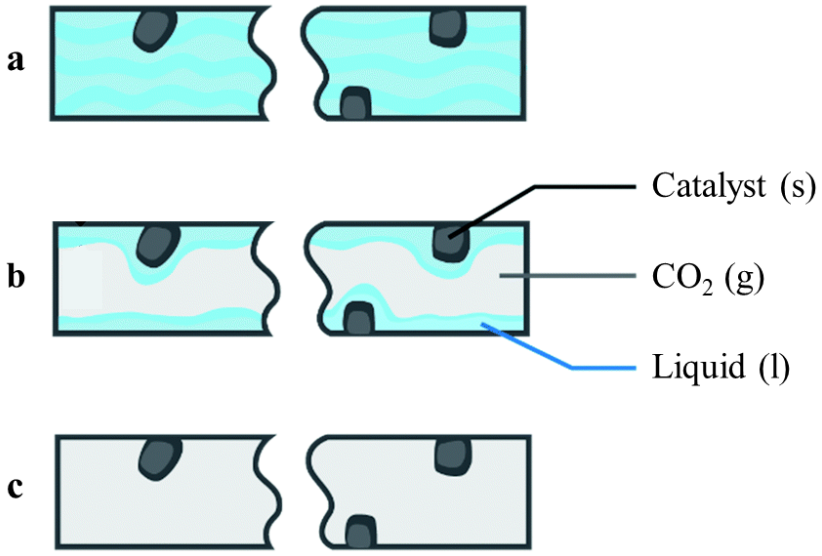

Figure 1.10 A pore of the catalyst layer in 3 conditions. **a**, Fully flooded pore **b**, Partially wetted pore (where triple-phase boundaries are realized) **c**, Fully dried pore. Adapted from *[38]*.

The second phenomena concerns the dissolution of carbon dioxide in water. The amount of carbon dioxide present in water in its dissolved form $CO_2(aq)$, can be described by Henry's law, which predicts a maximum concentration of 34 mM when 1 atmosphere of pure CO_2 at 298 K is considered [44]. The implication of this phenomenon is that, regardless of the capillary pressure, inside (or outside) the CL a liquid/gas interphase exists and CO_2 gets dissolved. This means that a concentration gradient for the CO_2 exists, as in correspondence of the gas/liquid interphase there will be a net flux of CO_2 from the gas to the liquid phase. Of course, according to the resistance provided to flow by the gas diffusion layer (determined by the effective diffusivity for molecular diffusion and

effective permeability for pressure-driven flow) the gradient will be more or less steeper (the higher the resistance the steeper the gradient).

As soon as the CO_2 dissolves into the aqueous electrolyte and provides by the hydrolysis reaction carbonic acid (Equation 1.7), it also reacts with ionic species according to the carbonate equilibrium (which will be further investigated in chapter).

$$CO_2(aq) + H_2O \rightleftharpoons H_2CO_3 \qquad 1.7$$

The described system is by no means trivial, and the electrolysis is not even occurring as the power supply has not yet been switched on. So let us connect the clamps to the cathode and the anode, and establish between them a potential difference.

Under the effect of an electric field, electrons are moved from the anode, where the oxidation occurs, to the cathode where the reduction occurs. Inside the cathode, as visible in Figure 1.9 the electrons move from a zone of high electrical potential (the current collector, where the clamp is attached) to a zone of lower potential (in the CL where electrons are used for charge transfer reactions). The electrons flow is none other than the electric current and the higher the effective conductivity of the porous media, the higher the current flowing when a potential is applied. When the electrolysis reactions start the dissolved CO_2 is reduced to higher energy products with a rate determined by the potential applied and the local reagent concentration (the current then is adjusted based on how much reactant is available to be reduced at the catalyst surface). This consumption further depletes carbon dioxide on the nanoparticles surface and the gradient in its concentration further increases, increasing the diffusive flux. As will also be clarified later, the change in the local pH near the electrodes due to the CO_2 consumption is additionally responsible for an increase in the homogenous consumption of CO_2 by bulk reactions which instead promote pressure-driven convective flows. Again the gradient in CO_2 concentration in the horizontal direction of Figure 1.9 is determined by the effective diffusivity and permeability of the porous media.

If we imagine to increase the potential for increasing the consumption rate, there will be a point in which the diffusion of aqueous CO_2 towards the catalyst particles occurs so slowly that its surface concentration vanishes. In this case the cell is said to be diffusion-limited as no matter how much the voltage is increased, the reduction rate will always be restrained by lacking CO_2 to be reduced.

We clearly understand now the importance of tailoring the gas diffusion media in order to have reasonably good effective transport properties which allow to push the reaction rate to industrially compatible scales.

For this reason, in the following chapter a close-up on the structure of the diffusion medium will be provided.

1.2.5. Manufacturing of gas diffusion layers

Gas diffusion media utilized in CO2 electroreduction build upon previous research endeavors focused on enhancing the GDL performance in fuel cells, given the shared functionalities between the two applications.

Two main gas diffusion layers can be employed, both carbon-fiber-based, due to their high porosity and electrical conductivity [45]:

- Non-woven carbon papers;
- Woven fabrics (or clothes).

In Figure 1.11, scanning electron microscope (SEM) micrographs are also shown.

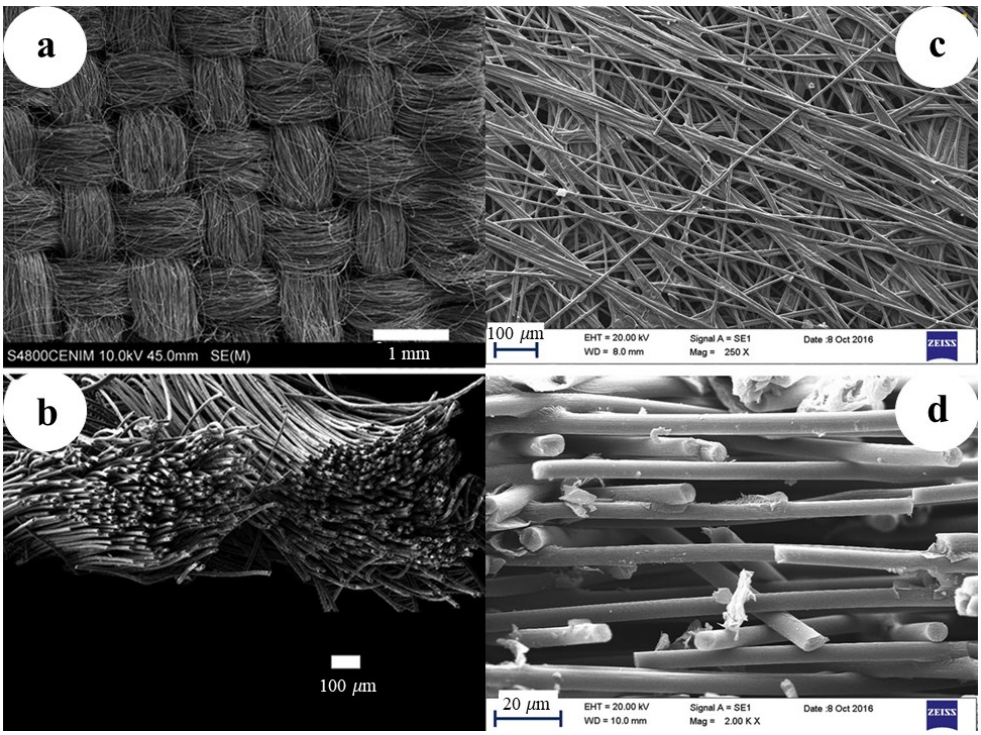

Figure 1.11 Macroporous gas diffusion layer, SEM micrographs. **a**, Through-plane view of a woven fabric **b**, In-plane view of a woven fabric **c**, Through-plane view of a non-woven paper **d**, In-plane view of a non-woven paper. Adapted from *[125]* (a and b) and *[68]* (b and c).

Regardless of the type, the precursor used in the manufacturing process of these fibers is a copolymer filament made of more than the 90% by polyacrylonitrile (PAN). The choice is directed toward this material due to its low cost (the market size being determined by their utilization in the textile market), high carbon yield (mass of remaining carbon after the production process relative the initial precursor mass) and carbon-fiber properties (high stiffness, high strength and light weight) [45]. Then, the production processes of the two different substrates shown in Figure 1.11 differentiate as while for the woven production the filament of the precursor is twisted to form a spun yarn, weaved and finally carbonized at 1600-1700 °C in vacuum, for the carbon-fiber paper the filament is chopped in many smaller fibers (3-12 mm) which are then grouped in continuous rolls through a wet papermaking process. The rolls then are impregnated with a phenolic resin (which will be referred to as "binder"), cut in sheets of 1 m^2 and stacked one over the other with a compression molding to reach a thickness ranging from 0.15 to 0.30 mm. Finally the stacks are graphitized at 2000 °C in vacuum [45].

For how the process has been described it is clear that carbon-fiber papers, which will constitute, as soon clarified, the core of the current study, are originally constituted of two different materials: the graphitized PAN fibers and the carbonized binder. Additionally, to increase its hydrophobicity (important when flooding represents an issue at the utilized operating conditions), the so-obtained macroporous layer can be coated with polytetrafluoroethylene (PTFE), also commonly referred to as Teflon®.

On top of the so-produced macroporous layer, carbon particles mixed with PTFE are added (e.g. by spraying) to form the microporous layer, responsible for further inhibiting water infiltration due to smaller pore sizes, as visible in Table 3.

Table 3 Basic morphological characteristics of the porous media constituting the gas diffusion electrode.

	Macroporous layer	**Microporous layer**
Thickness [μm]	190-250 [46]	<50 [45]
Porosity [-]	0.7-0.9 [47]	0.3-0.7 [47]
Pore size [μm]	10-30 [45]	0.01-0.1 [47]

So far the main features of gas diffusion electrodes have been discussed, clarifying the reasons why they have been extensively employed for improving the performance of electrochemical converters, shedding light on their working principle and briefly going through the manufacturing of one of their main constituent. In particular, the relevance that the engineering of the gas diffusion layer has on the overall cell performance has been qualitatively described.

The upcoming subsection will focus on the investigation of gas diffusion layers, with an emphasis on the essential tool used for this purpose, namely multiscale modeling.

1.3. Multiscale modeling of gas diffusion layers

Ever since gas diffusion electrodes have been developed, an increasing interest in fully understanding the rich variety of chemical and physical phenomena occurring inside the cell has also been experienced. Indeed numerical modeling of chemical reactors can help in this task as it represent a tool that enables the prediction of the reactor performances when different operating conditions are tested, without passing through expensive and time-consuming experiments [48]. Even before that, models are useful to check if all the physics of the phenomena occurring has been correctly captured (when they are validated with experimental data). Only at that point, the engineering of the chemical reactor can be rationalized and justified by the evidence provided by the model itself. And particularly for gas diffusion electrodes, there is a significant scientific potential to advance our fundamental understanding of the multiscale processes taking place within three-dimensional GDEs and to enhance GDEs performance through systematic engineering strategies. [36].

1.3.1. Introduction to multiscale modeling

In the realm of chemical reactor modeling, multiscale modeling has naturally emerged from the development of chemical reaction engineering [49]. In order to comprehend its functioning, it is essential to have an understanding of the processes that it attempts to model, say chemical reactions at industrially relevant conditions. In these conditions in fact, despite chemical reactions occur on a molecular level, they are influenced by the macroscopic behavior of the reactor, such as mass transfer, heat transfer and fluid dynamics (that determine local composition, temperature and pressure). This feature is conceptualized by recognizing that inside chemical plants, coupled events with

time scales spanning from the femtoseconds (related to molecular dynamics of the chemical reactions occurring) to the years (for achieving a production target) occur. Similarly, when considering spatial scales, the situation is analogous in terms of the extent or range being examined, going from tenths of angstrom (e.g. 0.74 Å for the hydrogen bond length [50]) to meters (10^0-10^1 m for industrial reactors). The purpose of Figure 1.12 is illustrating the complication behind industrial chemical processes by visually depicting the typical time and space scales involved within them. In this context, the basic idea behind multiscale modeling is computing relevant information at each of these scales and then coupling them in a physically sound model [51].

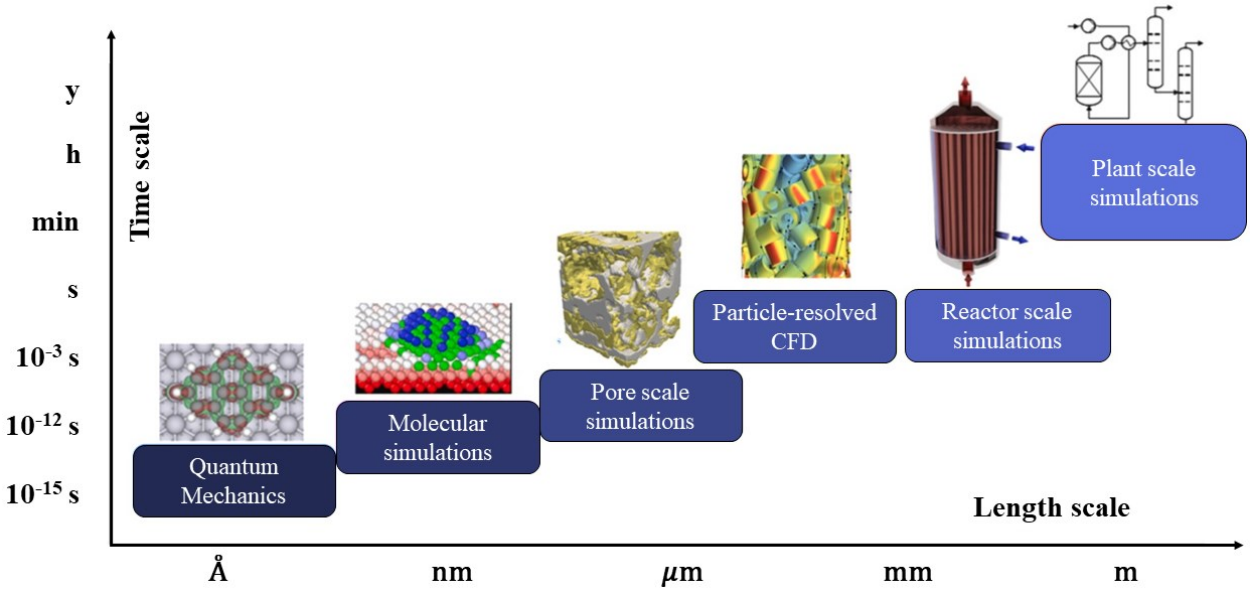

Figure 1.12 Typical space and time scales involved in processes of industrial chemistry. Adapted from *[51]*.

While multiscale modeling has numerous applications in reaction engineering, this work specifically focuses on its implementation in catalytic processes. Modeling a catalytic process through all its different length and time scales in fact, has the potential for driving from a fundamental perspective, the design of novel catalytic reactors [52]. Scientific literature about catalytic processes tells a story of rising interest in applying this approach. For example, the adoption of particle-resolved computational fluid dynamics (PRCFD) allows much more detailed study of fixed bed reactors with respect to the conventional porous medium model [53]. In this context, the implementation of an operator-splitting technique allowed for the multiscale simulation of heterogeneous catalytic systems by coupling detailed microkinetic models with PRCFD [54]. As a result

it was possible to bridge the microscale with the macroscale by using a fully first-principles based approach. Moreover, with reference to process intensification, multiscale modeling (together with machine learning techniques for reducing its computational burden and advanced manufacturing for physically reproducing the underlying new technologies) will play a pivotal role when trying to optimize the reactor performance at each scale, ensuring efficient cross-scale interactions [55].

While successful application of this technique is attainable, it should be noted that it requires effort and presents challenges that need to be addressed. Within an insightful feature article, Maestri describes the challenges behind the application of multiscale modeling through the dimensions of complication and complexity [56]. Particularly, the complication lies in accurately describing of the phenomena at the different scales and in smoothly coupling them in a simulation, from the atomistic level to the reaction environment. The complexity instead comes from the high dimensionality (degrees of freedom) of the phenomena, especially at the microscale (a reported example is the microkinetic model of the CH_4 partial oxidation on Rhodium, where 13 different adsorbed species take part in 41 reversible elementary steps).

In practice, when addressing the smaller scales, the remaining challenges are usually related to understanding the intrinsic functionality of the catalyst, especially during the proceeding of reactions, accounting for the nature and the structural dynamics of the active sites (the so called structure-dependent microkinetic modeling [56]).

When attempting to model larger scales, it becomes necessary to account for phenomena that occur at smaller scales as well. However, the methodology described above, which involves solving Navier-Stokes equations in complex geometries and incorporating detailed micro-kinetic mechanisms to accurately represent surface reactivity, poses significant computational challenges. As a result, the applicability of this methodology is limited [57]. The utilization of the hierarchical approach, hereafter described, may offer a solution to this challenge.

1.3.2. Hierarchical approach in multiscale modeling

When elucidating the concept of the hierarchical approach in multiscale modeling, it is crucial to recognize that distinct models exist for describing specific space/time scales, each with its own level of precision. For example, with reference to Figure 1.12, the reactor scale simulations can be performed by using ideal reactor models, macroscopic models making use of transport correlations or CFD simulations. Similarly, following the fashion

of increasing accuracy and computational cost, the quantum scale can be treated with semi-empirical methods, Density functional theory (DFT) based correlations and ab initio methods [58]. Due to the positive correlation between accuracy and computational cost of models, when bridging the different scales, "the inclusion of highest level theory at each scale is computationally intractable" [58]. This is where the hierarchical approach comes into play (Figure 1.13), as it helps retaining precious information from detailed descriptions of physical/chemical phenomena at each scale.

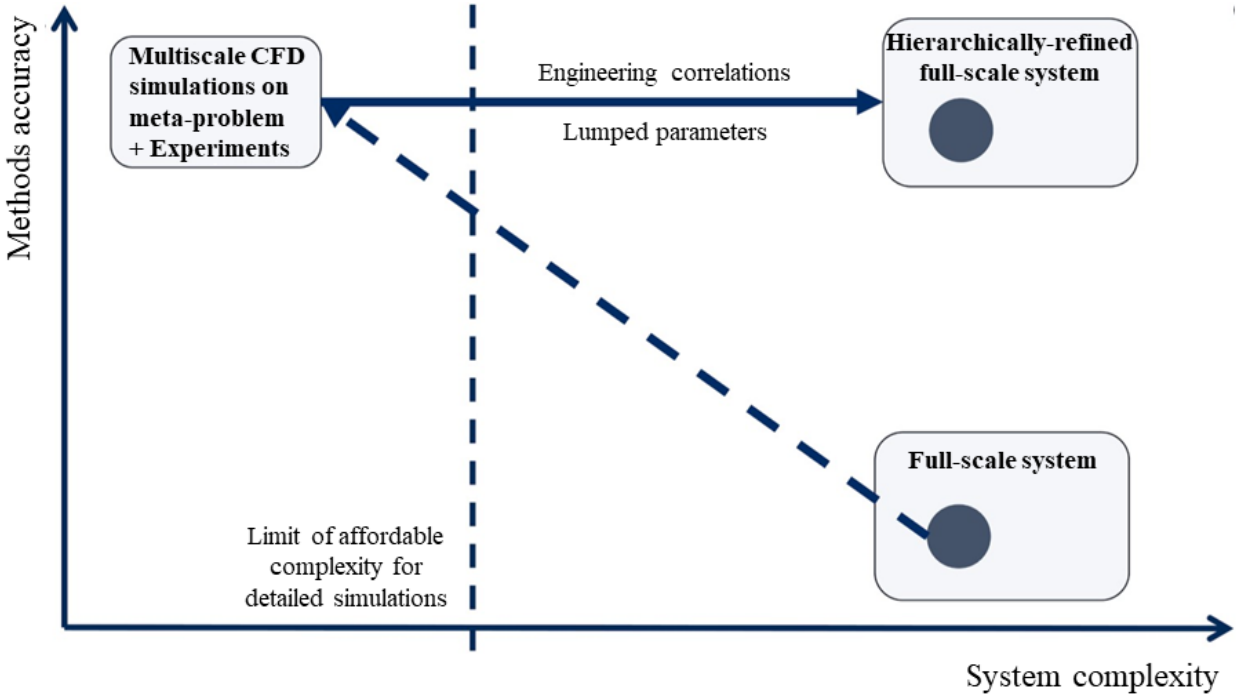

Figure 1.13 Hierarchical approach in multiscale modeling explained. Adapted from *[56]*.

The hierarchical approach procedure depicted in the figure, can be described in the following steps [56]:

1. The first step is to model the full problem (i.e. the whole chemical reactor or chemical plant) with the lower accuracy methods. The model is used to compare its prediction with selected experimental results;
2. The disparities in the results from the two sources (experimental and in silica) are examined, and the origins of these discrepancies are identified within specific components of the model;

3. A problem of reduced dimensions called sub-model or meta-model is created to study the critical aspects evidence in point 2. The sub-model allows to investigate the given aspects of the full-scale system as its reduced complexity allows for detailed investigation by the means of first-principles methods;
4. The information obtained through the sub-model is reinserted in the full problem to increase its accuracy;
5. Steps 1 to 4 are repeated for all the suspected faulty aspects of the full problem to hierarchically refine it.

For the purposes of the current work it is relevant how to hierarchically refine reacting systems at the reactor scales. An example is provided in the work by Rebughini et al. where gas-to-particle heat and mass transfer coefficients in micro packed bed reactors have been derived [59]. In the work at first CFD simulations have been performed on an reduced sample of the whole reactor. A series of in-silica experiments have been conducted to analyze the system behavior at different Reynolds number. The results of the simulations have been then interpreted by the means of a macroscopic model to derive a CFD-based correlation for transport properties. The so-obtained correlations has shown to fully retain the features of the detailed CFD simulation.

In another case-study a similar procedure has been used for deriving gas/solid mass transfer coefficients in open-cell foams [60]. After virtually reconstructing the required geometry, CFD simulations have been performed to facilitate the parametric analysis of foam geometrical properties. A suitable characteristic length and a correlation for the Sherwood number based on the Reynolds number and the porosity of the sample have been derived by interpreting the results of the simulations through a 1D heterogeneous macroscopic model, under the assumptions of full external mass transfer control.

The applications mentioned earlier specifically dealt with thermal systems, but the approach discussed can be equally utilized for electrochemical systems, as discussed in the next chapter.

1.3.3. CO_2 electroreduction as a multiscale phenomenon: state of the art and opportunities

In chapter 1.2.4 the working principle of a GDE has been described from a reactor scale perspective. In fact, it should be noted that also in this system the observed

performance of the reactor is the result of the interplay between elementary steps taking place at the atomistic scale and the flow conditions established at the macroscale. Despite the fact that the focus of the current work is not to obtain a detailed description of the surface reactivity it should be recognized that CO_2 electroreduction, whether occurring in a GDE or in a standard H-cell is a multiscale process. At the molecular scale, it involves the interactions between CO2 molecules and the catalyst surface, which occur on the nanometer scale and in short time frames. At the mesoscale, it encompasses the transport of reactants and products within the porous electrode structure, which occurs on the micrometer scale and over longer time periods. Lastly, at the macroscale, it involves the overall performance of the electrochemical system, such as the current density and selectivity, which are observed at the reactor scale level.

In this sense, effort has been focused in tailoring the properties of gas diffusion media (both morphological and transport related) which are known to significantly affect the electrode performance. Currently, three different methodologies exist for estimating these properties (Figure 1.14). The first one, which falls outside of multiscale modeling techniques is the experimental one. Morphological information like porosity and pore size distribution and effective transport properties of real samples are analyzed by consolidated approaches for porous media (e.g. mercury intrusion porosimetry or X-ray computed tomography and diffusimetry, respectively [61]). The second methodology consists in numerical simulation performed on computational reconstructions of GDL samples. In this case the virtual geometry can either be obtained by experimental methods (e.g. Micro-computed tomography (μCT) [62]) or by stochastic reconstruction of the sample [63].

Each of these three approaches naturally has its own advantages and disadvantages. As an example, while it is true that tomographic scans of real samples can deliver accurate 3D models, the systematic analyses of a wide range of samples are costly in terms of time and resources. Even more importantly, the resolution of physical rendering significantly restricts imaging-based methods, and the capability to discern distinct phases (such as carbon and PTFE) within the GDL continues to pose a substantial challenge [64]. Stochastic reconstructions roughly overcome all of these mentioned challenges but validating the structure and having a correct representation of the real GDL is a challenging task [65]. At last for experimental methods selecting appropriate measurement techniques that can provide accurate and reliable results for the effective transport properties of GDLs is a challenge. Different techniques may have limitations or may require complex experimental setups. Moreover the set of investigated samples is limited by their commercial availability.

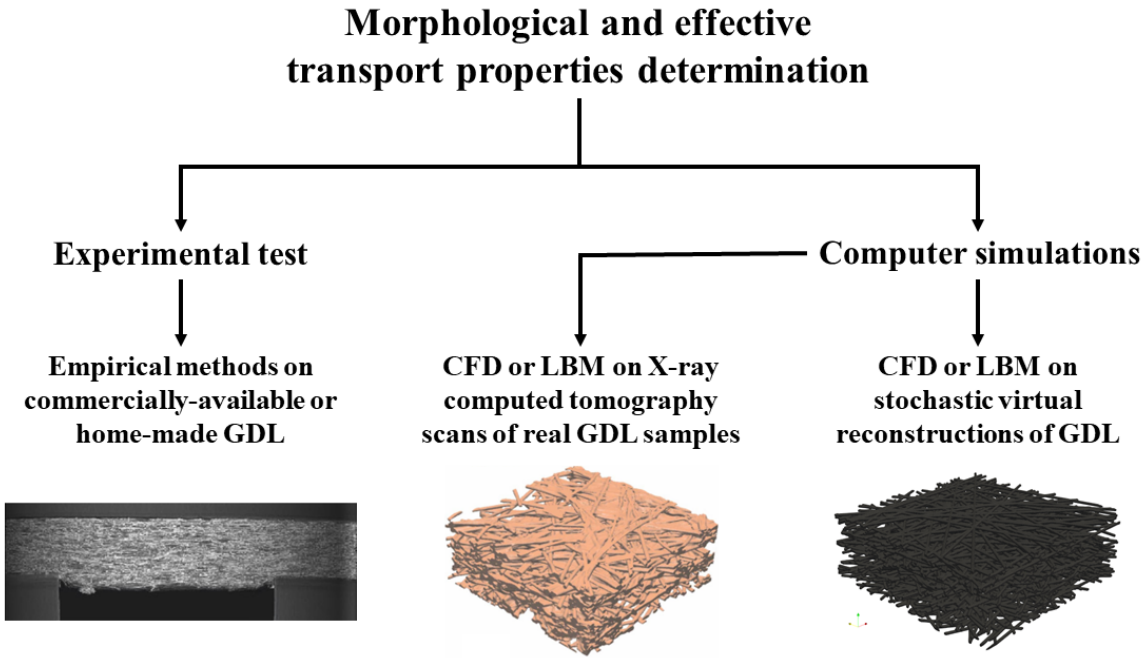

Figure 1.14 A schematic view of the different approaches utilized so far, for determining the morphological and effective transport properties of gas diffusion layers. From the left to the right *[127]*, *[62]*,this work.

So the opportunities for multiscale modeling of CO_2 electroreduction gas diffusion layer have to be searched in stochastic reconstructions as they offer an appealing alternative to serve as a potent tool for establishing a relationship between freely adjustable microstructural parameters and the macroscopic behavior of the geometry (that is bridging the microscale with the macroscale). As previously mentioned there are no chemical reactions taking place within the diffusion media. Therefore, when employing multiscale modeling for this component of the cell, it is sufficient to descend to the microscale level (Figure 1.15).

This fundamental approach to the study of gas diffusion layers has been employed since 2007 with Schulz et al. [66] that pioneered the development of a stochastic model incorporating actual microstructural parameters obtained from scanning electron microscopy image and literature data. The virtual geometry was then used to assess and validate the resulting permeability of the GDL. Over the course of time the models representativeness of the GDL improved. As an example, the model by Schulz et al. originally accounted only for the carbon fibers without considering the presence of the binder material holding the fibers together. Binder was originally added to the geometry with a Bernoulli filling approach (in which the pores are randomly filled with binder with a fixed probability p) [67] and it was only with the seminal work by Becker et al [62] that

image processing techniques have started to be considered for the binder addition process due to their capability of accurately mimicking the wetting nature of the phenolic resin. Recent works have also accounted for the presence of PTFE, notably the stochastic model by Daino et al. [63], which makes use of 3D morphological image processing operations, obtaining a close replica of commercial GDLs as confirmed by visual validation with 2D micrographs and 3D X-ray synchrotron data. Fine tunings of the stochastic reconstruction were provided by Simafrooktheth et al. [68], in which the measured fiber orientation distribution from a GDL SEM scan is implemented in their virtual reconstruction, and by Hinebaugh et al [69], whose work stands out from the others for implementing three novel features concurrently, namely the periodicity of the fibers in the x-y plane, the vertical orientation of the fibers (named "pitch") and the placement of fibers in the x direction based on μCT obtained local porosity distribution. The information retrievable through these microscale reconstructions is accessed utilizing PRCFD or LBM to obtain correlations for effective transport properties which then are back utilized in macroscopic model of the full-scale gas diffusion electrode.

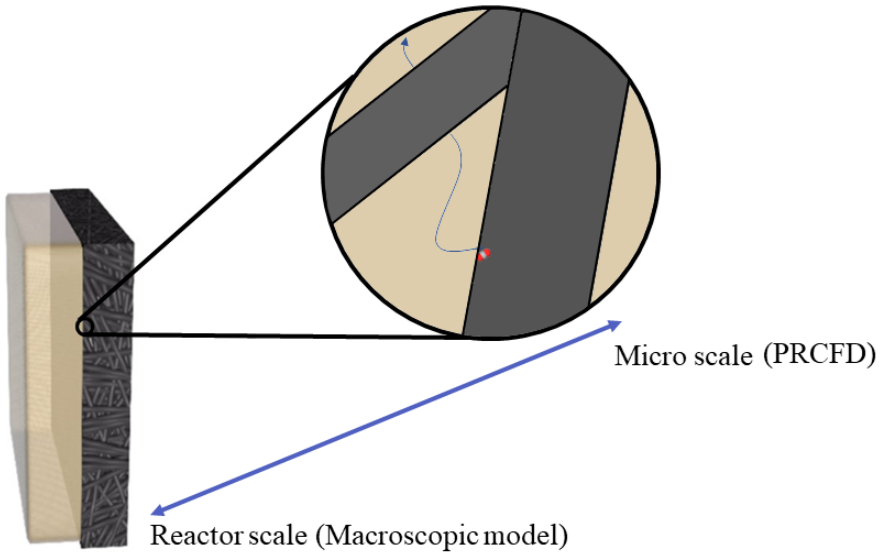

Figure 1.15 Bridging reactor scale and micro scale in gas diffusion layers. CO2 molecule not in scale. Adapted from *[36]*.

Numerical modeling of GDE has been carried out significantly for fuel cell applications, for which the first models are dated back to the sixties of the last century [70]. For what concerns CO_2 electrolysis instead, to the best of the author's knowledge, the first macroscopic model ever built is the one developed by Delacourt & Newman [71].

In the model, a cell comprising of both cathodic and anodic chambers, is simulated by discretizing in space the governing equations with finite differences in 1 dimension. The catalyst layer is represented as a surface rather than a domain of finite thickness and the liquid phase homogeneous reactions are assumed to be at the equilibrium. The model was improved by Bell et al ., where the latter two assumptions where removed, and only the cathodic chamber was simulated [38] (one year later, the same group developed a similar numerical model, this time considering an Anionic exchange membrane rather than a liquid electrolyte between the cathodic and anodic chambers [72]). Also other interesting models have been developed notably the one from Löffelholz et al [73] which describe through geometrical considerations the flooded portion of the catalyst layer ("thin-film flooded agglomerate model") and the one from Smith et al, which introduces the second dimension (in the direction of the flow channel) to account for longitudinal concentration gradients naturally occurring also in real case scenarios [74].

Among the different assumptions made in each of these studies, a common one is that of utilizing the effective medium approximation (EMA), in which the transport phenomena in the different phases are described by the means of constitutive laws with properly defined effective transport properties (more insights on this approximation will be provided in the theoretical section). Effective transport properties (such as effective electrical conductivity for the solid phase and effective diffusivity for the gas phase) are a function of the morphology of the porous media and of course of the bulk value of the property itself. As a consequence, these properties have to be derived in some way for the porous structure of interest, in our case for the gas diffusion layer.

1.4. Motivations behind the study

Before trying to explain the motivations behind the study of a particular scientific problem, it is often convenient to start from the uncertainties and the doubts the underlying topic raises.

1.4.1. Remaining challenges of CO_2 electroreduction and GDE

To gain insight into the obstacles that currently hinder the industrial significance of CO2 electrolyzers, one can seek to understand the specific requirements and expectations that the industry has for this type of technology. In Figure 1.16 a cause-effect

mapping on industrial requirements and related challenges is reported, with a stepwise increase in the degree of complexity. Small wonder, it all starts from the need of a cost-effective solution.

To the knowledge of the author, most of the literature reviews on the topic agrees on identifying the reported challenges as the main drivers for the current research effort. High reaction rate, high selectivity, low energy requirement and high durability and affordability of the cell can, in fact, be obtained by putting in place the actions listed in the rightmost column. To make some examples, it is clear how for improving selectivity towards desired products, required for minimizing downstream expensive separations, selective electrocatalyst are needed. Also the transport rate of carbon dioxide towards the electrode surface has been proved to have an effect on selectivity [75]. In particular when the CO_2 consumption rate is pushed by increasing the potential applied, the concentration of the dissolved gas near the electrodes may decrease if its transport rate is not able to sustain such increased depletion. As a consequence, the hydrogen evolution reaction (Equation 1.8 in alkaline media), may increase in its rate due to less CO_2 subtracting the catalyst active sites reducing the faradaic efficiency towards the desired product.

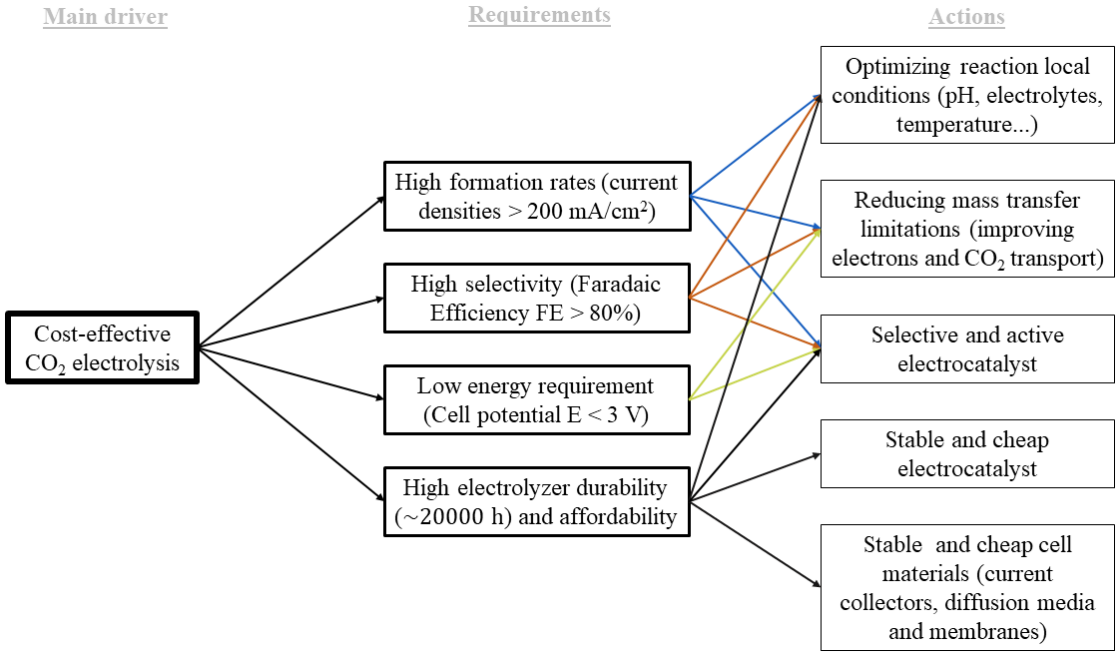

Figure 1.16 CO2 electrolysis challenges map. Data on industrially relevant current density, faradaic efficiency, cell potential taken from *[75]*, operational lifetime from *[76]*.

$$2H_2O + 2e^- \rightleftharpoons H_2 + OH^- \qquad 1.8$$

At the same time cost-effectiveness of catalytic materials is required for improving the affordability of the electrolyzer. Moreover, the catalyst activity indirectly affects the cost of the electrolyzer as, regardless of the materials employed, the higher the current density, the lower the geometric surface of the electrode required, the lower the capital investment involved due to smaller cells [76]. This is a crucial aspect when considering that electrolyzers are not endowed with economy of scale due to their modular character [25].

Lastly, the energy efficiency, reflected in the potential applied to the cell, is hampered by reaction kinetics inefficiencies (the so called activation overpotential) determined by the catalyst being used, and by the transport limitations (the so called concentration overpotentials and ohmic losses).

The current CO2 electroreduction challenges thus, can be classified in two main investigation frontiers [76]. The first one is about catalytic investigation, say discovering and analyzing the performances of novel catalysts that promote the CO_2 reduction reaction (CO_2RR) to the desired product, and the second one concerns the design of the flow cell in all the other aspects (electrode configuration, electrolyte choice, materials choice, flow channel and gas diffusion layer engineering and so on). Among these two, the current study focuses on the design of the flow cell, with a particular attention directed towards the gas diffusion layer and how its structure affects, through transport limitations, the performance of GDEs.

1.4.2. Motivation statement and outline of the work

The majority of the computational works developed for understanding the effects of the morphology on the effective transport properties of gas diffusion layers only take into account the porosity as a determining factor (in the so called ε/τ models approach). However, before reaching the conclusion that the transport properties of the mentioned substrates can be solely described as a function of porosity, a more comprehensive analysis is necessary. In this analysis, other parameters should be allowed to vary independently, and the impact of their changes should be evaluated. Moreover, all of the analyzed literature works lack a fundamental understanding on how the porous structure of GDLs is linked to their resulting effective transport properties.

As an additional fact, even if plenty of studies have been conducted separately for macroscopic modeling of GDE and effective transport properties determination of the GDL, none of them in the former category have used real estimates of the effective transport properties, specifically computed for gas diffusion layer. In all the cited works in fact, a more general correlation for effective porous media is used. Highly popular in this sense, is the Bruggeman correlation, developed for isotropic porous media of randomly positioned spheres or cylinders [77]. Insights for the derivation of the Bruggeman correlation are provided by Tjaden et al., who also raise concerns on the widespread application of this formulation [78]. Doubts on its applicability are arising especially when observing that the correlation predicts the same effective transport property regardless of the morphology of the geometry considered, and of the direction of the material/energy flow (anisotropy not accounted for).

The purpose of the following work is to perform a fundamental investigation of the effect of geometrical properties on the effective transport properties of gas diffusion layers employed in CO_2 electroreduction cells. The effective diffusivity and the effective conductivity of virtual reconstruction of gas diffusion layers, governing respectively the transport of chemical species in the gaseous phase and the transport of heat/electrons in the solid phase are analyzed. Particularly, it is assessed if parameters other than the porosity of the samples affect these properties and consequently, suitable correlations for the effective transport property ratios are derived. More in details, a virtual geometry of a carbon paper based gas diffusion layer is recreated using a stochastic reconstruction method based on microstructural parameters. Valuable insights on the morphology of the reconstructed samples are given, in terms of local porosity distribution and pore size distribution. After the virtual geometry has been validated by the means of morphological and physically-based metrics, a CFD simulation campaign is executed in order to assess the dependency of selected structural parameters (porosity, fiber diameter and binder volume fraction). The results of the simulations are then be interpreted and used in deriving correlations for the effective thermal/electrical conductivity and effective diffusivity. The rationale behind the work can then be summarized as depicted in Figure 1.17, where the work has been conveniently subdivided in the three major milestones: geometry generation, geometry validation and derivation of the correlations.

Additionally, in the full spirit of multiscale modeling, the correlations are also tested in an in-house built macroscopic model for a GDE for conducting an analysis based on the discrepancy among the simulation-derived effective transport properties and the ones coming from the Bruggeman model.

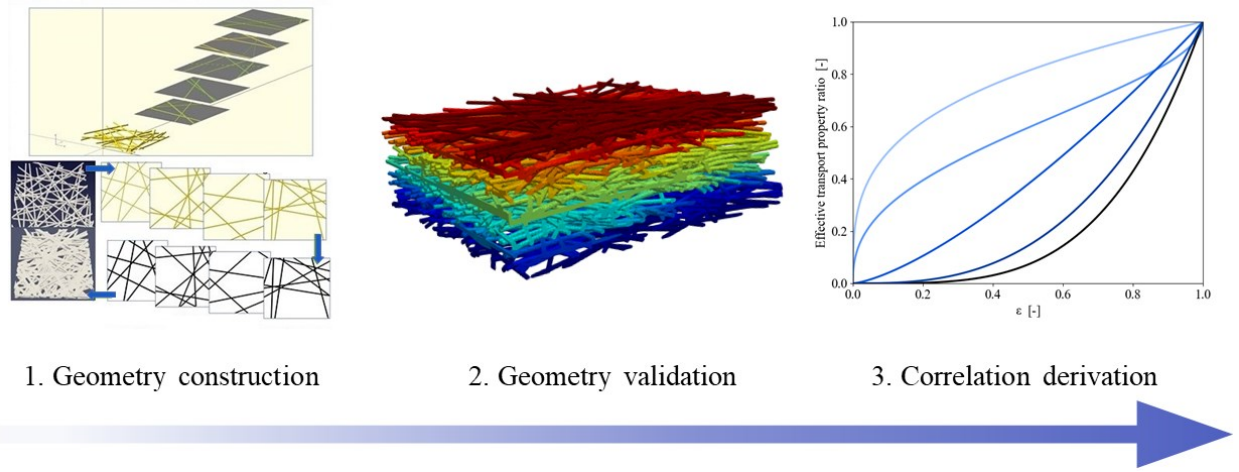

Figure 1.17 Milestones of the current work. After the geometry construction and validation, the correlation for the effective transport properties are derived.

2 Theoretical background of CO_2RR

As qualitatively described in chapter 1.2.4, a multitude of phenomena simultaneously occur inside an electrochemical device. In general, even though this work mainly focuses on the transport aspects of the cell, it is possible to recognize in the behavior described the three pillars of chemical engineering Figure 2.1. As such, before proceeding with the chapters of methods and results, where such phenomena will be interpreted by the means of designed simulations, it is fundamental to understand the chemical and physical phenomena governing vapor-fed CO_2 electrolyzers.

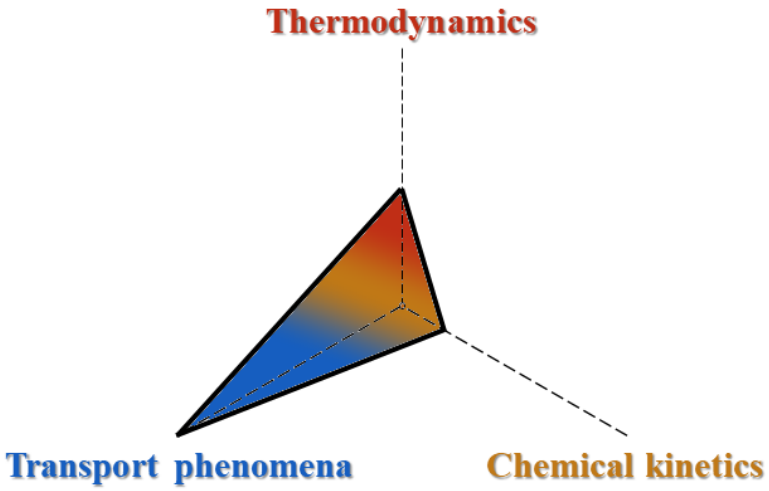

Figure 2.1 The three pillars of chemical engineering. In this work the main focus is on transport phenomena, even though some aspects of chemical kinetics and thermodynamics are essential for the development of the macroscopic model.

2.1. Thermodynamics

When setting the framework for the thermodynamics behind electrochemical cells, it is often useful to recall some concepts from the study of an electrical circuit as after all, that is what an electrochemical cell is.

The electrochemical reactions occurring in a cell, belong to the class of redox reactions, where it is possible to identify a species losing one or more electrons (the reducing species, which oxidizes itself) and a species gaining these electrons (the oxidizing species, which reduces itself). To be precise, an important distinction between an electrochemical reaction and a chemical redox reaction is that, in an electrochemical reaction, reduction occurs at one electrode and oxidation occurs at the other, while in a chemical reaction, both reduction and oxidation occur in one place [33]. Therefore it is common to split the complete reaction in two half-reactions, conventionally written in the verse of reduction (Equation 2.1). The two species, Ox and Red constitute a redox couple.

$$Ox + ne^- \rightleftharpoons Red \qquad 2.1$$

This is the elementary notions behind the Voltaic pile, the first pile (or electric battery) ever built [79]. This pile is made by copper and zinc electrodes, immersed inside a sulfuric acid solution and connected via metallic cable (Figure 2.2).

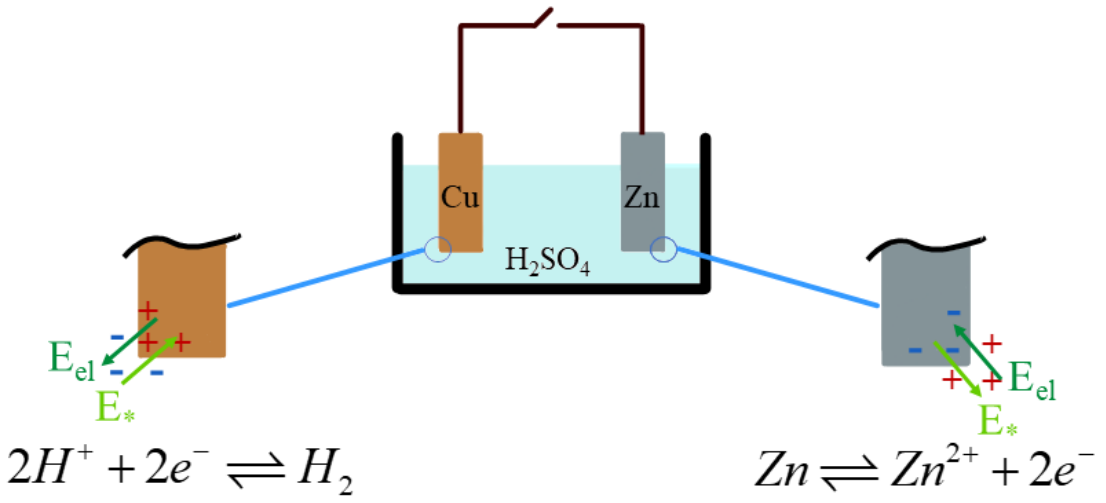

Figure 2.2 Voltaic pile. As long as the circuit is open, the reactions cannot proceed and the current does not flow.

As soon as the metal plates are immersed in the solution, the zinc electrode becomes negatively charged, as some metal atoms lose their electrons to move inside the solutions as positive ions. The process is promoted by the tendency of the zinc metal to be dissolved. This tendency can be related to an electric field, named electromotive field E_*. Nevertheless, when the circuit is open (no electrical contact between the electrodes) the process is rapidly blocked by the insurgence of an electrostatic field E_{el}. A similar process occurs on the copper side, where the electrons are withdrawn from the electrode by the adsorbed hydrogen ions, to give molecular hydrogen. The metal is left with a positive charge but before the process can continue, an electrostatic field acts to balance the tendency of hydrogen to be reduced (expressed by another electromotive field). In these conditions, globally the current does not flow, only the copper electrode is positive with respect to the zinc one [80].

When the circuit is closed over a load (Figure 2.3), the electrons in excess on the zinc plate are now free to move towards the copper one, so that under the driving force provided by the tendency to reach the chemical equilibrium, the half-cell reactions can occur continuously and the current flows from the copper to the zinc (as by convention the current is associated to positive charge being moved. In reality we know that the real charge carriers in metals are electrons and this has been proved experimentally by Edwin Hall in 1879 [81]).

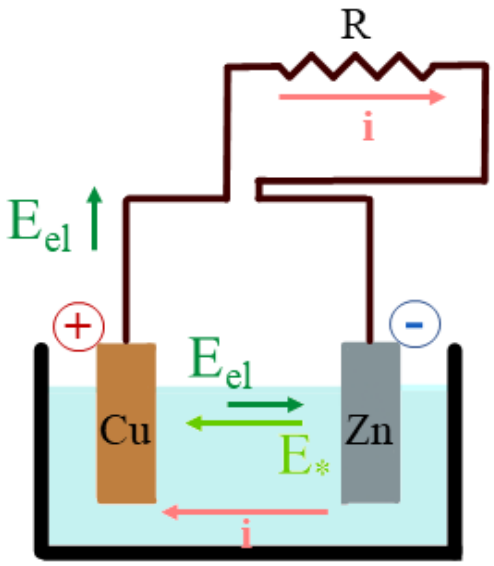

Figure 2.3 Voltaic pile. When the circuit is closed the electrochemical reactions occur continuously and the current flows.

The sum of the two electromotive fields, each generated by the half-reaction occurring, gives the total electromotive field, which allows for charge circulation in an opposite direction with respect to the electrostatic field.

The as-described system is different from the electrochemical devices presented in chapter two. In fact, with piles (or batteries) the energy stored in the chemical species (chemical energy is converted in electrical energy (as evidenced by the current flowing). The energy of the chemicals is used to perform electrical work on the charges being transferred. On the contrary, with electrolytic cells (as the CO_2 electroreduction cell), electrical energy is converted in chemical energy, stored inside the products of the electrochemical reactions. Unfortunately, the voltaic pile is not reversible, meaning that if one wants to make it work as an electrolytic cell for reducing zinc ions to metal atoms, it is not enough to just provide an external tension, higher than the electromotive field generated inside the cell. To make it reversible, the two electrodes must be immersed in solutions of their salts communicating by the means of a salt bridge which allow for ions exchange but avoid mixing the solutions (in this case copper is deposited on the surface of its electrode and zinc is dissolved from its electrode, following a similar mechanism of that occurring for the voltaic cell). In this modified configuration the cell takes the name of Daniell cell [82].

It would be now interesting to understand what is the relation between the chemical properties of the species involved in a cell, and the electromotive field generated. In particular, given any redox couples at the half-cells, thermodynamics must provide an answer for the following questions:

1. What are the spontaneous reaction occurring ?
2. What is the maximum theoretical voltage achievable from the cell ?

For the first question, it is expected that, as also happens for thermal systems, an electrochemical reaction is spontaneous when the change in the reaction free energy is negative, say when the reaction, proceeding brings to the minimum of the Gibbs free energy.

To answer the second question, a relation between the electrical work and the change in Gibbs free energy must be found. In fact it is known that, at constant temperature and pressure, the maximum non-expansion work a closed system can perform is given precisely by the change in Gibbs free energy (as shown below) [83].

From the definition of Gibbs free energy ($G = H - TS$), of enthalpy ($H = U + PV$) and internal energy ($U = Q + W$):

$$dG = dH - TdS - SdT = dU + d(PV) - TdS - SdT = dq + dw + d(PV) - TdS - SdT$$

If the process is reversible, from the definition of entropy ($dS = dq_{rev}/T$):

$$dG = dq_{rev} + dw_{rev} + d(PV) - TdS - SdT = TdS + dw_{rev} + d(PV) - TdS - SdT = dw_{rev} + d(PV) - SdT$$

Finally, if the work consists of expansion work ($-PdV$) and electrical work (dw_{el}):

$$dG = dw_{rev} + d(PV) - SdT = -PdV + dw_{el} + PdV + VdP - SdT = dw_{el} + VdP - SdT$$

This means that at constant temperature and pressure, the maximum (as the process is reversible) additional work (in this case electrical work) a system can provide is given by Equation 2.2:

$$dG = dw_{el} \qquad 2.2$$

Now comes the link with chemical reactions.

It is known that the change in Gibbs free energy for a reacting system (at constant temperature and pressure) is:

$$dG = \sum_i \mu_i dn_i = \sum_i \nu_i \mu_i d\xi = \Delta G_r d\xi \qquad 2.3$$

Therefore from the latter two equation one has:

$$dw_{el} = \Delta G_r d\xi \qquad 2.4$$

The electrical work is expressed as the product of a charge and the potential difference causing the charge to be displaced. In this case, the charge associated to the chemical reaction advancing, is that of the electrons being transferred. Since the extent of reaction is $d\xi$, the number of moles of electrons transferred is $\nu d\xi$ and the total number of electrons (intended as single entities) is $N_a \nu d\xi$ being $N_a = 6.022 \cdot 10^{23}$ the Avogadro number (entities per mole). The charge associated to this electrons is then just the product of the elementary charge and the total number of electrons $-eN_a \nu d\xi = -F\nu d\xi$, where F is the Faraday's constant expressed in unit charge divided by moles ($F = 96458\ C/mol$).

Accordingly, the electrical work will be:

$$dw_{el} = -\nu F E d\xi \tag{2.5}$$

Being E the potential difference. Finally, by comparing Equation 2.5 with Equation 2.4 the answer to the second question is obtained:

$$-\nu F E = \Delta G_r \tag{2.6}$$

which constitutes the link between reactions free energy and their related potential difference. Please notice that when the reaction is spontaneous, say when the reaction free energy is negative, the voltage is positive.

It is also important to revise the assumptions under which this relationship holds. The first one, is that the system, say the electrochemical device must operate reversibly. The second is that, when using the expression for calculating the physical quantities of interest, the composition of the system must be specified, as the reaction free energy is dependent on the composition of the system. When these conditions are verified, the potential difference granted by the cell is also called electromotive force emf.

Equation 2.6 can be conveniently rewritten as an explicit formula for finding the voltage by recalling the definition of reaction free energy:

$$\Delta G_r = \Delta G_r^o + RT \ln \prod_i a_i^{\nu_i} \tag{2.7}$$

and by defining the standard emf as follows:

$$E^o = \frac{-\Delta G_r^o}{\nu F} \qquad 2.8$$

Making these substitutions the Nernst Equation, relating the maximum potential achievable by an electrolytic cell, to the standard reaction energy (or equivalently to the equilibrium constant) and to the activities of the chemical species, is obtained:

$$E = E^o - \frac{RT}{\nu F} \ln \prod_i a_i^{\nu_i} \qquad 2.9$$

With reference to the Daniell cell example, the procedure for evaluating the cell potential starts with assuming a convention for writing the electrochemical reaction. From now on, it will be assumed that they are written towards the reduction sense. In this case the half-cell reactions will be:

$$Zn^{2+} + 2e^- \rightleftharpoons Zn \qquad \& \qquad Cu^{2+} + 2e^- \rightleftharpoons Cu$$

An assumption is made on where the reduction reaction will take place, i.e. on what of the two metals will constitute the cathode. In this case the copper half-cell is taken as cathode. The overall reaction is computed by subtracting the anodic reaction to the cathodic reaction:

$$Cu^{2+} + Zn \rightleftharpoons Cu + Zn^{2+}$$

To each of the two original half-reaction a reaction free energy is associated, assigned the temperature and the concentration of the species. Therefore for the additivity of the Gibbs free energy, and for Equation 2.9, the potential of the cell will be:

$$E_{cell} = E_{cathode} - E_{anode} = E^o_{cell} - \frac{RT}{\nu F} \ln \prod_i a_i^{\nu_i} \qquad 2.10$$

where this time the index "i" ranges over all the species of the cell. Again, if the potential of the cell turns to be positive than the reaction is spontaneous as the free energy of reaction is negative.

To effectively compute the potential two information are needed, the activities of the species and the standard potentials of the two cells. For determining the latter parameters the usual procedure is that of using a reference electrode for their direct measure. The concept of standard hydrogen electrode (SHE), which consists of a platinized Pt electrode and an acidic solution having unitary activity of H^+ through which gaseous H_2 is supplied at a fugacity of 1.00 bar [84], is conventionally used to set a reference scale with the value of 0 V is assigned to its potential. The reaction occurring inside the SHE is the hydrogen evolution reaction (HER) in acidic media (Equation 2.11).

$$2H^+ + 2e^- \rightleftharpoons H_2 \qquad 2.11$$

It is important to realize that the SHE is just a abstraction and in practice it cannot be constructed. Still it is indispensable for taking measures (more on how to measure the potential vs SHE can be found elsewhere [85]).

Another useful concept is that of reversible hydrogen electrode (RHE), formally constituted by the same components of the SHE, with the difference of allowing for any temperature, H^+ activity and H_2 fugacity. To see how does the RHE work, the Nernst equation is applied on it giving:

$$E_{RHE} = E^o_{SHE} - \frac{RT}{\nu F} \ln \prod_i a_i^{\nu_i} = E^o_{SHE} - \frac{RT}{F} \ln \left(\frac{\sqrt{f_{H_2} / p^o}}{a_{H^+}} \right) \qquad 2.12$$

where it is very clear how if the fugacity of H_2 is 1 bar and the activity of H^+ is 1, the RHE coincides with the SHE [86]. It follows that, if needed, it is possible to convert the potential of a half-cell measured with the RHE (E_{RHE}), to the potential of the cell measured with SHE (E_{SHE}) according to Equation 2.13:

$$E_{SHE} = E_{RHE} + E_{RHEvsSHE} \qquad 2.13$$

where the term $E_{RHEvsSHE}$ is the potential of the RHE measured with the SHE (coinciding with the second term of the right-hand side in Equation 2.12.

At last, let us conclude this part on thermodynamics with a practical example. It is required to compute the minimum voltage supplied to a CO_2 electroreduction cell for producing carbon monoxide, in alkaline media. At the cathode, carbon dioxide reduction will occur:

$$CO_2 + H_2O + 2e^- \rightleftharpoons CO + 2OH^- \qquad 2.14$$

$E^o = -0.10\ V\ vs\ RHE$ [28]

while inside the anodic chamber, the oxygen evolution reaction will occur:

$$H_2O + 1/2O_2 + 2e^- \rightleftharpoons 2OH^- \qquad E^o = +1.23\ V\ vs\ RHE \text{ [28]}$$

Therefore, utilizing the Nernst equation the voltage needed is:

$$E_{cell} = E_{Cat} - E_{An} = \left(E^o_{Cat} - E^o_{An}\right) - \frac{RT}{2F}\ln\left(\frac{P_{CO}P^{0.5}_{O_2}}{P_{CO_2}}\right)$$

Where if standard conditions are considered, the value of E_{cell} is just -1.33 V, meaning that electrical work must be provided from an external power supply to run the desired reaction, with at least (remember the reversibility) an applied voltage of 1.33 V.

So far equilibrium conditions were assessed, using exclusively thermodynamics concepts. Of course, as stated at the beginning of chapter 2, to get a complete description of the CO_2 reduction process, where a real current flows and electrochemical reactions occur, departure from equilibrium must be described too. To do so, a description of

reaction kinetics and transport phenomena occurring inside an electrochemical cell is required.

2.2. Kinetics

It is observed experimentally that when current is passed inside an electrochemical cell the potentials of the electrodes shift to new values. When considering for example the electroreduction of CO_2 to CO and the oxygen evolution reaction, the behavior will be qualitatively that of Figure 2.4.

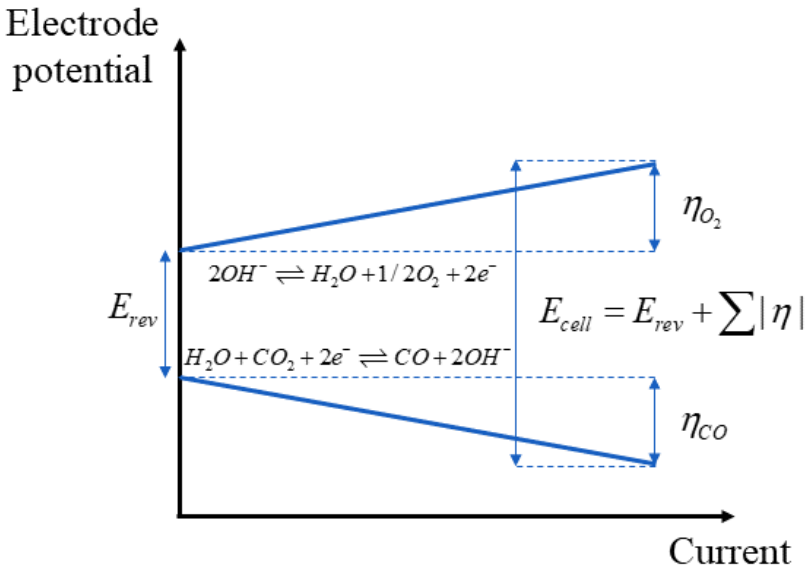

Figure 2.4 Qualitative representation of the change in the potential of the cathode and the anode when current is passed in the CO2 to CO reduction cell. The cathodic potential gets more negative while the anodic potential becomes more positive. Overall the voltage needed to drive the reaction increases. Adapted from *[87]*.

This departure from the equilibrium potential when the circuit is closed and current is passed, is historically named polarization of the cell and it represents dissipative losses [33]. The polarization is measured by the total overpotential:

$$\eta = E_{cell} - E_{cell,rev} \qquad 2.15$$

At low currents, the departing phenomenon is mainly associated with the limitations in the rate of electron transfer across the boundary between the electrode and the solution. This phenomenon is termed as electron transfer overpotential [87] (or activation overpotential). As the current in substantially increased, this step is no more the limiting one, as slow transport of species towards and away from the electrodes becomes the dominant rate limiting step (diffusion or concentration overpotential). Moreover, together with the charge-transfer step (responsible for the activation overpotential) there will be other coupled reactive steps whose activation energy can hinder the rate of the process (reaction overpotential).

Proceeding with the fashion of increasing current density, we may first investigate how to characterize the electron transfer overpotential. This is done with the Butler-Volmer equation, whose derivation (adapted from [87] and [88]) is now reported.

Consider the generic electrochemical reaction occurring at a half-cell (Equation 2.1). The potential energy surface of such a reaction is reported at a given applied potential E_1, in the dashed line of Figure 2.5.

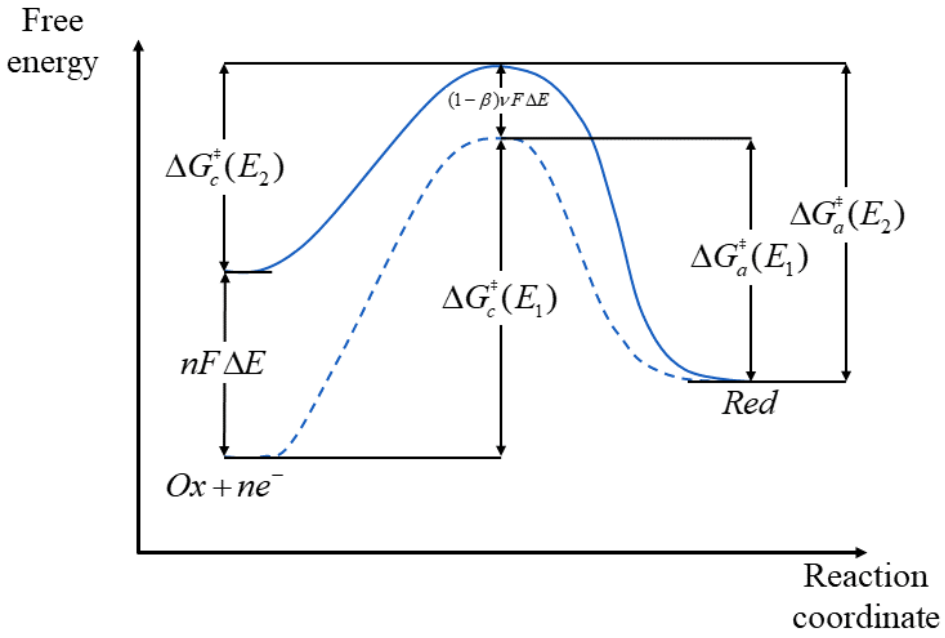

Figure 2.5 Potential energy surface for a generic electrochemical reaction. Oxidized and reduced species on the left and right of the transition state, respectively. Dashed line corresponds to the potential E_1, full lines correspond to the more negative potential E_2. Adapted from *[87]*.

Assuming a first order reaction rate for both the oxidation and reduction process the net surface reaction rate [mol/m^{2}s] is given by Equation 2.16 (the concentration of the

electrons is constant and therefore incorporated in the forward rate constant while the concentration of the active species is taken in correspondence of the electrode surface).

$$r = r_f - r_b = k_f C_{Ox}^{surf} - k_b C_{Red}^{surf} \qquad 2.16$$

Using the Faraday's law it is possible to convert the net reaction rate to a net current density, difference between the cathodic current density (reduction) and the anodic current density (oxidation):

$$j = j_c - j_a = \nu F\left(k_f C_{Ox}^{surf} - k_b C_{Red}^{surf}\right) \qquad 2.17$$

being ν the number of electrons exchanged.

Experimental evidence shows how varying the applied potential on the cell, significantly affects the reaction rate [88].

If for the rate constant an Arrhenius expression of the type:

$$k_f = A_f \exp\left(-\Delta G_r^{\ddagger} / RT\right)$$

is assumed, then by changing the reaction free energy towards of the formation of the transition state the rate constant changes accordingly. In an electrochemical reaction, where electrons participate as species, it is possible to change their energy (and consequently the reaction free energy) by changing the applied potential. For example in Figure 2.5 it is shown how making the potential applied to an electrode more negative from E_1 to E_2, the free energies of the cathodic reaction (or reduction reaction) and anodic reaction (or oxidation reaction) change according to Equations 2.18 and 2.19, respectively. The reason of these changes is that when the potential is shifted by ΔE to a new value, the relative energy of the electrons resident on the electrode changes by $-\nu F\Delta E$ (electrical work on a charge associated to ν moles of electrons) [88]. The energetic content of the transition state also resent of this change and for simplicity it is assumed that of the total energy added by the increase in the potential, only a fraction $(1-\beta)$ is retained by the transition state itself.

$$\Delta G_c^{\ddagger}(E_2) = \Delta G_c^{\ddagger}(E_1) + \beta \nu F \Delta E \qquad 2.18$$

$$\Delta G_a^{\ddagger}(E_2) = \Delta G_a^{\ddagger}(E_1) - (1-\beta) \nu F \Delta E \qquad 2.19$$

If now for the potential E_1 the standard potential E^0 is chosen, the related reaction free energy will be the standard free energy. By choosing this reference and by plugging Equation 2.18 in the Arrhenius expression we get:

$$k_f(E_2) = k_f(E) = A_f \exp\left(-\Delta G_c^{o,\ddagger} / RT\right) \exp\left[-\beta \nu F \left(E - E^o\right) / RT\right] \qquad 2.20$$

where the subscript 2 has been removed for generalization purposes. Similarly for the backward reaction we get:

$$k_b(E) = A_b \exp\left(-\Delta G_a^{o,\ddagger} / RT\right) \exp\left[(1-\beta) \nu F \left(E - E^o\right) / RT\right] \qquad 2.21$$

The first two terms of both the Equations just written represent the rate constant when E is equal to the standard potential E^0. Now consider the special case in which the interface is at equilibrium with a solution in which $C_{Ox} = C_{Red}$. In this situation, $E = E^0$ and $k_f C_{Ox} = k_b C_{Red}$, so that $k_f = k_b$. Thus, E^0 is the potential where the forward and reverse rate constants have the same value, named standard rate constant k^0 [88]. Under these considerations we may finally write by using Equation 2.17 the net current density as in Equation 2.22, also called current-potential characteristics.

$$j = \nu F k^o \left\{C_{Ox}^{surf} \exp\left[-\beta \nu F \left(E - E^o\right) / RT\right] - C_{Red}^{surf} \exp\left[(1-\beta) \nu F \left(E - E^o\right) / RT\right]\right\} \qquad 2.22$$

From here it is possible to show how at equilibrium the Nernst equation is recovered, conferring consistency to the derivation provided.

Further manipulation of Equation 2.22 will be provided in the chapter 2.3, to add on top of the discussion developed so far, the effect of transport limitations on the current density

2.3. Transport

At first the effect of transport limitations on surface reactions is discussed with a practical toy problem of reaction and diffusion in series. Then, after having introduced the effective medium approximation, the equation of continuity for a binary mixture is derived, as it will constitute the starting point for solving the diffusion problem inside the reconstructed virtual domain. At last, the concentration overpotentials, say the effect of a local change of species concentration close to the electrode on the cell voltage, will be introduced.

As discussed in chapter 2, inside a CO_2 electroreduction cell the charge transfer reactions (electrochemical reactions) occur on the surface of the catalyst nanoparticles dispersed within the CL. The nanoparticles are surrounded by a thin liquid film through which the dissolved CO_2 diffuses to reach the active sites. To qualitatively understand why transport phenomena can constitute a limitation for those reactions, the system depicted in Figure 2.6 can be considered as a highly simplified representation of the wetted nanoparticle surface.

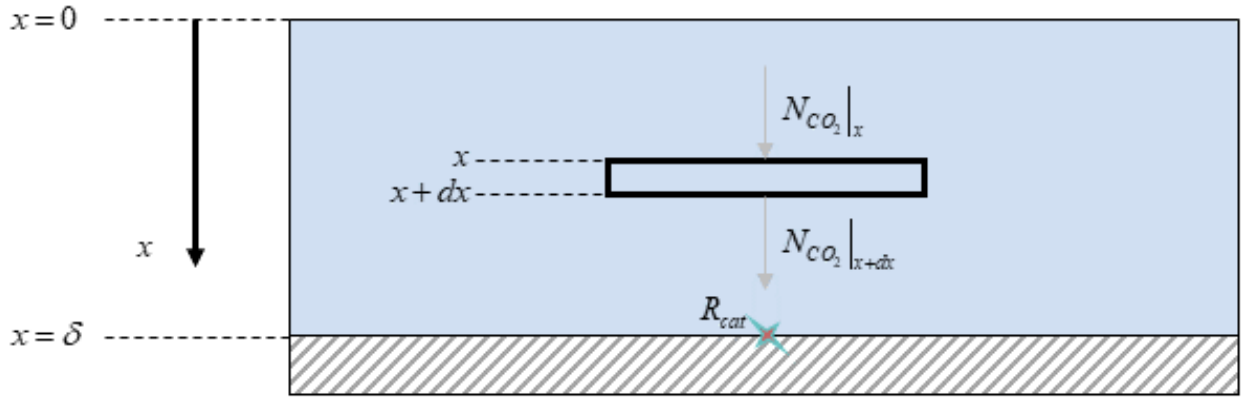

Figure 2.6 Reaction and diffusion in series. CO2 diffuses towards the catalytic surface in order to get reduced to CO.

The CO_2 is dissolved from the gas in the liquid phase and once it reaches the catalytic surface it gets reduced, e.g. to carbon monoxide. It is possible by performing a shell mass balance to obtain the diffusive flux and the concentration profile of carbon dioxide. A unimolecular reaction rate of the form:

$$R_{cat} = kC_{CO_2}$$

is assumed, where k is the rate constant expressed in m/s.

Three species are simultaneously present in the liquid, CO_2, CO and the liquid assumed to be a unique pseudo species. If the latter assumption is valid and the CO does not interfere with the binary diffusion of CO_2 inside the liquid, the molar flux of the gas can be expressed considering an unit area fixed in space as in Equation 2.23 [89].

$$N_{CO_2} = -c_{tot} D_{CO_2/H_2O} \frac{dy_{CO_2}}{dx} + y_{CO_2}\left(N_{CO_2} + N_{H_2O}\right) \qquad 2.23$$

where the second term can be neglected due to the small molar fraction of CO_2 in aqueous systems.

Therefore, from the shell material balance, in absence of sources/sinks in the bulk, one can get:

$$N_{CO_2}\Big|_x - N_{CO_2}\Big|_{x+dx} = 0 \qquad 2.24$$

which brings, after having performed a first order Taylor expansion of the second term, centered in x, to discover that the flux is constant:

$$dN_{CO_2} = 0 \quad \rightarrow \quad N_{CO_2} = const.$$

The boundary conditions to be enforced are:

$$\begin{cases} C_{CO_2}(x=0) = C^o_{CO_2} = 34 \ mM \\ N_{CO_2}(x=\delta) = kC_{CO_2}(x=\delta) \end{cases}$$

whose related solution in terms of flux and CO_2 concentration is reported in Equation 2.26 and Equation 2.26 respectively.

$$N_{CO_2} = \frac{C^o_{CO_2} D_{CO_2/H_2O}}{\delta} \frac{Da}{1+Da} \tag{2.25}$$

$$C_{CO_2}(x) = C^o \left(1 - \frac{Da}{1+Da} x/\delta\right) \tag{2.26}$$

Where the Damköhler number (Da) has been defined as:

$$Da = \frac{k}{D_{CO_2/H_2O}/\delta}$$

The feature of the two processes of diffusion and reaction being in series is captured by the emergence of the Damköhler number, which constitutes a ratio between the rate of reaction and the rate of diffusion. In Figure 2.7, different CO_2 concentration profiles achieved when varying the Damköhler number are plotted. The Damköhler number is a combination of three parameters. Apart from the diffusivity of the CO_2 in water (for this model assumed to be $1.91 \cdot 10^{-9}$ m^2/s at 293.15 K [38]) which is a weak function of the temperature, the two parameters on which one can act for maximizing the consumption rate of CO_2 are the rate constant k (in this case assumed to be a convenient value of $1 \cdot 10^{-4}$ m/s), dependent on the activity of the catalyst, and the thickness of the diffusion layer δ. The purpose of the toy problem is to show what happens to the consumption rate of carbon dioxide when the thickness δ spans three order of magnitudes, going from 100 nm to 500 μm, say when the CO_2 electroreduction is conducted in a GDE rather than in a conventional H-cell. With these assumptions the Damköhler number is correspondently varied between $5 \cdot 10^{-3}$ to 25.

By looking at the figure, when Da<<1 the process is not limited by the diffusion of CO_2 but by the speed of the reaction (determined by the rate constant k). A steep gradient in the concentration of CO_2 is observed as the molecules have to travel a short path to get consumed. As $\delta \to 0$ the consumption rate assumes its maximum value, being equal to the reaction rate evaluated at the gas/liquid equilibrium concentration $C^0_{CO_2}$. Conversely, when the thickness of the diffusion layer is increased, the gradient in the concentration of CO2 (say the consumption rate) gradually decreases. The asymptotical behavior in this case tells that as $\delta \to \infty$ the consumption rate approaches 0. In fact, in order to reach the

active sites and react upon them, carbon dioxide has to slowly travel a long path, after which it gets rapidly consumed. In this case the system is said to be in its mass transfer diffusion limit, meaning that the overall rate of the process is limited by the concentration-driven slow movement of the molecules. It can be concluded then that maximizing the surface concentration of CO2, which maximizes the surface reaction rate at a fixed rate constant, means working in kinetic regime by ensuring a small Damköhler number, which in turns is achieved by ensuring a small thickness of the diffusion layer. As anticipated in chapter 2, the latter is one of the reasons behind the success of the GDE configuration, which has been able to reduce the thickness of the diffusion layer by at least 3 order of magnitude.

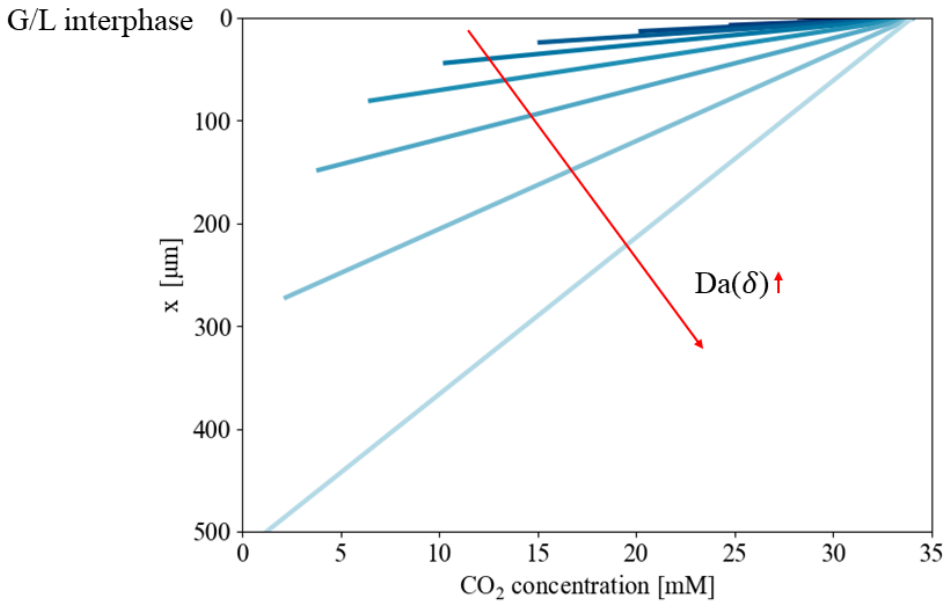

Figure 2.7 Diffusion and catalytic reaction of CO2 in aqueous system. CO2 concentration profiles when varying the Damköhler number by changing the thickness of the diffusion layer δ.

While we start witnessing the importance of transport phenomena in industrial chemical processes and more specifically in CO_2 electrolysis, we have to remember that before reaching the liquid present inside the catalyst layer, CO_2 has a wide portion of gas diffusion layer to cross (≈200 μm). From an intuitive point of view, the physics of carbon dioxide inside the GDL is very similar to its diffusion in the aqueous solution. There is a path to travel and a sink at the end of the path. In the latter case the sink is constituted by the CO_2 consumption by charge transfer reaction while in the former case it is represented

by the dissolution of the gas inside the liquid. Nevertheless, there is an important difference between the two processes (other than the dissolved gas homogeneous consumption that for simplicity was neglected in the toy problem). In the process of CO_2 diffusion inside the GDL two parameters can be used to keep low what would be a properly defined Damköhler number for this domain. The first one, as happened also for the CL, is the thickness of the GDL. The second one is the diffusivity of CO_2 which now depends on the morphological characteristics of the GDL, as in accordance with the effective medium approximation.

Simply stated the effective-medium approximation is a method for dealing with a "macroscopically inhomogeneous medium, i.e., a medium in which quantities such as the conductivity , dielectric function , or elastic modulus vary in space" [90]. By "dealing" it is meant to solve transport (matter, momentum and energy) problems in a simpler, nonetheless effective way.

For introducing the topic, an intuitive and familiar case-study may help in the understanding of the issue to be addressed.

It is needed to compute the total heat flowing through a composite wall made of two different materials, arranged as shown in Figure 2.8 **a**.

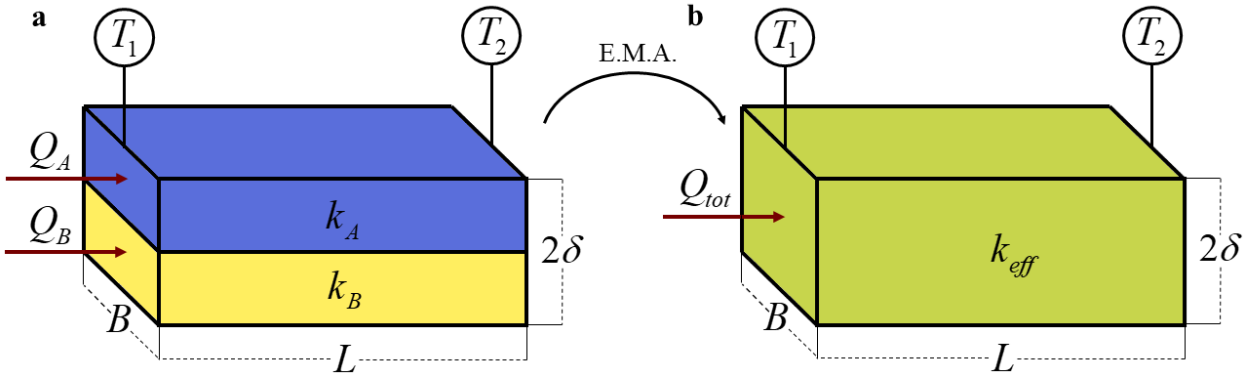

Figure 2.8 Toy problem for explaining the effective medium approximation (E.M.A.). **a**, The composite material before the E.M.A. appears as a heterogenous media **b**, The composite material after the E.M.A. appears as a homogenous media with a unique effective transport property.

The left and right sides of the walls are kept at constant temperature T_1 and T_2, materials A and B have a thermal conductivity of k_A and k_B [W/mK] respectively. The cross section through which the heat is flowing is the same for both the material and equal to the product of the quantities indicated by δ and B. All the remaining lateral walls are insulated.

From a shell heat balance, not different in its physical meaning from the one performed in the case of Figure 2.6, one can get the heat Q_i [W] flowing in the two slices of materials A and B.

$$Q_i = \frac{k_i \cdot A}{L}(T_1 - T_2) \qquad 2.27$$

The total heat transferred can be obtained by summing Q_A, and Q_B and an effective conductivity can be conveniently introduced as shown in Equation 2.28.

$$Q_{tot} = Q_A + Q_B = (k_1 + k_2) \cdot \frac{A}{L}(T_1 - T_2) = k_{eff} \cdot \frac{A}{L}(T_1 - T_2) \qquad 2.28$$

So from a macroscopic perspective, as shown in Figure 2.8 b, it is possible to treat the composite wall, heterogeneous in its properties, as a homogenous material characterized by unique effective transport properties.

Is it possible from these basic considerations to develop a general method, suitable for calculating an effective transport property in whatever composite geometry ? Following the rationale of the case-study, the goal is to represent the total heat exchanged utilizing an effective conductivity to be plugged in a simple expression as the one in Equation 2.28 (rightmost expression). This heat then has to be matched with the sum of the two heat flowing in the separated materials which can be obtained by integrating the heat flux q [W/m^2] over a generic cross section of the composite material, perpendicular to the heat flow (as in steady state, in absence of source/sinks of heat, the heat flux is constant). In mathematical terms:

$$total\ heat\ exchanced = k_{eff} \cdot \frac{A}{L}(T_1 - T_2) = \int_{A^*} \boldsymbol{q} \cdot d\boldsymbol{A}^* \qquad 2.29$$

Equation 2.29 provides a general expression for evaluating k_{eff}. From there it is easy by utilizing the Fourier's constitutive law, to show how the integration of the rightmost term provides for the case-study previously shown the sum of Q_A and Q_B.

Imagine now to have a complex geometry for which it is not possible to solve analytically the integral of Equation 2.29. The cross section will be divided in many small facets and the integral will become a sum extended to all the small areas of the facets, as shown for a generic scalar field in Equation 2.30 (finite difference formulation):

$$k_{eff} \cdot \frac{A}{L}\left(\phi_1 - \phi_2\right) = \int_{A^*} \boldsymbol{J} \cdot d\boldsymbol{A}^* = \int_{A^*} -k\nabla\phi \cdot d\boldsymbol{A}^* = \sum_i -k\frac{\Delta\phi_{x,i}}{\Delta x}A_i \qquad 2.30$$

where being the area perpendicular to the one of the three coordinates (e.g. x), only one component of the flux **J** has been considered (in principle the cross section is not oriented perpendicularly to a specific coordinate. Then the scalar product between the normal to the section and the flux will provide the relevant components of the flux to consider). Once the right-hand side of Equation 2.30 is known, say when the scalar field in the medium is known, the effective transport property can be computed.

So in order to compute the effective transport properties, the scalar field of the physical quantities being transported at steady state needs to be reconstructed. For a complex geometry such as the one of gas diffusion layer, this information can be exclusively be retrieved with numerical methods.

To obtain the partial differential equation governing the transport of a passive scalar (e.g. CO_2 gas concentration in the GDL), consider the volume element in Figure 2.9.

The molar fluxes multiplied by the area of the face through which matter penetrates and leaves the volume element is equal to the quantity of matter accumulated inside the small cube (reactions are not accounted for in the gas diffusion layer).

Mathematically this is translated in the following expression.

$$N_{Ax}\big|_x \Delta y\Delta z - N_{Ax}\big|_{x+\Delta x} \Delta y\Delta z + N_{Ay}\big|_y \Delta x\Delta z - N_{Ay}\big|_{y+\Delta y} \Delta x\Delta z + N_{Az}\big|_z \Delta x\Delta y - N_{Az}\big|_{z+\Delta z} \Delta x\Delta y = \frac{\partial C_A}{\partial t}\Delta x\Delta y\Delta z$$

Dividing by the whole expression by the volume and performing a first order Taylor expansion it is possible to get Equation 2.31.

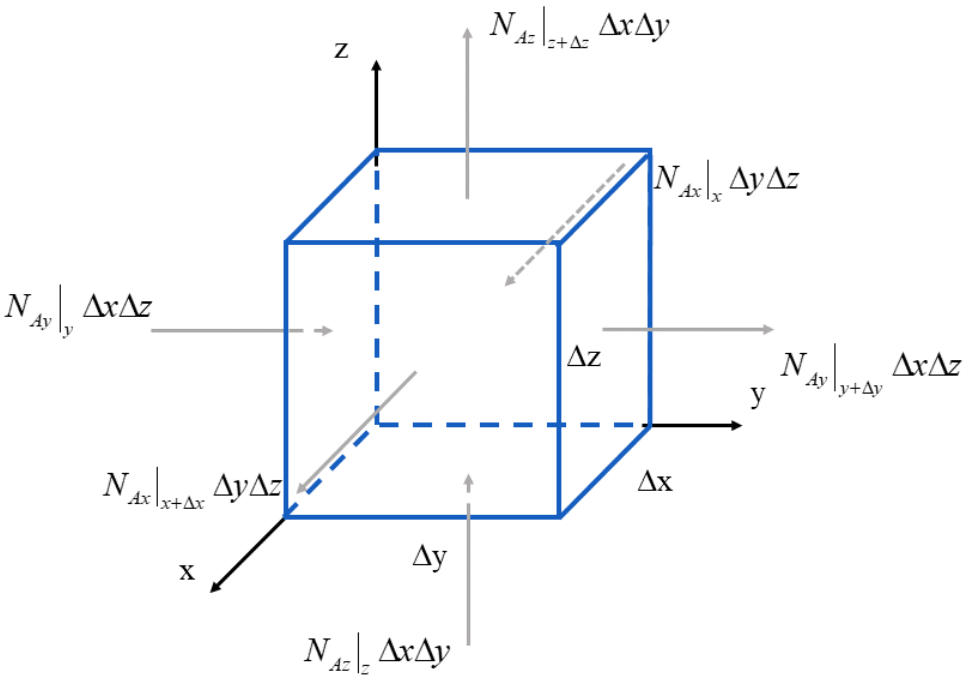

Figure 2.9 Volume element for material balance of binary mixture (species A and B). The molar flux of species A is a vector quantity of three component, N_{Ax}, N_{Ay}, N_{Az}.

$$\frac{\partial C_A}{\partial t}+\frac{\partial N_{Ax}}{\partial x}+\frac{\partial N_{Ay}}{\partial y}+\frac{\partial N_{Az}}{\partial z}=\frac{\partial C_A}{\partial t}+\nabla\cdot \boldsymbol{N_A}=0 \qquad 2.31$$

where the divergence operator,$\nabla=\left(\frac{\partial}{\partial x},\frac{\partial}{\partial x},\frac{\partial}{\partial x}\right)$ has been conveniently introduced.

In order to utilize the equation a closure model for the molar flux is needed. If considering binary diffusion Fick's law may help in writing the diffusive part of the flux:

$$\boldsymbol{N_A}=-D_{AB}C_{tot}\nabla x_a+C_A v^* \qquad 2.32$$

v* being the molar averaged velocity. By substituting 2.32 in 2.31:

$$\frac{\partial C_A}{\partial t}+\nabla\cdot C_A v^*=+\nabla\cdot D_{AB}C_{tot}\nabla x_A \qquad 2.33$$

If the following assumptions are considered:

- Steady state
- Uniform diffusivity
- Uniform concentration
- Absence of convective transport

The Laplace equation is obtained.

$$\nabla^2 C_A = 0 \qquad 2.34$$

Similarly, it is possible to obtain an equivalent equation for the temperature and electric potential scalar fields. This equation constitutes the starting point for the implementation of the numerical algorithm needed to compute these fields. More information about this part will be provided in the method chapter.

For concluding the theoretical digression dedicated to transport phenomena, we may briefly discuss how these affects the reaction rate through the so called concentration overpotentials.

Recall from chapter 2.2 that the current-potential characteristics describes how the current density changes according to the applied potential E. Despite the importance of the equation, we might introduce slight modifications to it in order to make explicit the distinction between the bulk and surface concentration of the species involved. This difference, if present, is representative of the so called concentration overpotential (coming from the fact that, as predicted from the Nernst equation, a difference in electrical potential between two location in the electrolytic solutions exists whenever there is a gradient in the concentration of the active species among the two points).

We define exchange current density j_0 as the current density at equilibrium. From Equation 2.22 j_0 turns to be:

$$j_o = \nu F k^o C_{Ox} \exp\left[-\beta \nu F \left(E - E^o\right) / RT\right] \qquad 2.35$$

where due to the equilibrium the concentration at the surface is the same as that in bulk ($C^{surf} = C$). We note now that the exponential term of the right-hand side can be also written in terms of the ratio between the concentrations of the reduced and oxidized species thanks to the Nernst Equation:

$$\exp\left[-\beta\nu F\left(E-E^{o}\right)/RT\right]=\left(\frac{C_{Ox}}{C_{Red}}\right)^{-\beta} \qquad 2.36$$

so that Equation 2.35 now is:

$$j_o=\nu F k^{o}\frac{C_{Ox}^{1-\beta}}{C_{Red}^{\beta}} \qquad 2.37$$

Finally, dividing the current-potential characteristics (Equation 2.22) by Equation 2.37 the concentration-dependent Butler Volmer equation is obtained (Equation 2.38). In its original form the dependence on the concentration is not present, as it is assumed that the bulk concentration of the active species is the same as that on the electrode surface (valid for low enough current densities).

$$j=j^{0}\left[\frac{C_{Ox}^{surf}}{C_{Ox}}\exp\left(-\frac{\beta\nu F}{RT}\eta\right)-\frac{C_{Red}^{surf}}{C_{Red}}\exp\left(\frac{(1-\beta)\nu F}{RT}\eta\right)\right] \qquad 2.38$$

The equation relates the overpotential applied to the net current density flowing inside the cell. According to the sign of the overpotential a cathodic (positive) or anodic (negative) current will flow. When the overpotential becomes sufficiently high, being it negative or positive, it is clear that one of the two terms of Equation 2.38 becomes negligible with respect to the other. As an example, for ν being equal to 1 and a reduction process occurring, this may happen, in practice, when the following condition is respected:

$$\exp\left(\frac{(1-\beta)\nu F}{RT}\eta\right)/\exp\left(-\frac{\beta\nu F}{RT}\eta\right)=\exp\left(\frac{F}{RT}\eta\right)<0.01$$

say when η < - 118 mV at 25 °C. In these conditions the rate equation can be written according to the so called Tafel kinetics as shown in Equation 2.39.

$$j=j^{0}\frac{C_{Ox}^{surf}}{C_{Ox}}\exp\left(-\frac{\beta\nu F}{RT}\eta\right) \qquad 2.39$$

In its concentration independent form (say when the concentration of the oxidized species is uniform throughout the electrolyte), the Tafel equation constitute an important tool for deriving experimentally the values of J^0 and β. In the current work, Equation 2.39 will be used to describe the kinetics of the charge transfer reaction. In fact, under the assumption that the overpotential is sufficiently high, only CO_2 reduction occurs as an irreversible process.

3 Methods

The subsequent sections delve into the methodology employed to conduct the study. Following the key stages outlined in Figure 1.17, the construction process of the geometry is elaborated in detail. Subsequently, the procedure for morphological and transport validation is discussed, and finally, the approach to obtaining the correlations is also elucidated.

3.1. Geometry construction

The development of a stochastic model incorporating actual microstructural parameters for reconstructing the gas diffusion layer was pioneered by Schulz et al. [66]. While certain aspects of their approach have influenced the current work, there are notable distinctions. As an example, one significant difference pertains to the modeling of the binder. In the original work, the carbonaceous binder, described in chapter 1.2.5 as a phenolic resin used to bind the fibers together, was not considered. However, in the present work, the inclusion of the binder material allows for a convenient division of the geometry generation into two distinct macro steps:

1. Skeleton generation
2. Binder addition

where skeleton is referred to the geometry constituted of PAN fiber only.

3.1.1. Skeleton generation

For constructing the skeleton, the process involves creating an arrangement of randomly distributed fibers positioned in the x-y plane. These almost two-dimensional layers (in reality a fiber is by itself a 3D object, but each fiber layer mainly extends in the

x-y plane) are then stacked on top of each other (as in the manufacturing process, where many sheets are compressed together) to construct the three-dimensional structure.

To generate this structure, it is crucial to emphasize the underlying assumptions regarding the geometric characteristics. The main assumptions made in this regard are:

1. Fibers are spread throughout the three dimensional space. The position of a fiber in a specific fiber layer is completely determined by two parameters, an in-plane (x-y) angle ϑ and the distance from the center of the computational domain r, as shown in Figure 3.1;
2. ϑ and r are sampled randomly for each single fiber, from a uniform distribution (meaning that each possible distance from the center of the domain, as each possible angle from the reference angle, are equally likely to be picked for a given fiber);
3. Fibers are modelled as infinitely long straight cylinders (hence every fiber will cross the entire computational domain and not end abruptly inside it);
4. All the fibers have the same diameter. The additional complexity of incorporating a diameter distribution is not very meaningful without clear manufacturing process data, and has been set aside for future work;
5. Fibers interactions are modeled by allowing them to interpenetrate each other; the soft carbon fibers bending and compressing near junctions have not been considered;
6. The entire GDL is generated in the z-direction (i.e. along the through-plane direction. See Figure 3.14) by stacking different fiber layers (each formed in x-y plane) on top of each other. Each layer penetrates the neighboring ones by a distance of 6% of the fiber diameter (to avoid singular contact points between fibers of consecutive layers). This replicates the physical process of fibers layers being eventually compressed to form the paper and also helps in avoiding having contact points which would cause numerical problems during the meshing phase of the geometry;
7. Each fiber layer is populated by approximately the same number of fibers (it is possible that during the cropping process, in which the fiber stack is cut to be fitted in into the computational domain, some fibers are left outside the selected area).

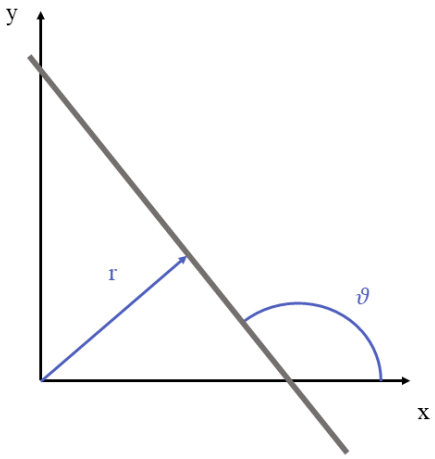

Figure 3.1 Polar coordinates for fiber generation. The position of each fiber is completely determined once the angle ϑ and the distance from the center r are assigned.

The generation process consists of multiple distinct steps, which can be better understood by referring to Figure 3.2. This figure illustrates the complete workflow for skeleton generation, providing an algorithmic representation of the iterative procedure involved. The whole pipeline has been implemented in Python, which execute the different software and manages the data files.

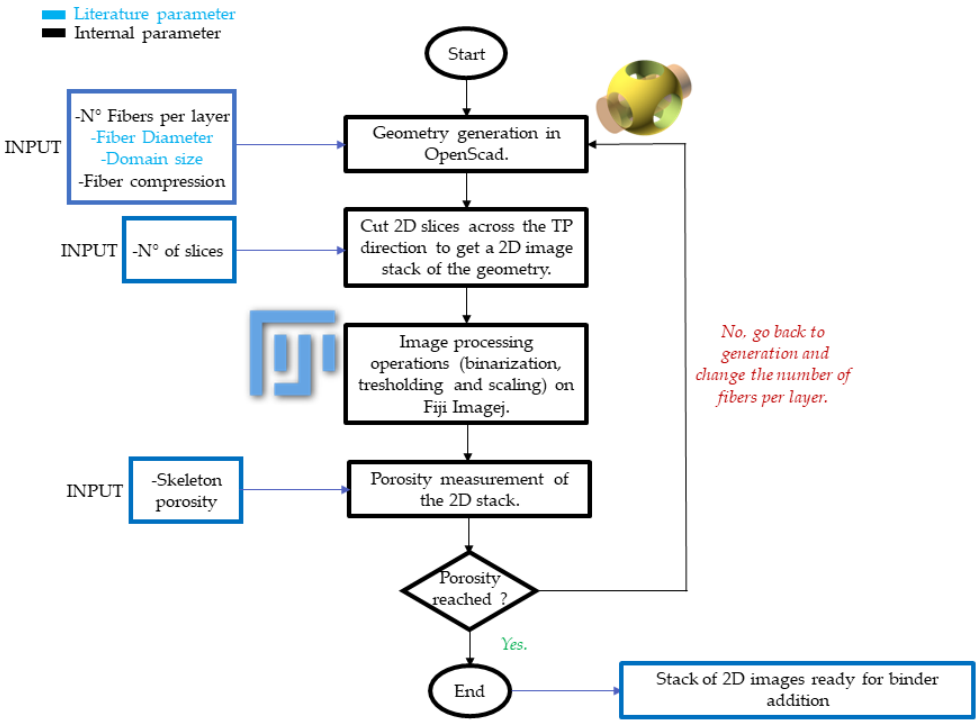

Figure 3.2 Skeleton generation algorithm. From microstructural parameters to 2D image stack.

The first step is the geometry generation, conducted in OpenSCAD, an open-source computer-aided design (CAD) software specifically developed for creating parametric designs, where objects can be defined and modified using a scripting language rather than a visual interface [91]. OpenSCAD receives as input the geometry generation parameters such as manufacturing specifications (e.g. the fiber diameter) and other model-specific computational parameters such as the number of fibers for each layer, the desired domain size and the compression of the fibers (which controls the interpenetration of consequent fiber layers, without changing their shape). From a conceptual standpoint, the procedure can be visualized Figure 3.3, which illustrates the fundamental building blocks of the geometry: a straight cylinder representing a fiber, a planar arrangement of fibers constituting a layer, and ultimately stacks of layers forming the simulation domain. The number of fiber layers to be stacked is back-calculated using the thickness of the GDL, the fiber diameter and the interpenetration distance between the layers. Once the diameter of the fibers and carbon paper thickness are known (from manufacturing spec. sheets), the interpenetration distance between the layers is fixed and the required number of layers is computed to match the desired GDL thickness.

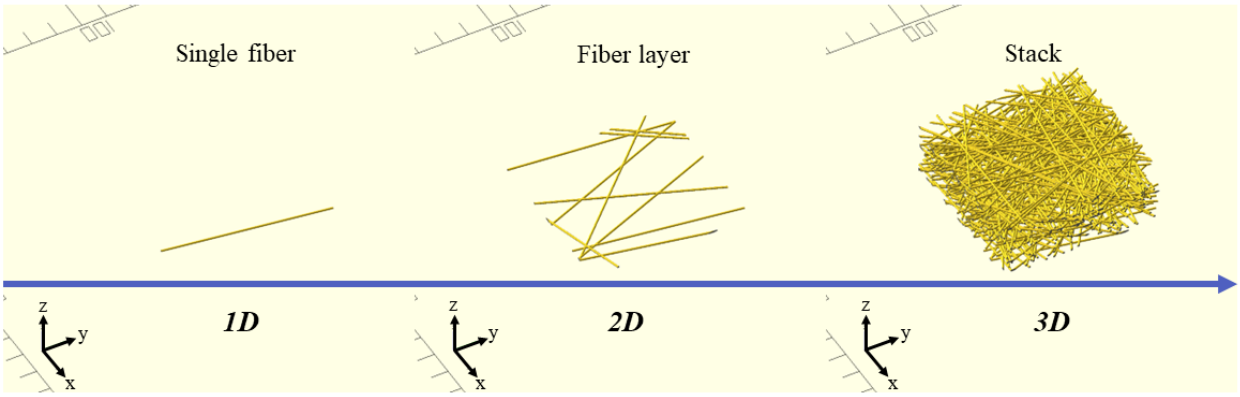

Figure 3.3 OpenSCAD generation of the skeleton. From a single fiber to the full 3D stack.

The virtual geometry can be rendered and exported in the form of an stereolithography (STL) file and utilized by the CFD simulations. Nevertheless, for the entire geometry we have observed direct rendering from OpenSCAD results in impractical computational times (since OpenSCAD rendering is not parallelized by default, an initial solution was developed to lock different cores of the CPU individually and run parallel instances of OpenSCAD in each core to render sections of the geometry simultaneously). However, generating the binder material in the stage of binder addition

requires the virtual geometry to be converted in a stack of two-dimensional images. Hence, rather than rendering the geometry into an stl file and again reconverting it back to an image stack, screenshots of the virtual geometry were captured using the virtual camera tool in OpenSCAD and the image stack was directly generated.

Following the algorithm depicted in Figure 3.2, this is done by slicing the geometry into a specified number of slices, as defined by the user. The number of slices is determined based on the requirement of the through-plane resolution [pixel/μm]. In the current work a resolution of 1 μm/pixel has been assumed as this value is close to the computational tomography based methods used to experimentally visualize the geometry (it was further noticed that increasing this resolution did not significatively affect the computed porosity of the sample).

The produced image stack is exported to the open-source image processing software Fiji-ImageJ [92]. Here, the images are first cropped to remove the background in excess (residue of the slicing procedure employed) and then thresholded to get a binary image stack. This series of operations is shown in Figure 3.4.

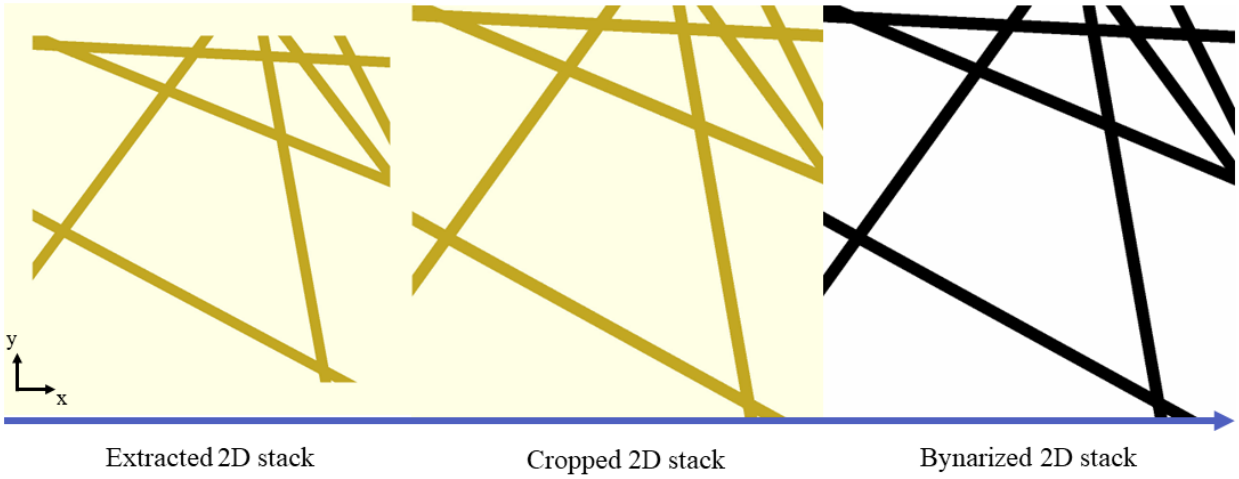

Figure 3.4 Image processing with Fiji ImageJ. After the porosity check, the binarized 2D stack is ready for the binder addition.

Once the binary stack is produced, an assessment on the skeleton porosity of the sample is executed (more information on the meaning of the skeleton porosity will be provided in the subsequent chapter). The porosity at this stage is calculated as the ratio between the white pixels (void space) and the total number of pixels of the stack. If the porosity matches with the desired value ($\pm$ a tolerance of 0.6-0.9%) then the skeleton generation is completed and the user can proceed with the binder addition. Instead, if the

porosity check fails, the optimization loop forces the routine to restart from the geometry generation in OpenSCAD. The optimization loop works by varying as a unique degree of freedom, the number of fibers per layer. Therefore, until the exit condition posed by the porosity check is not verified, the optimizer will try to change the number of fibers per layer until getting reasonably close to the desired value.

3.1.2. Binder addition

Analogous to the skeleton generation, the binder generation procedure algorithm is shown in Figure 3.5.

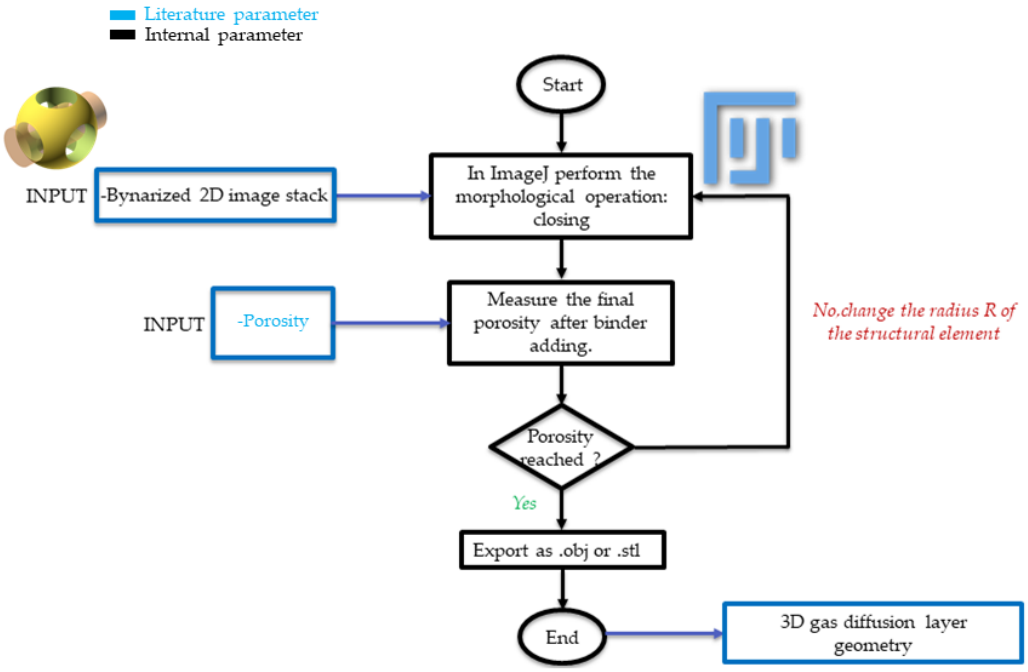

Figure 3.5 Binder addition algorithm from the 2D image stack to the final 3D geometry.

The addition of binder is performed in Fiji ImageJ via image processing by applying morphological operations (the CPU-based operations are available through the Fiji ImageJ plugin MorphLibJ [93]). To speed up the process, particularly needed when large geometries are considered, the GPU-accelerated image processing plugin Clij2 has been utilized [94].

Morphological operations are a set of image processing techniques that are used to manipulate the shape and structure of objects in an image. Some applications of

morphological operations are for example image denoising, image filtering, segmentation, object recognition and so forth. In a morphological operation the value of each pixel (black or white in a binary image) in the output image is updated based on a comparison of the value of the corresponding pixel with its neighbors [95]. The image comparison or probing is performed using a probing agent known as the "Structuring Element" (SE). The SE can have any shape, and to complete the operation, it must scan the entire image, pixel by pixel (or voxel by voxel in 3D).

The two fundamental morphological operations are dilation and erosion. Dilation expands the boundaries of objects in an image, making them larger and more connected. Erosion, on the other hand, shrinks the boundaries of objects, making them smaller and removing small details. Mathematically the dilation operation is a Minkowski sum while the erosion operation is a Minkowski subtraction. Both are defined in Equation 3.1 and Equation 3.2 respectively.

$$X + Y = \bigcup_{y \in Y} (X + y) \tag{3.1}$$

$$X - Y = \bigcap_{y \in Y} (X - y) \tag{3.2}$$

where X and Y are two sets of points in the Euclidean space and y is the generic point belonging to the set Y [96].

To demonstrate the impact of these two operations, a single slice from the stack of the 2D images obtained after the completion of the skeleton generation algorithm is utilized as the set X. In Figure 3.6 the results of the erosion and dilation operation achieved by using a circular SE (the set Y) are shown. It has to be noted that alternately taking the sum and difference with Y is not necessarily equivalent, meaning that:

$$(A - B) + B \subseteq A \quad \textit{and} \quad (A + B) - B \supseteq A$$

which translated in simple terms means that the Minkowski sum has the ability to bridge gaps that cannot be reopened by the Minkowski difference, while the Minkowski difference can eliminate small islands that the sum cannot recreate from scratch [97].

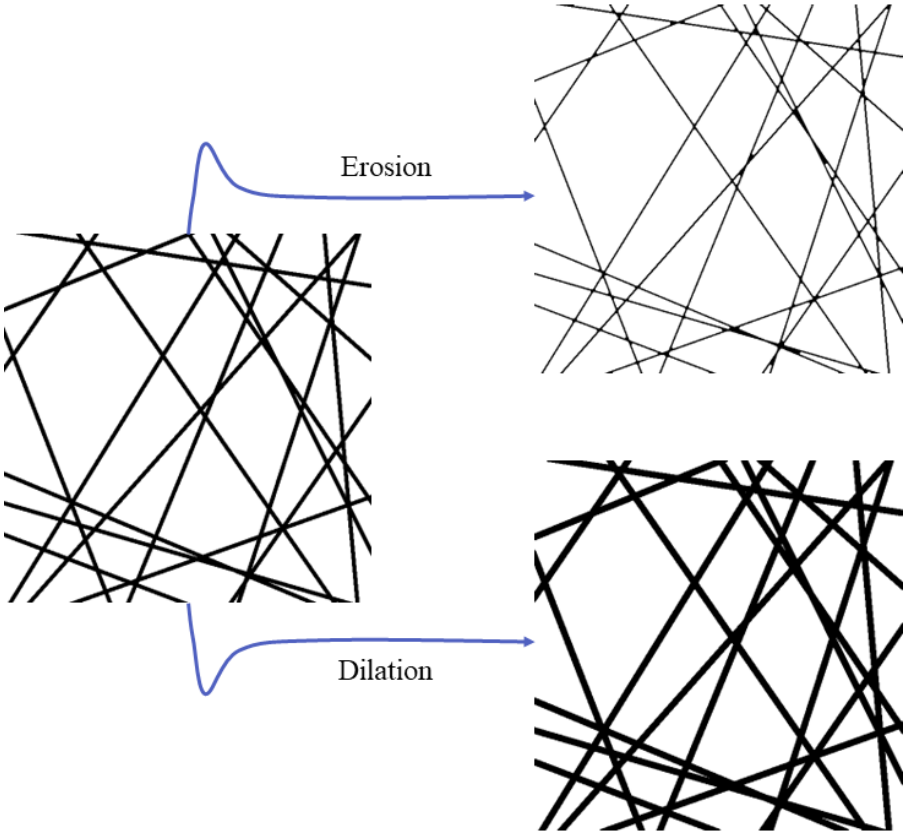

Figure 3.6 Erosion and dilation morphological operations, applied separately on a single slice of the 2D stack. The SE utilized in this case is circular, with radius equal to 2. As visible from the slices, erosion has the effect of thinning the fibers while dilation enlarges them.

Consequently, by combining these two operations in series, it is possible to obtain two different results: the opening (erosion followed by dilation) and closing (dilation followed by erosion) operations. The closing operation is of particular interest when it comes to adding binder, as it serves the purpose of filling small holes while maintaining the original shape and size of larger holes and objects in the image [98]. It must be noted here, that this image processing manipulation for binder generation has to pertain to the physical behavior of the resin on the carbon fibers. It is well known that due to its wetting nature, binder tends to accumulate at the intersection between distinct fibers [63]. Hence, a closing operation can geometrically replicate this behavior on the images of the skeleton. Mathematically, as exemplified by Didari et al. [99], the dilation is a Minkowski sum between the skeleton and the SE while the erosion is a Minkowski subtraction between the result of the dilation and the SE. The results of the closing operation applied to a single slice of the 2D stack are shown in Figure 3.7 for increasing circular SE. Other shapes are also possible for the SE (e.g. square, diamond and so on) but the circular one

resulted to give the best approximation for the binder wetting behavior (a detailed discussion on the effect of the shape of the SE can be found elsewhere [99]).

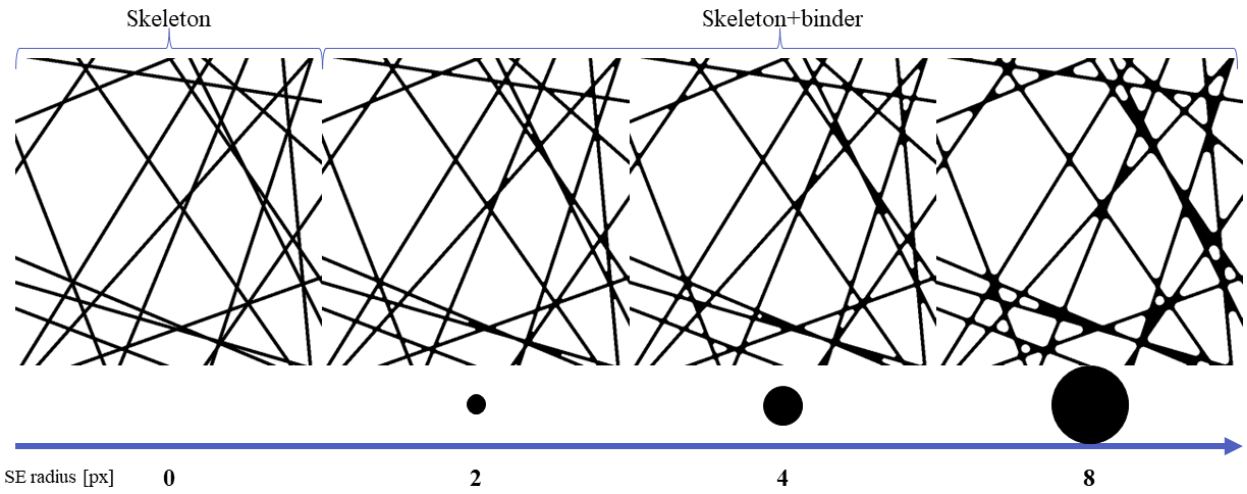

Figure 3.7 Closing operation applied to a single slice of the 2D stack. The binder is added at the intersections between fibers, mimicking the wetting properties of the actual resin. The effect of increasing the radius of the circular SE is visualized in the increased amount of binder added.

Once binder is added, a subsequent assessment is conducted to verify the final porosity of the sample, aiming to match it with the porosity of the commercially available sample. It needs to be pointed out here, that the actual GDL geometry has a further coating of PTFE to account for the hydrophobicity of the GDL. However, the PTFE coating effect can be indirectly accounted for in the CFD simulations, by considering a varying surface tension parameter (such as the liquid contact angle), rather than further geometrically modifying the geometry. If the calculated porosity after binder addition aligns with the target value, the generation process is considered complete, and the 3D image stack is converted into an stl file. In any other case the algorithm automatically restarts from performing the closing operation, with a different size of the SE. Please notice that for a 3D stack since binder may get added also between two subsequent fiber layers, the closing operation has to be performed with a 3D SE, so that the disk becomes a sphere (Figure 3.8). In this sense, when choosing to perform the binder addition with a 3D SE rather than a 2D one, if the radius of the SE is kept constant, more binder will be added in the 3D case as also the adjacency between fibers belonging to different fiber layers will be accounted for.

For concluding this section on the geometry generation, an important aspect has to be highlighted.

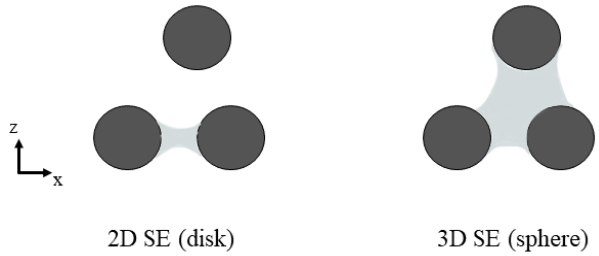

Figure 3.8 Qualitative binder addition in 2D and in 3D, with disk and sphere as SE, respectively. When using a 3D SE, the binder gets added also in the z (or TP) direction.

In particular, the specified porosity of the commercial GDL samples is the porosity of the structure composed by the skeleton and the binder. This means that for the generation of the skeleton, the so called skeleton porosity is an information not clearly specified in spec sheets and needs to be back-calculated. In order to obtain the porosity of the skeleton starting from the porosity of the commercial sample, an additional parameter is introduced, defined as the binder volume fraction (BVF). From simple considerations, it can be shown that the BVF can be calculated from the knowledge of the overall porosity and the skeleton porosity, as suggested in Equation 3.3:

$$BVF\left[\frac{m_{binder}^3}{m_{solid}^3}\right]=\frac{\varepsilon_{skeleton}-\varepsilon}{1-\varepsilon} \tag{3.3}$$

from which the skeleton porosity can easily be calculated:

$$\varepsilon_{skeleton}=BVF\left(1-\varepsilon\right)+\varepsilon \tag{3.4}$$

The reported values of BVF in the literature lack consistency. They vary widely, ranging from 0.1 to 0.5, resulting in significant variations in the geometry's morphology and, consequently, in its transport properties (e.g. values from 5 to 15 % weight are reported here [45], whilst 40 % and 50 % volume are reported here [69] and here [100] respectively).

3.2. Validation methodology of the geometry

The validation process involves verifying whether the generated geometry aligns with the desired physical characteristics of the actual samples. By conducting a thorough validation, the suitability and reliability of the generated geometry can be established.

The following validation has been carried out:

1. Morphology validation
    - Visual comparison (qualitative)
    - Sectional porosity analysis
    - Pore size distribution analysis
2. Transport properties validation
    - Effective conductivity determination
    - Effective diffusivity determination

The initial validation process involves examining the structural characteristics of the virtual sample and performing a visual comparison with scanned images of physical GDLs samples retrieved from the literature. Additionally, an analysis of sectional porosity and pore size distribution is performed. The significance of studying the morphology derived from the virtual reconstruction lies in the inherent connection between the transport phenomena within the GDL and the morphology itself. As an example, even if not investigated in the current study, the pore size distribution is known to dominate, together with wettability, the intrinsic saturation/capillary-pressure relationship which is critical for optimal multiphase performance [35].

3.2.1. Morphology validation

The comparison of the morphology starts with a qualitative assessment based on different images of the obtained virtual sample and the carbon paper geometry. In fact, even though quantitative metrics are necessary at this stage, it is also important to critically analyze the replicated geometry to see whether it visually resembles the real scans obtained via advanced imaging techniques.

Once this phase is completed, the sectional porosity plots can be compared. Obtaining these plots is a straightforward process as the porosity can be computed for

each slice of the 2D image stack generated during the binder addition. In fact, computing the porosity for one single slice requires its binarization first, followed by computing the ratio among the white (void) pixels and the total number of pixels of the slice (white plus black pixels representing the solid phase). By repeating this procedure for each slice of the full stack, porosity profiles along the specific direction of interest (the z direction, shown also in Figure 3.3) can then be compared with experimental data (mainly obtained via analysis of μCT reconstructions).

Finally, the extraction of the pore size distribution (PSD) from the sample is required. Upon conducting a comprehensive analysis of the numerical methods utilized for this purpose, it becomes evident that the geometrical definition of what constitutes a pore and the PSD plays a crucial role in determining the actual probability density curve of the pores within the GDL geometry. The main contribution to this important rationalization comes from Münch & Holzer, whose seminal work reports the development of a computationally fast approach for extracting the PSD from 3D data, using different geometrical definitions of the pore size distribution [101]. The motivation behind the work was to explain the discrepancy between experimentally obtained PSD via mercury intrusion porosimetry (MIP) and PSD obtained from analysis of back-scattered electron (BSE) images. With this purposes, they developed a computational framework to reproduce the results of both the approaches and to explain the fundamental differences between the two methods. In the current study, the pore size distribution (PSD) analysis is conducted using the Fiji ImageJ plugin called "Xlib", based on the framework developed by Münch & Holzer [102].

Three methods are available in the framework:

1. Discrete PSD;
2. Continuous PSD;
3. Continuous PSD with MIP simulation.

Here, a descriptive overview of how each method functions is presented. As a reference case-study, a slice from a 2D stack is chosen, although the principles outlined can be applied to 3D geometries as well.

In the discrete PSD approach, the pores are regarded as discrete object, meaning that each pore has its own area, delimited by the boundaries of the solid phase. Once each pore has been identified, its equivalent diameter can be calculated, as shown in Figure 3.9.

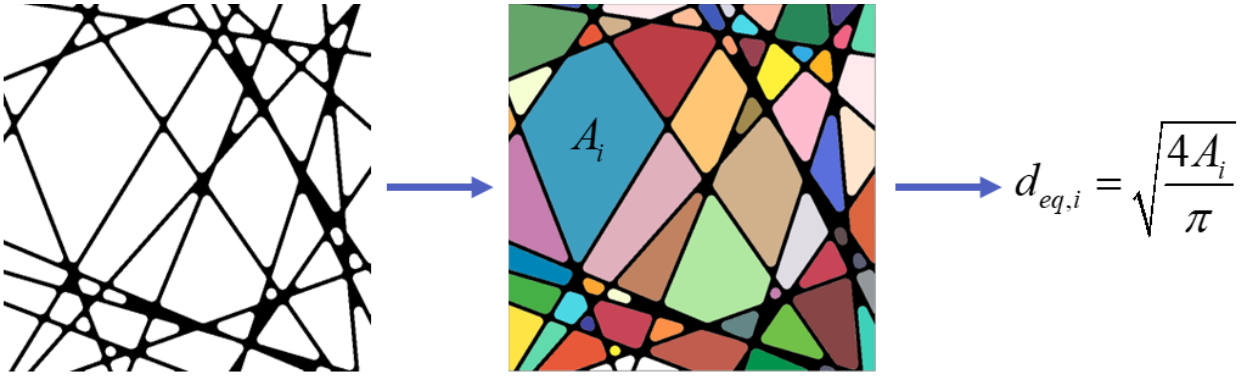

Figure 3.9 PSD according to the discrete approach. Each single pore is assigned an equivalent diameter calculated using the area of the pore itself.

Of course in three-dimensions the diameters will be calculated from equivalent spheres representing three-dimensional cavities. This is the usual approach by which pore size distribution is obtained by analysis of BSE images.

In the continuous PSD approach, the pore space is filled with spheres of gradually decreasing diameters. This means the pores that in the discrete approach were considered as separated entities now can be filled with balls of varying sizes. In Figure 3.10 a visualization of the process is reported, where it is possible to see how the procedure starts by trying to fit disks of a sufficiently big diameter d_1 throughout the pore space. When there are no more volumes in the pore space that can accommodate a disk of diameter d_1, the size of the disks being fitted is reduced to d_2 and the pore space is once again scanned to fit these new disks. This procedure of fitting disks and reducing their diameter is repeated until a sufficiently small diameter is reached, in correspondence of which the totality of the pore space has been filled.

In the last method, the continuous PSD with MIP simulation is virtually identical to the continuous method, the only difference being that, as in a real MIP experiment, the balls of different diameters are intruded into the pore volume from one of the edges of the 2D image (or from one of the faces of the 3D geometry). For this method, since the connectivity of the GDL 2D slice does not allow for a proper visual representation, at first a visual of the process is shown in Figure 3.11 with a generic porous media and then in Figure 3.21 the result of the procedure directly applied to a 3D GDL virtual sample is showcased.

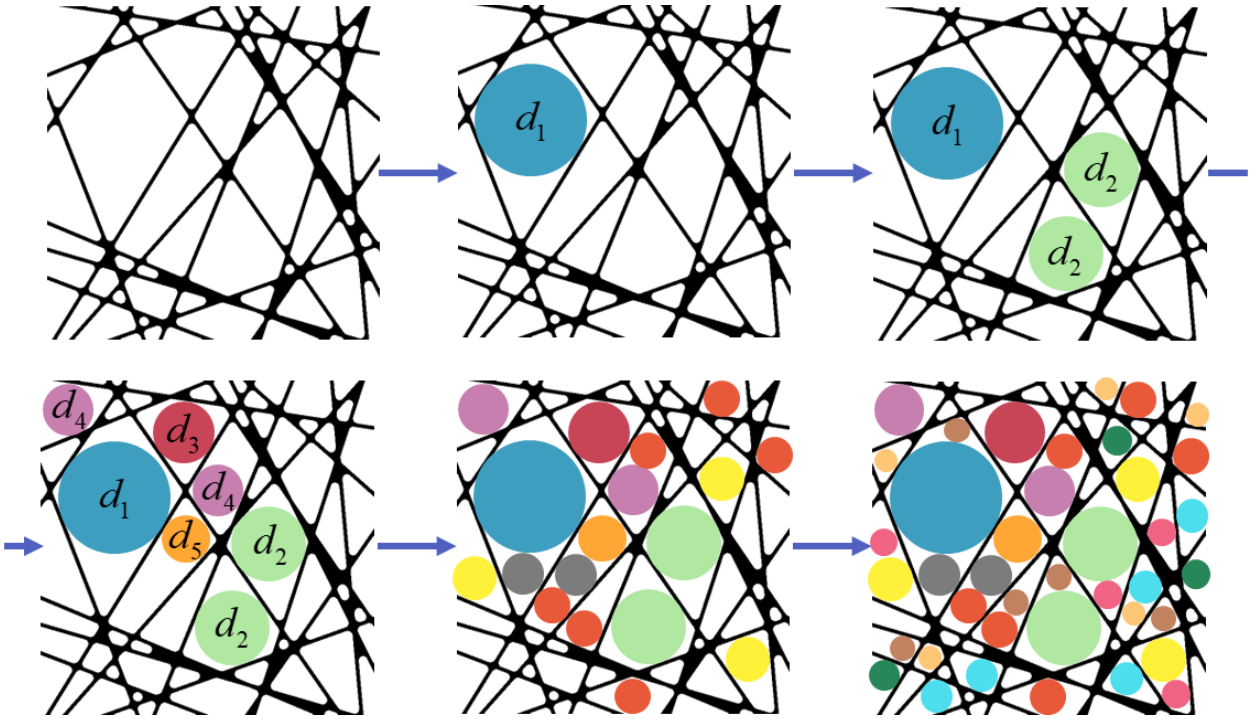

Figure 3.10 PSD according to the continuous approach. From the upper left side to the lower right side the 2D (3D) pore space is gradually filled with disks (spheres) of decreasing size.

This method appears to be particularly appealing for computing the PSD, as even if not physically based it still retains some important phenomena of the physics-based MIP experiment. Experimentally, the MIP technique takes advantage of the high surface tension of the mercury. In order to measure the PSD in fact, it is required that the liquid utilized for the intrusion is a non-wetting fluid (i.e. it has a high surface tension with respect to the solid porous media). The reason is straightforward and can be explained by making use of the Washburn equation (Equation 3.5).

$$D_{pore} = 4\gamma \cos\theta / P \qquad 3.5$$

Derived for pores of cylindrical shape, the equation relates the diameters of the pores intruded with liquid to the pressure applied in the mercury bath in which the sample is immersed and to the nature of the liquid solid interface (ϑ being the contact angle and γ the surface tension [mN/cm]).

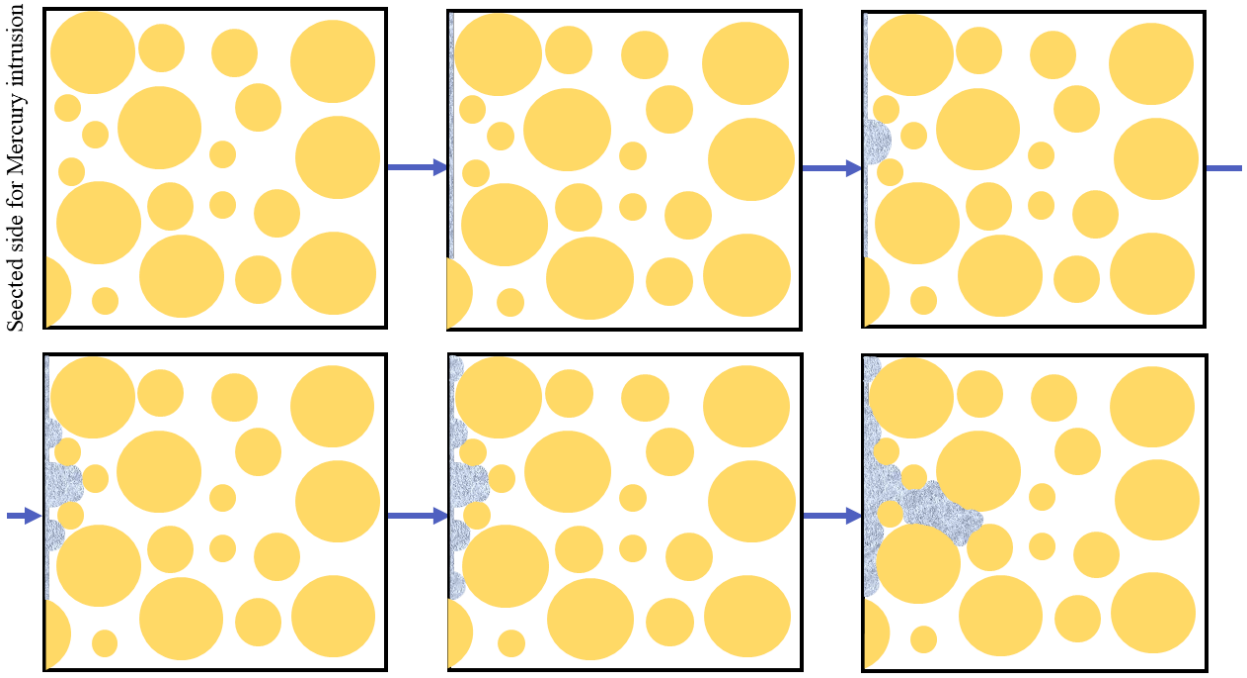

Figure 3.11 MIP approach for a generic porous media. The left side of the 2D geometry has been selected for the intrusion. From there the algorithm will start to fit disks of decreasing diameter, until all the void space gets filled. Each snapshot corresponds to a disk of a fixed diameter being fitted.

It is clear that if the surface tension is low, all the pores, starting from the bigger up until the smaller ones will be filled with the liquid without having the possibility of controlling with the pressure P the extent of the liquid penetration. Contrarily, if γ is sufficiently high it is possible to gradually increase the pressure applied to the mercury bath and monitoring the incremental volume of mercury intruded for each increase in applied pressure [103]. At that point by using Equation 3.5 applied pressures are related to pore diameters and the cumulative PSD can be plotted. As anticipated, the simulated MIP does not require the solution of any physical equation as it only makes use of image processing operations. Still, as it happens for the real MIP, during the process gradually smaller pores are filled with mercury. As a consequence, some important phenomena occurring in real MIP tests are also captured by the simulated MIP (e.g. the ink bottle effect for which larger pores, which can only be reached through smaller pores known as "necks", become filled when the pressure corresponding to the smaller pores is reached [104]).

Regardless of the chosen geometric definition of pores, the outcome of the analysis is an array of pore diameters ranging from 10^0 to 10^2 μm.

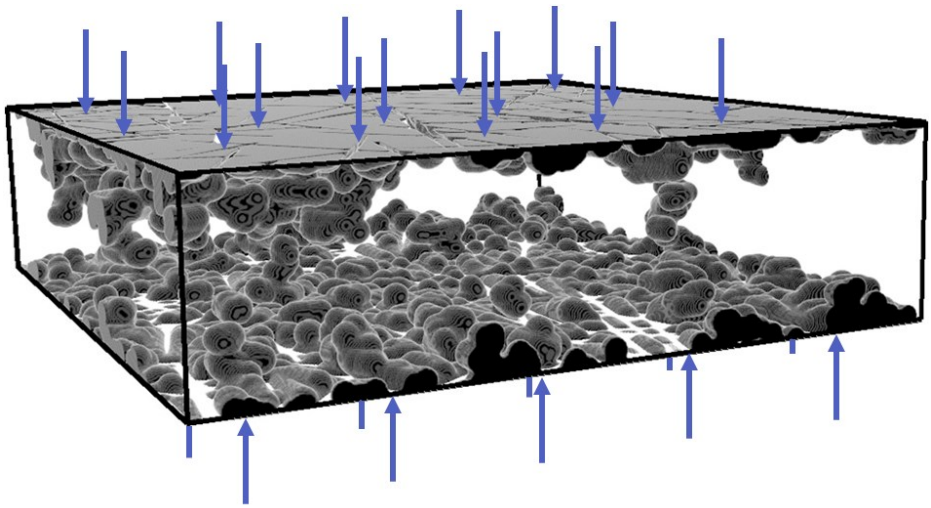

Figure 3.12 PSD according to the continuous MIP approach. In this case both the top and bottom faces were selected for Mercury injection. Adapted from *[69]*.

To construct the PSD, it is advantageous to begin with the cumulative PSD, as the provided array requires no additional data processing to generate the curve. For instance when considering the continuous approach, the algorithm will provide the diameters of the fitted disks in descending order and the corresponding volume of the pore space occupied. This means that it is possible to report on a plot the progressive filling of the pore space volume as a function of the diameters of the disks being fitted. The latter plot is formally a cumulative PSD, whose normalized version is reported in Figure 3.13 with reference to the pore space in Figure 3.10. To normalize the cumulative PSD curve, it is simply a matter of dividing all the volumes obtained by the total volume of the pore space. This normalization is useful because it allows the y-axis to represent the volume fraction of the filling pore space, rather than the total volume of the pore space.

Starting from the normalized curve, it is possible to apply the definition of probability density function to calculate the actual PSD, as shown in Equation 3.6.

Among the three possible choices, the specific method employed in the current work for measuring the PSD is the MIP based. MIP has been commonly used by experimentalists to determine the distribution of pore sizes in GDL ([61], [64], [69], [45]). By utilizing the MIP method, the aim is to ensure consistency and enable a meaningful comparison between numerical results and experimental data. Furthermore, all the described methods were tested, and it was found that the MIP simulations yielded the most comparable results to those reported in the literature.

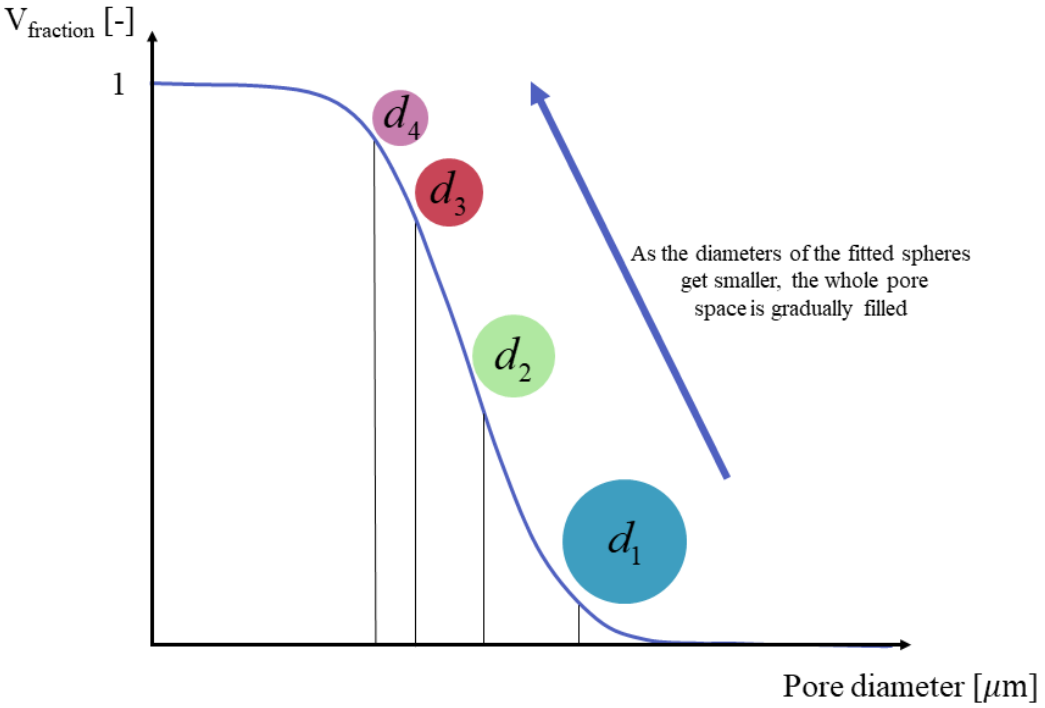

Figure 3.13 Normalized cumulative PSD. The curve is obtained by dividing the cumulative PSD by the total volume of the pore space.

$$PSD\left[\mu m^{-1}\right] = \frac{dV_{fraction}}{dD_{pore}} \qquad 3.6$$

3.2.2. Transport properties validation

The Laplace equation for the temperature and concentration scalar fields is solved in OpenFOAM, an open source CFD software package based on the finite volume method (FVM). Since the geometry is highly anisotropic the analysis has to be performed separately for at least two directions, the through-plane direction (TP) and the in-plane direction (IP). To provide a clearer understanding, in relation to Figure 3.14, the TP direction refers to the normal direction of the x-y plane, while the IP directions are the normal directions of the z-y or z-x planes. Ideally, the two IP directions should be treated independently. However, in practice, due to the numerical model used for the reconstructed geometry where fibers are positioned in the x-y plane with a uniformly

distributed orientation ϑ, it can be assumed that the properties are isotropic for the IP directions.

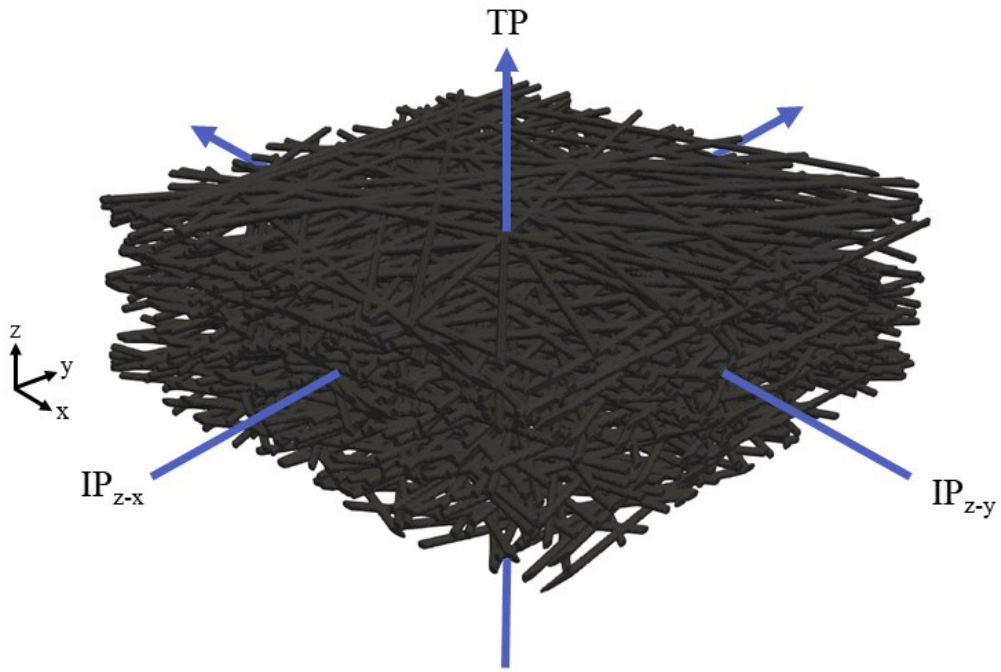

Figure 3.14 TP and IP directions visualized.

In order to accurately describe the transport phenomena in the reconstructed GDLs, an appropriate meshing procedure is required. In this study, the computational domain for the solid phase is generated using the snappyHexMesh utility of the OpenFOAM framework [105]. The procedure begins with an uniform background mesh (generated with the blockMesh utility) and then refines the computational domain near the stl surface using the cut-cell approach. Finally, the mesh surface is "snapped" on the stl file, to ensure precise reproduction of the foam geometries (a detailed explanation of the procedure, together with visual representation of it can be found elsewhere [106]). Prior to solving the equations and interpreting the results in terms of the calculated effective transport properties, it is necessary to conduct a mesh independence study to identify a suitable resolution for the computational grid that ensures the accuracy of the computations. After experimenting with various background meshes, a specific mesh was chosen that ensures a ratio of 4 between the fiber diameter and the grid size of the background mesh. In doing so, after the castellation and the snapping operations a mesh of approximately 17M cells was resulting for the solid phase (Figure 3.15).

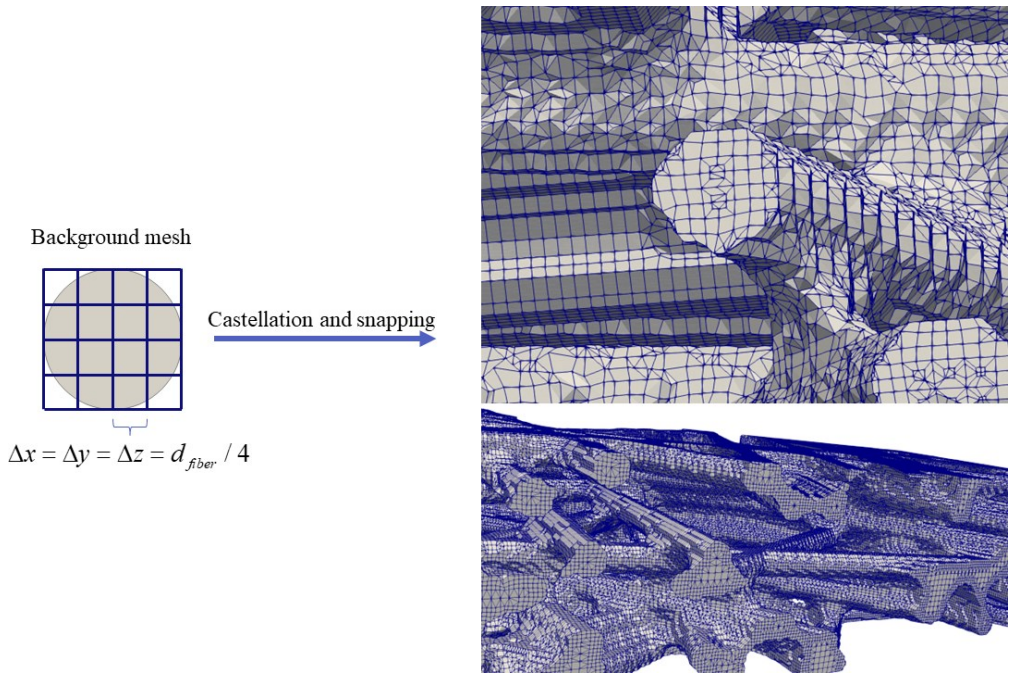

Figure 3.15 The mesh grid before and after the castellation and snapping operations.

The selection of simulations for conducting this phase of the study prioritized heat conduction over species diffusion because the former imposes stricter demands in terms of grid refinement. Of course the independence was proved both for the TP and IP simulations. Moreover, care is taken to generate high-quality grids with low non-orthogonality (say low number of faces belonging to two different cells which are not oriented with angles of 90 degrees) and skewness values (which measures the deviation of an element from its ideal shape). All the relevant parameters for the mesh construction are summarized in Table 4.

Table 4 Mesh parameters and settings for castellation and snapping in OpenFoam.

Δx=Δy=Δz	**Level of refinement (features & surfaces)**	**Max nonorthogonality**	**Max boundary skewness**	**Max internal skewness**
$d_{fiber}/4$	1	50	4	2

The simulations should be carried out on the representative elementary volume (REV). An exhaustive definition of REV is provided by Willis et al. referring to a composite material for structural applications: "It is the smallest material volume element of the composite for which the usual spatially constant (overall modulus) macroscopic constitutive representation is a sufficiently accurate model to represent mean constitutive response" [107]. Simply stated for the purposes of the current study, the REV is the smallest volume of the porous media (GDL) for which the approximation of effective porous media is valid (and for which it is possible to univocally determine the effective transport properties). In principle conducting a REV analysis is simple, at least conceptually. Essentially, the process (Figure 3.16) involves progressively cropping and examining larger subdomains from a generated virtual geometry to understand the dependency of the analyzed properties on the dimensions being considered. The selection of the REV depends on the specific property under analysis. As an example, it is possible to use the porosity to define the REV. In this case it can be defined as a geometrical REV (representative of morphological properties).

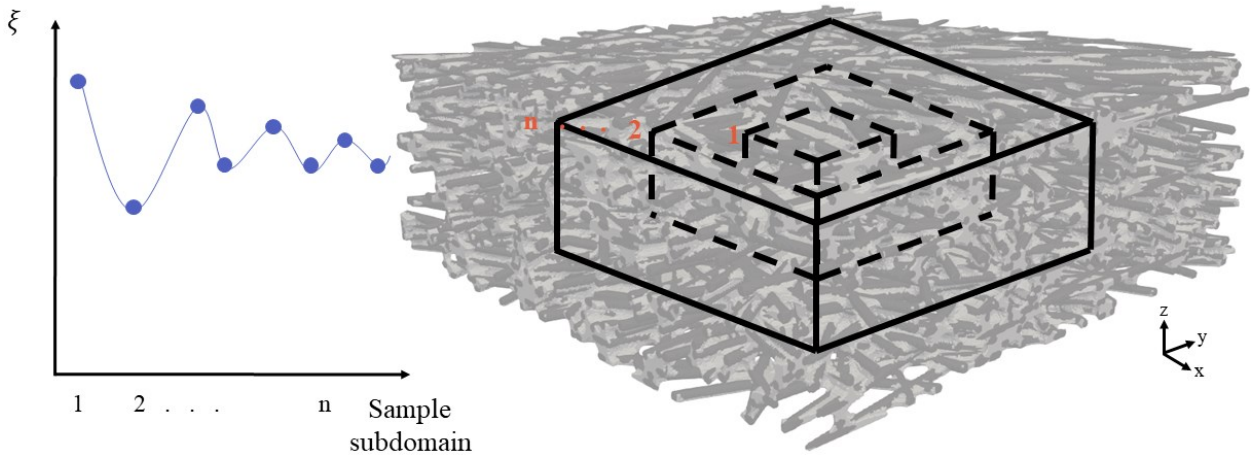

Figure 3.16 Graphical rationale of the REV analysis. Subsequently bigger domain are analyzed in terms of the generic property ξ until convergence (or reduced oscillation around a mean value) is reached.

At the same time effective transport properties may be used to define a physical REV (representative of physical properties as the effective conductivity or effective diffusivity). The resulting REV from the two definition may or may not coincide, as happened for example with open-cell foams here [108], where switching from a geometrical (porosity-based) to a physical REV (effective conductivity-based) required

4.5 more cells in each direction (in the work it is also highlighted how this behavior may be due to the strong dependence of the effective conductivity on the local structure of the foam). It is important to note in this sense, that when using macroscopic approaches to transfer information to higher scales in porous media, the REV must be valid for all properties being investigated.

The analysis is ideally concluded when no further changes in the analyzed property are observed upon increasing the dimension of the subsample. However, one finding from the initial studies on REV was that the criterion of observing zero fluctuation in the effective property as the measurement volume increases was unrealistic [109]. As a result, Bachmat & Bear [110] proposed the idea of allowing for fluctuations in the effective property as long as they remained below a predetermined threshold value, thereby ensuring approximate validity of the REV assumption (in this case the REV is also referred to as "statistical REV" [111]). In the analysis of the current work, the procedure depicted in Figure 3.16 is repeated different times varying the location of the subdomain within the geometry, and the results are visualized with candlestick charts (Figure 4.15) to account for the stochasticity of the reconstruction. The REV was defined then as the volume of the domain where the observed changes in the measured property were within the allowable tolerance value (see results section). One final consideration is necessary regarding the REV analysis. Due to the limited thickness of many commercial Gas Diffusion Layers (GDLs), typically around 200 μm, the analysis was performed by maintaining a fixed thickness of this value and only altering the dimensions of the geometry in the x-y plane.

As discussed in the theoretical section, equation 2.30 allows for the calculation of the effective transport properties when their bulk value and the flux of the scalar fields being transported (species concentration, temperature, electric potential) are known.

The solver laplacianFoam of OpenFOAM was used. The default solver is capable of solving unsteady diffusion problems. However, since we only required the steady state solution for our case, we made appropriate modifications to the solver. In practice, a gradient of the selected scalar field ϕ (e.g. temperature) is applied across two opposing geometry faces that are perpendicular to the specified flow direction (Dirichlet boundary condition) while on the remaining lateral walls the condition of zero flux is set (Neumann boundary condition). A second order discretization scheme is employed for the Laplacian operator and the simulations were assumed to be converged when the calculated residual is below 10^{-12} (see Appendix A for the info on the residual definition). The effective thermal conductivity is then evaluated according to Equation. 3.7 (obtained directly from Equation 2.30).

$$k_{eff} = \frac{L\int_{A^*} \boldsymbol{J} \cdot d\boldsymbol{A}^*}{A\left(\phi_1 - \phi_2\right)} \qquad 3.7$$

A and L being the total cross section perpendicular to the flux and the side length of the GDL, respectively. In the present case study, due to the fact that the thermal conductivity of the carbon based material is at least 3 orders of magnitude higher than the thermal conductivity of air [112], heat transfer in the latter medium has been neglected, thus reducing the problem to a single phase conduction case study (likewise when considering species diffusion through the void medium, the species transport across the solid phase has been neglected). Finally, it is important to make an additional observation, specifically regarding the conduction simulations. As discussed extensively in the introductory chapter, the Gas Diffusion Layer consists of at least two solid phases: the graphitized PAN fiber and the carbonized binder. Consequently, despite both materials being carbon-based, they exhibit different bulk thermal conductivities (as a direct result of the manufacturing process and of the different nature of the two materials). In this study, similar to what is commonly found in the literature, the solid phase of the GDL was treated as a single solid phase without distinguishing between the fiber and binder components. The possible effects of this choice will be discussed in the results section.

3.3. Correlations for the effective transport properties

After completing the morphological and transport property validation of the geometry, the computational framework, which includes the virtual geometry generation followed by transport simulations, can be employed to establish reliable macroscopic effective transport property correlations for the gas diffusion medium.

When initiating the development of any correlation, it is necessary to establish the functional relationship between the effective transport properties and the selected parameters, in this case structural parameters. The correlations will be written to find the ratio between the effective transport property (k_{eff}) and its bulk value (k). For instance, it can be supposed that the effective transport property ratio may be dependent on the geometrical microparameters used during the construction phase, namely the number of fibers per layer (n), the fiber diameter (d), the binder volume fraction (BVF) and the porosity (ε) as shown in Equation 3.8.

$$k_{eff} / k = f\left(n, d, BVF, \varepsilon\right) \tag{3.8}$$

It should be noted that of the 4 parameters, only 3 of them are independent. In fact, as soon as n, d and BVF are fixed, the porosity of the sample is completely determined. As an example, employing a number of fibers of 18, a fiber diameter of 8 um and a BVF of 40% automatically determines a porosity of 0.742.

A power law is assumed to describe the functional form.

$$k_{eff} / k = f\left(n, d, BVF, \varepsilon\right) = g\left(n\right) h\left(d\right) i\left(BVF\right) j\left(\varepsilon\right) = c \cdot n^{\lambda_1} d^{\lambda_2} BVF^{\lambda_3} \varepsilon^{\lambda_4}$$

and one functional dependence is removed e.g. the one on the number of fiber (due to the interdependencies discussed above):

$$k_{eff} / k = c \cdot d^{\lambda_2} BVF^{\lambda_3} \varepsilon^{\lambda_4} \tag{3.9}$$

By individually varying each of the three parameters while holding the other two constant, it is possible to observe the corresponding changes in the investigated effective transport property, k_{eff}/k. If when changing the three parameters (d, BVF and ε) the same effect is observed on the effective transport property, then a porosity-based monofunctional relationship can be established (as shown Figure 3.17), indicating that ε provides an exhaustive description of the transport in GDLs.

To obtain the correlations the distance between the simulation points and the fitted curve has to be minimized. The optimization process is facilitated by the SciPy library of Python. The specific function utilized for this purpose is "curvefit" from the optimize module. This function utilizes non-linear least square regression to determine the parameters of the fitted functions.

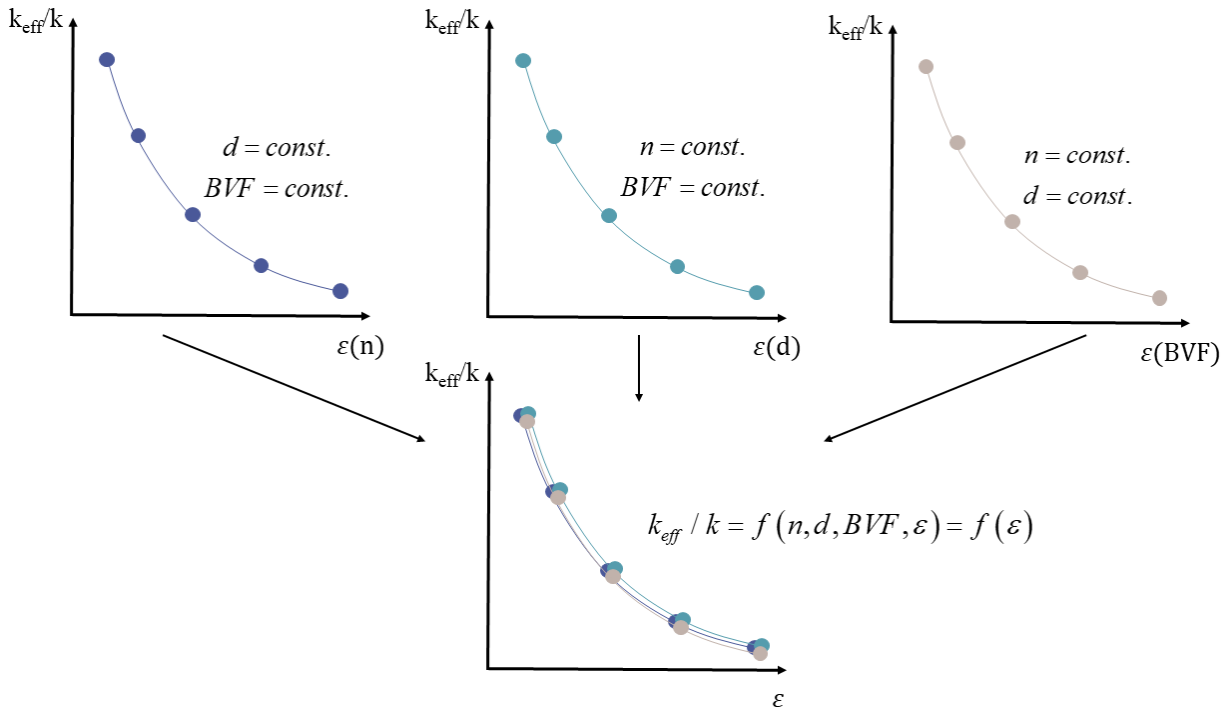

Figure 3.17 Graphical rationale of the procedure for determining the monofunctional porosity-based correlation for the effective transport properties.

3.4. Macroscopic model of GDE for CO_2 electroreduction to CO

The CO_2 electroreduction to carbon monoxide inside a gas diffusion electrode is described by the means of a macroscopic model of the cathodic chamber. As shown in Figure 3.18, the computational domain is composed by the gas diffusion layer (of thickness L = 325 μm), where a one-dimensional spatial discretization in the TP direction is employed and by the catalyst layer, say the microporous layer with catalyst particles sprayed upon it, descripted as a reactive surface in direct contact with the GDL. The gas diffusion layer is completely dry while the catalyst layer is partially wetted. The physical phenomena the model accounts for are listed below:

1. Multicomponent gas diffusion in the gas diffusion layer.
2. Dissolution of the CO_2 in the liquid electrolyte;

3. Carbonate species reactions and water auto-protolysis reactions inside the liquid electrolyte wetting the catalyst layer (homogeneous reactions);
4. Charge transfer reactions in the catalyst layer (surface reactions);
5. Escape of dissolved CO_2 and aqueous species from the cell, by its diffusion within the electrolyte channel.

The CO_2-rich stream is fed from the gas channel, through a stream whose only impurity is nitrogen. As the CO_2 diffuses through the GDL it reaches the catalyst layer where it is first dissolved into the electrolyte.

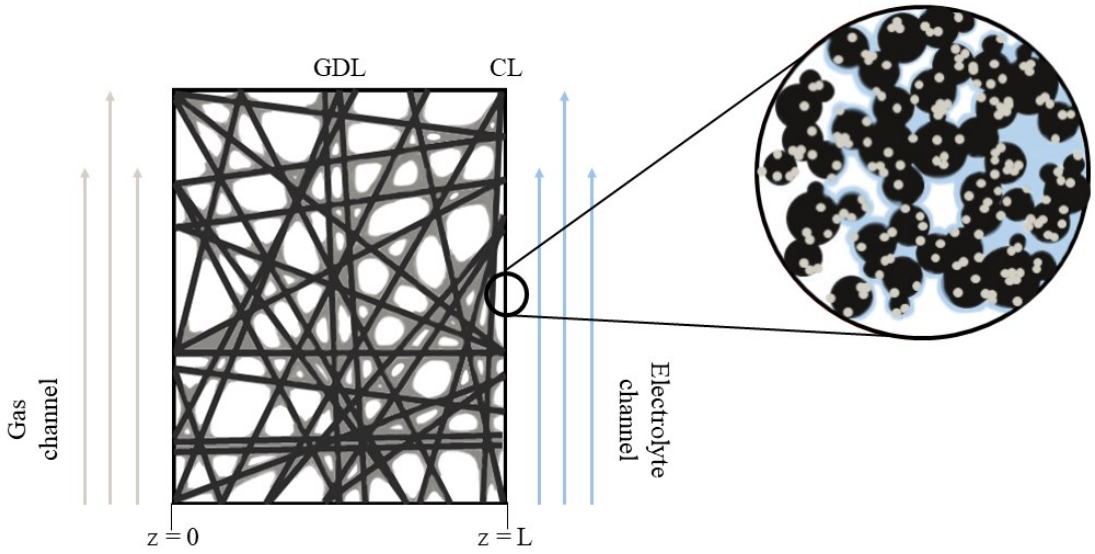

Figure 3.18 Computational domain. The gas diffusion layer is discretized in the TP direction. The effective medium approximation is used to treat the GDL as a homogeneous media characterized by effective transport properties. The catalyst layer is treated as a reactive surface at z = L. In the magnification, the carbon black microporous layer with nanoparticles of silver upon it, covered by the electrolyte thin layer.

After the dissolution the gas has to diffuse inside the liquid to reach the active sites where the charge transfer reaction will occur. The charge transfer reaction considered are not only the reduction of CO_2 to CO (Equation 2.14) but also the HER in alkaline and acidic media (Equation 1.8 and Equation 2.11, respectively), which are considered as unwanted reactions subtracting a portion of the overall current circulating through the cell.

The gas evolving from the charge transfer reactions (CO and H_2) are allowed to leave the cell only from the GDL side, without bubbling in the electrolyte solution.

Parallelly to the diffusion, CO_2 also reacts homogeneously according to the scheme of carbonate species equilibrium reactions reported below.

$$CO_2 + H_2O \rightleftharpoons HCO_3^- + H^+ \qquad CO_2 + OH^- \rightleftharpoons HCO_3^-$$
$$HCO_3^- \rightleftharpoons CO_3^{2-} + H^+ \qquad HCO_3^- + OH^- \rightleftharpoons CO_3^{2-} + H_2O$$

The water auto-protolysis (or self-ionization) also occurs:

$$H_2O \rightleftharpoons H^+ + OH^-$$

At last, the dissolved CO2 can also potentially exit the catalyst layer on its right-hand side through the electrolyte flowing in the electrolyte channel.

As anticipated in the theoretical section (chapter 2.3), the described system can be treated as a diffusion + reaction occurring in series. Differently from the previous toy problem, here the diffusive molar fluxes (N) are described by the Stefan-Maxwell equation (suitable for multicomponent diffusion):

$$-\frac{P}{RT}\frac{dy_i}{dz} = \sum_{j=1}^{n} \frac{y_j N_i - y_i N_j}{D_{i,j}^{eff}} \qquad 3.10$$

where the effective diffusivities are calculated using the developed correlations (Figure 4.21). Knudsen diffusion is not accounted for as due to the mean pore size found in GDL (d_{av} = 20 μm), the Knudsen diffusivity results to be order of magnitudes higher with respect to the effective diffusivity of the gas. As an example, the Knudsen diffusivity at 298 K is calculated for CO_2 (Equation 3.11 [38]), which results to be at least 3 order of magnitudes higher than the effective diffusivity of CO_2 in air. Therefore, Knudsen diffusion is not controlling the diffusive transport in the GDL.

In order to describe the diffusion problem, a shell material balance formally identical to the one developed for the toy problem (Equation 2.24) can be written for any

$$D_{K,CO_2} = \frac{d_{av}}{3}\sqrt{\frac{8RT}{\pi M_{CO_2}}} = 2.5\cdot 10^{-3}\,\frac{m}{s^2} \qquad 3.11$$

of the gaseous species diffusing in the GDL (CO_2,CO,H_2,N_2). The absence of any source/sink term and the steady state form of the problem, brings the molar flux to be constant:

$$N_i = const. \quad i = 1,2,...,n \qquad 3.12$$

to be used in combination with equation 3.10. The system of ordinary differential equations has to be solved to find the unknowns 2n integration constants.

Being a boundary value problem, two boundary conditions have to be enforced. At the left-hand side of the gas diffusion layer, Dirichlet boundary conditions corresponding to the inlet concentration of the CO_2-rich gas flow are used:

$$y_i\left(z=0\right) = y_i^0$$

while for z = L, the 1D model has to be linked with the surface description of the catalyst layer. As anticipated, in the catalyst layer charge transfer reactions occur, which can be described by the means of the Tafel kinetics (assuming the overpotential is high enough to make the reactions irreversible and proceeding towards the reduction direction):

$$R_{k,CT} = \frac{j_k}{\nu_k F} = \frac{j_{0,k}}{\nu_k F}\left(\frac{C_{ox,k}^{surf}}{C_{ox,k}^{bulk}}\right)\exp\left(-\frac{\beta_k \nu_k F}{RT}\eta_k\right)$$

In this expression the overpotential η_k is calculated accounting for the difference between the actual potential applied and the thermodynamic potential required (Equation 3.13).

$$\eta_k = \phi_{GDL} - \phi_{CL} - \left(E_k^o(SHE) - 0.989\, pH \right) = \phi_{GDL} - \left(E_k^o(SHE) - 2.303 \frac{RT}{F} pH \right) \qquad 3.13$$

The bulk reaction terms instead are modeled with the standard power law rate expression of homogeneous reactions, comprising of the thermodynamic consistency that links the forward to the backward reaction rates through the equilibrium constant:

$$R_{j,hom} = k_j^f \left(\prod C_{reactants,j} - \frac{1}{K_{eq,j}} \prod C_{products,j} \right)$$

The transfer of species from the catalyst layer to the liquid electrolyte, occurring at the right-hand side of the CL is modeled using the Sherwood-Reynold-Schmidt [38] correlation for the mass-transfer coefficient:

$$N_i^{out} = k_{MT,i} \left(C_i^{CL} - C_i^{electrolyte} \right) = \left(\frac{D_{i/H_2O}}{L_{tot}} \right) 0.664 \left(\frac{\rho v L_{tot}}{\mu} \right)^{0.5} \left(\frac{\mu}{\rho D_{i/H_2O}} \right)^{1/3} \left(C_i^{CL} - C_i^{electrolyte} \right)$$

where the transport properties used are related to the liquid electrolyte (approximated to pure water) and L_{tot} is the total length of the electrode (0.02 m). At last, having to describe the transfer of CO_2 from the gas phase to the liquid phase, Henry's law is used in the following form:

$$N_{CO_2}^{in} = \frac{D_{CO_2/H_2O}}{\delta} \left(H_{CO_2/H_2O} \cdot P \cdot y_{CO_2}(x = L) - C_{CO_2}^{CL} \right)$$

being H the Henry's constant of CO_2 in water, P the total pressure of the gas in the GDL (assumed to be 1 atm) and δ the thickness of the electrolyte layer covering the catalytic particles.

Now that all the relevant terms have been defined, to determine the remaining

boundary conditions, a material balance on the catalyst layer is carried out, giving Equation 3.14.

$$N_i^{in} \cdot a_v^0 s - N_i^{out} \cdot \frac{\varepsilon_{CL}}{L_{CL}} + \sum_j \nu_{ij} R_{j,\text{hom}} \cdot \varepsilon_{CL} s + \sum_k \nu_{ik} R_{k,CT} \cdot a_v^0 s = 0 \qquad 3.14$$

where the saturation of the catalyst layer "s" has been introduced (the ratio between the liquid volume and the total void volume inside the CL) together with the specific surface area of the catalyst "a_v^0" ($m^2_{catalyst}/m^3_{CL}$) and the geometrical length of the CL "L_{CL}".

Equation 3.14, constitutes an additional constraint to be satisfied by the solution of the diffusion problem. Particularly, the sought-after link among the GDL and the CL, comes by expressing the fluxes of the gaseous species as seen in Equation 3.14. Correspondently, for CO_2 the boundary condition is:

$$N_{CO_2}\left(x=L\right) = \frac{D_{CO_2/H_2O}}{\delta}\left(H_{CO_2/H_2O} \cdot P \cdot y_{CO_2}\left(x=L\right) - C_{CO_2}^{CL}\right) \cdot a_v^0 s L_{CL}$$

while for the products (CO and H_2) the flux corresponds to the charge transfer source terms. This assumption corresponds to the fact that the product species are directly added as a source term to the gas phase at the GDL/CL interface and back-diffuse in the GDL.

To solve the set of equations governing the electroreduction process, a system ordinary differential equations need to be solved for the diffusion in the GDL, while the flux boundary condition at the GDL/CL interface requires solving a set of non linear equations (Equation 3.14). The macroscopic model has been implemented in Python and solved using the SciPy solver package, a Python library commonly employed for scientific and technical computing [113].

In the context of this work, the analysis of the model will be limited exclusively to assess the effect of switching from the Bruggeman correlation to the developed correlation for the effective diffusivity, showing the discrepancy in the predicted CO partial current density.

4 Results and discussion

4.1. Geometry validation: morphology

The complete geometry generation pipeline results in a three-dimensional GDL structure as the one shown in Figure 4.1. The geometry is constituted by two solid phases, the PAN fibers (in black) and the binder (gray colored). Moreover, Figure 4.2 shows additional snapshots of the reconstructed GDG with and without binder. As the figures suggest, morphological image closing has the effect of adding binder predominantly in the fiber intersection regions, extending both between the fibers of the same layer as well as across two consecutive fiber layers. In principle the shape of the structuring element can be altered from a spherical to an ellipsoidal shape to incorporate more binder in either the TP or IP direction. In this work, the SE shape was primarily chosen based on the requirement of achieving a desired final porosity during the binder addition process. This is because by adjusting the extension of the SE in a specific direction has a distinct impact on the amount of binder added, which varies depending on the chosen direction. This criterion was applied while striving to maintain the element's spherical shape as much as possible, to minimize pronounced morphological disparities in the resulting geometries.

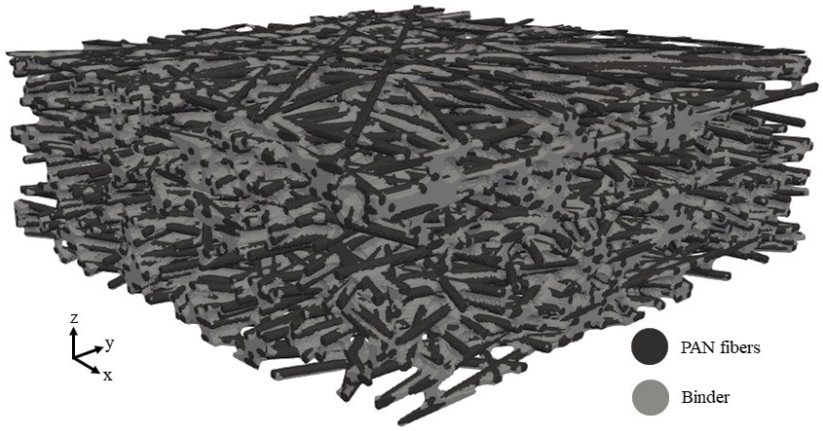

Figure 4.1 Result of the geometry generation algorithm. A three-dimensional sample of a gas diffusion layer made by carbon fibers (black colored) and binder (gray colored).

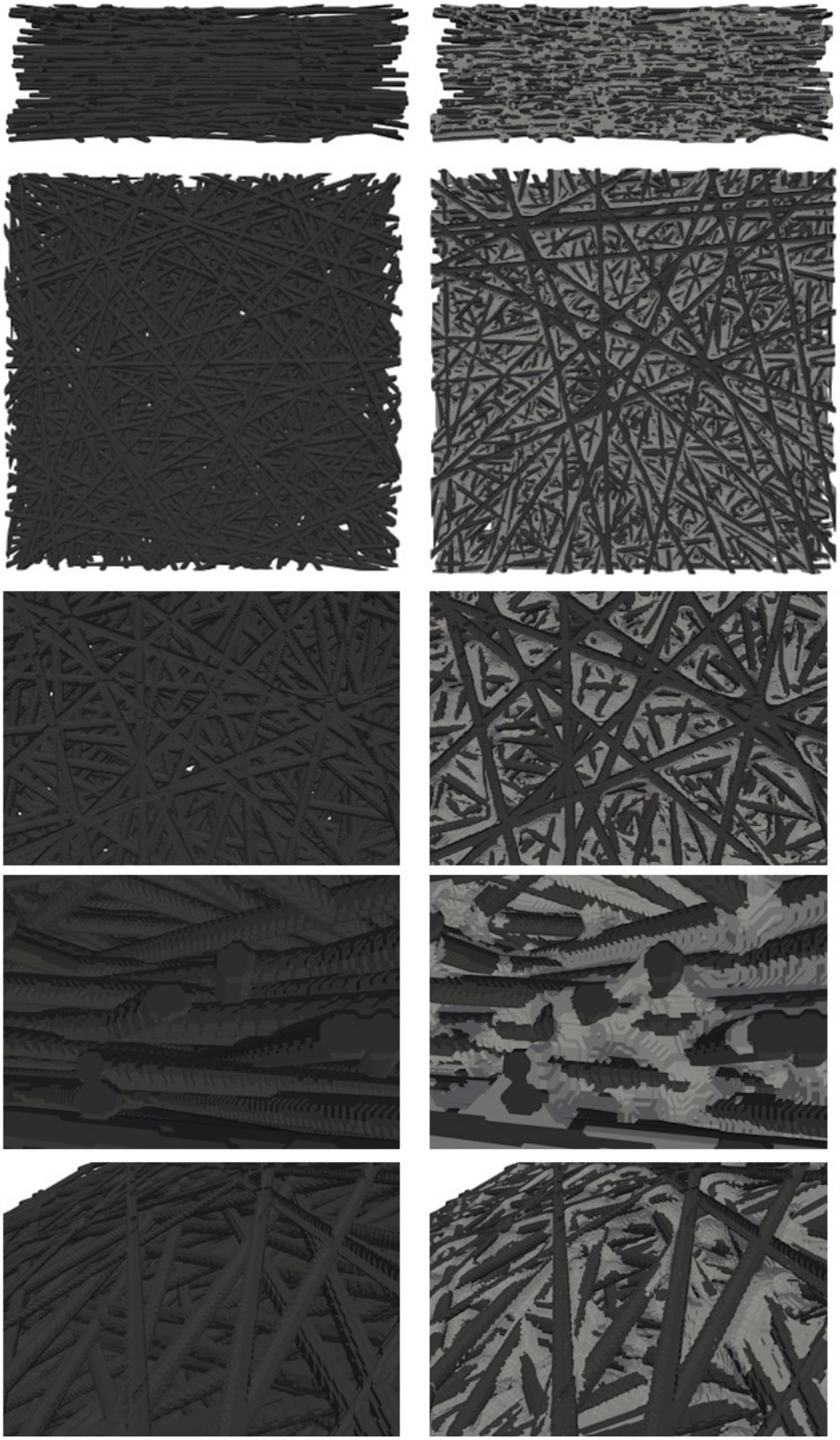

Figure 4.2 Details of binder addition in the skeleton precursor.

However, the impact of non-uniform binder addition on the geometry requires further investigation in future studies.

Figure 4.2 illustrates the significant impact of the binder addition to the skeleton structure. It is evident that the binder leads to the closure of pores, resulting in obstacles for gas diffusion or permeation within the material. However, this closure also enhances the connectivity of the structure, which in turn positively affects the thermal and electrical conductivity (if the binder is considered to have the same thermal conductivity) of the GDL.

The enhanced visualization capabilities of Fiji ImageJ open up opportunities for comparison with real images obtained through experimental imaging techniques. Figure 4.3 and Figure 4.4 show a comparison between the TP and IP scans obtained from scanning electron microscopy (SEM) and the generated sample. The TP scan reveals some differences, primarily attributed to the small curvatures observed in the real fibers, which deviate from the assumption of perfectly straight fiber used in this work. Additionally, the fibers from the physical sample also exhibit possible terminations within the domain, resulting in shorter lengths compared to the continuous fibers in the generated model. On the other hand, the IP scan highlights that the GDL exhibits a continuous distribution of fibers along the TP direction, in contrast to the discrete placement of fibers in separate layers in the model. In fact, in the model, each fiber is positioned at discrete heights, spatially separated by a distance equivalent to one fiber diameter. In future works, these additional features might be considered to further refine the reconstructed geometry, improving the description of the GDL transport behavior. A third image is included in the analysis, which corresponds to the stochastic reconstruction conducted by Hinebaugh et al. [69] whose work has accurately reproduced a physical GDL sample.

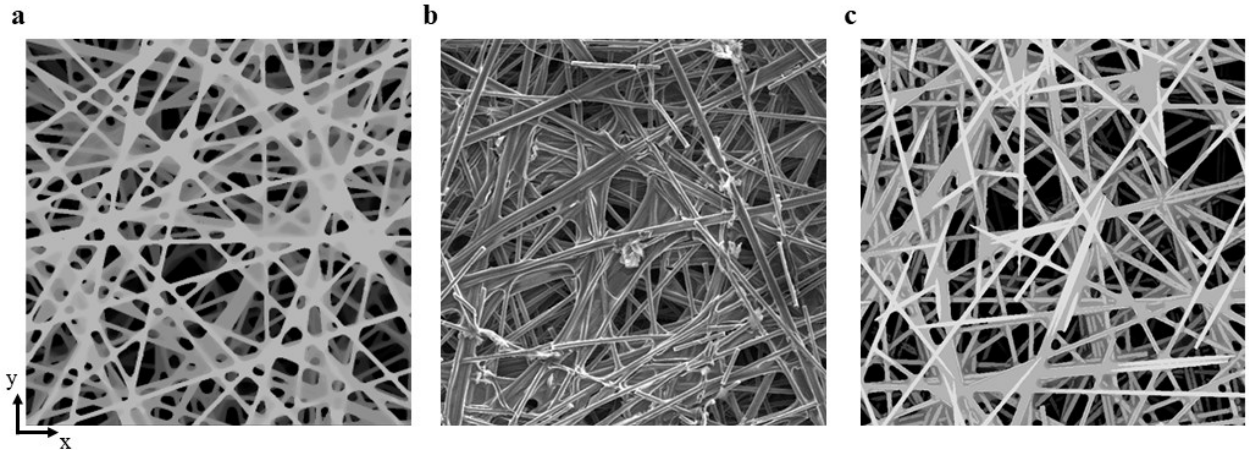

Figure 4.3 Visual comparison of GDL sample from TP direction, 640x640 μm^2. **a**, Virtual sample from this work **b**, Experimental image adapted from *[69]* **c**, Virtual sample adapted from *[69]*.

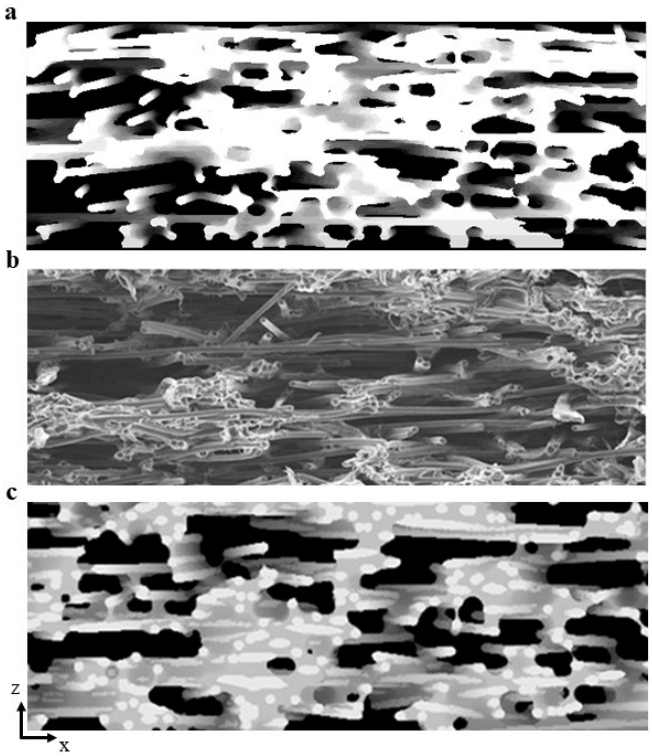

Figure 4.4 Visual comparison of GDL sample from IP direction, 640x220 μm^2. **a**, Virtual sample from this work **b**, Experimental image adapted from *[69]* **c**, Virtual sample adapted from *[69]*.

Despite the assumptions behind the stochastic reconstructions, the virtual GDL visually seems to accurately represent the morphological features of the physical GDL samples. However, it is crucial to carry out a quantitative assessment of the performances.

The sectional porosity in the through-plane direction was chosen as the first metric for comparison with μCT derived experimental data. The sectional porosity of a virtual sample before and after the binder addition is shown in Figure 4.5,. From the plot, the periodic nature of the sectional porosity curves, especially for the bare skeleton (dark curve) becomes evident. This occurs due to the fact that when slicing the geometry along the TP direction, the plane travels recursively through the center of each fiber layer, where the fiber diameters are maximum (hence more solid present) towards the intersection planes of the different layers where the fibers of consecutive layers intersect with reduced in-plane thickness (Figure 4.6). As the binder is added to the skeleton, the average porosity reduces and the periodicity of the skeleton plot is lost. Indeed, Figure 4.5 highlights that the regions of lower porosity in the skeleton curve are mapped to the regions of lower porosity in the skeleton + binder curve.

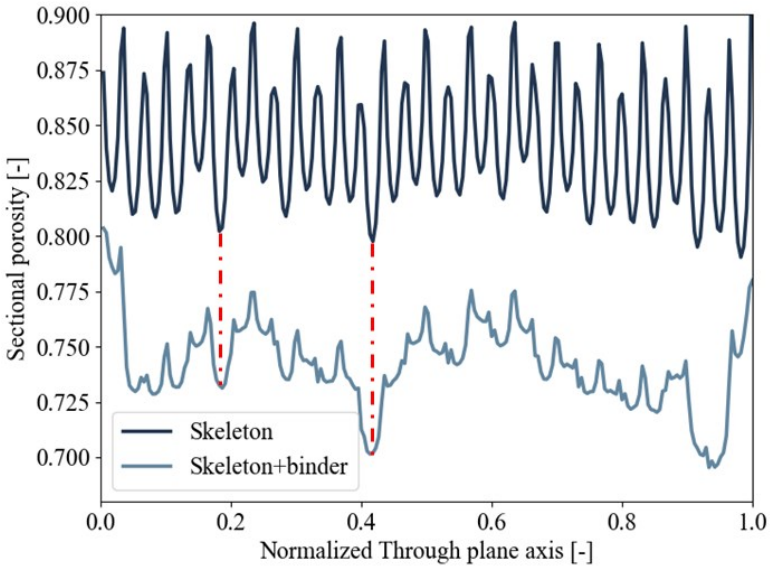

Figure 4.5 Sectional porosity plot for reconstructed sample, before and after the binder addition. The red lines indicates 2D slices which despite having initial porosity, get different amount of binder added.

Nevertheless, having a similar sectional porosity in the skeleton does not guarantee similar amount of added binder. In the skeleton curve, the sectional porosity at x = 0.2 (Figure 4.5) is approximately equal to the sectional porosity at x = 0.4. Still, when mapped to the lower curve, the resulting porosity in the two planes is different (see the red lines in Figure 4.5). In order to provide an explanation for this behavior, Figure 4.7 displays the 2D slices corresponding to those points both before and after the binder addition.

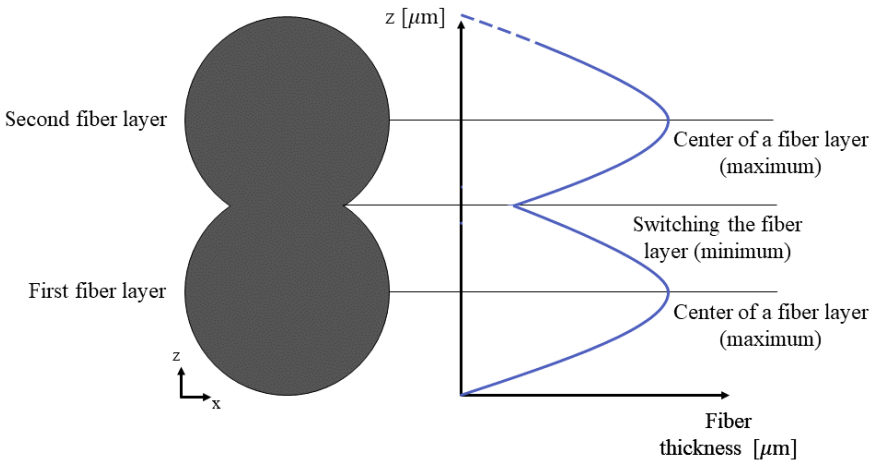

Figure 4.6 Explanation of the periodicity observed in the sectional plots of the GDL skeleton. The fiber thickness periodically oscillates and the porosity changes accordingly.

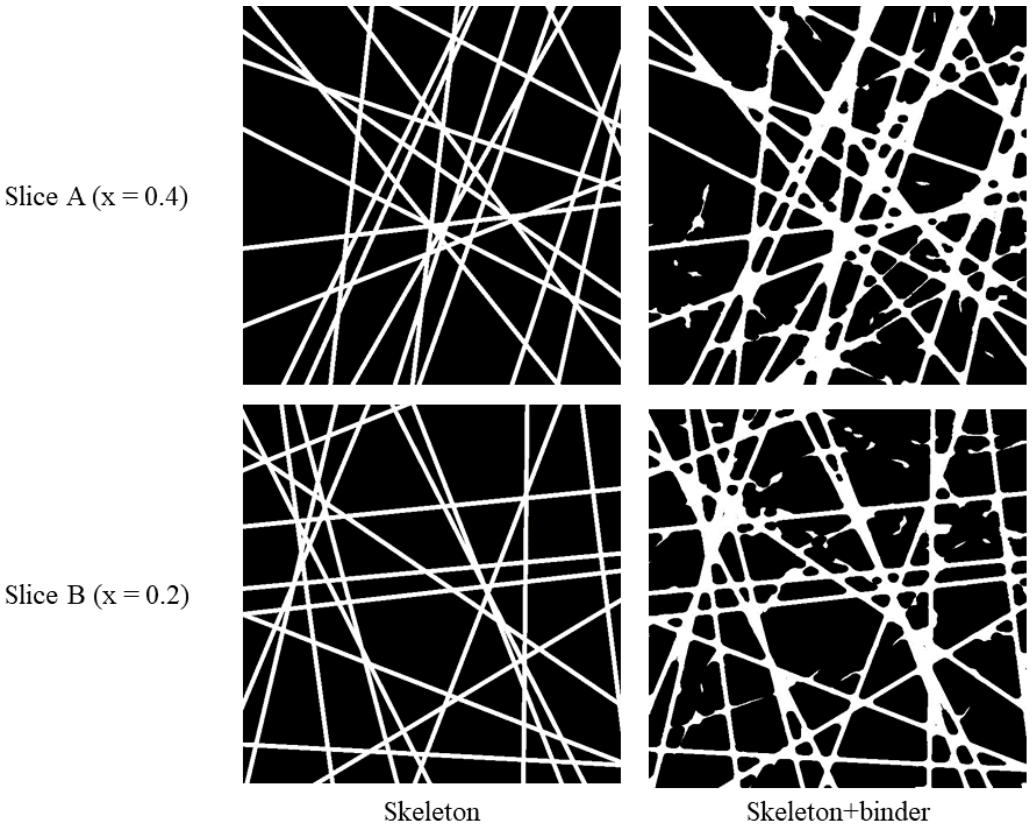

Figure 4.7 2D slices at selected TP distance, before and after the (3D) binder addition.

In both the slices, the number of fibers is the same (18) resulting in a very close sectional porosity (0.802 vs 0.797). The difference could lie in the arrangement of the fibers that creates in the original skeleton a larger number of small pores in the slice at x = 0.4. Consequently, the binder addition process fills these small cavities increasing the amount of binder deposited. Such a hypothesis can be verified by using the pore area distribution reported in Figure 4.8. To this aim, the function "analyze particles" from Fiji ImageJ was used [114]. Before analyzing the results, it is worth to notice that the achieved pore area distribution correspond to the pore size distribution as described by the "discrete" interpretation given in section 3.2.1.

Figure 4.8 shows that no significant differences are noticeable between the pore area distribution of slice A and slice B, meaning that the values of the pore areas and the number of pores with similar areas are similar for both the slices.

Since the specific values and distribution of the pore areas did not quite explain the difference in binder addition in the two sections of the GDL, the next possible analysis was to assess whether the shape of the pores has any effect.

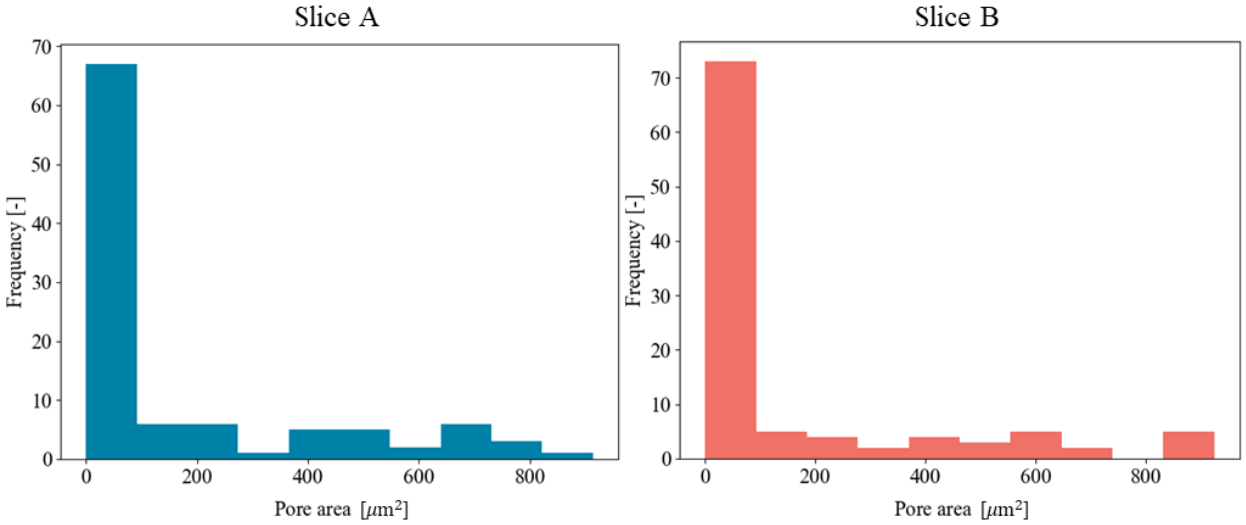

Figure 4.8 Pore area distribution for skeleton slices at selected TP distance. As discussed for the "discrete" approach in the method section, each pore is regarded as a separate entity with a fixed cross-sectional area. The pores having similar areas are grouped and a histogram showing the frequency of occurring of each pore size can be obtained. The comparison does not show significant differences between the two slices.

To proceed in the investigation, the second hypothesis was formulated. Due to the relative orientation of the fibers, in one slice the shape of the pore could be more skewed with respect to those in another slice. Skewed pores may result in higher amounts of binder added without posing any restriction on the area of the pores themselves: imagine having two parallel fibers very close to each other. Binder will fill the gap between the two fibers forming a sort of film. To address this possibility, ellipses were fitted (once again by making use of the "analyze particle" functionality of Fiji ImageJ) inside each pore and the two semiaxes were plot against each other as shown in Figure 4.9. The more a pore is skewed, the higher the difference between the two semiaxes, the higher the distance from the 45° line which represent perfectly circular pores. Also in this case, the different slices in the GDL geometry seem having pores with similar skewness, as no significant differences are noticeable by comparing the semiaxes of the ellipses plotted for both the slices.

The discrepancy between the observed porosity in the different slices in the GDL can then only be explained by considering the effect of the neighboring slices, located above and below the analyzed one. In fact, it is important to consider that since binder addition is a 3D operation, the mutual position of the fibers in neighboring layers can enhance or hamper the binder addition in the z direction (or TP direction).

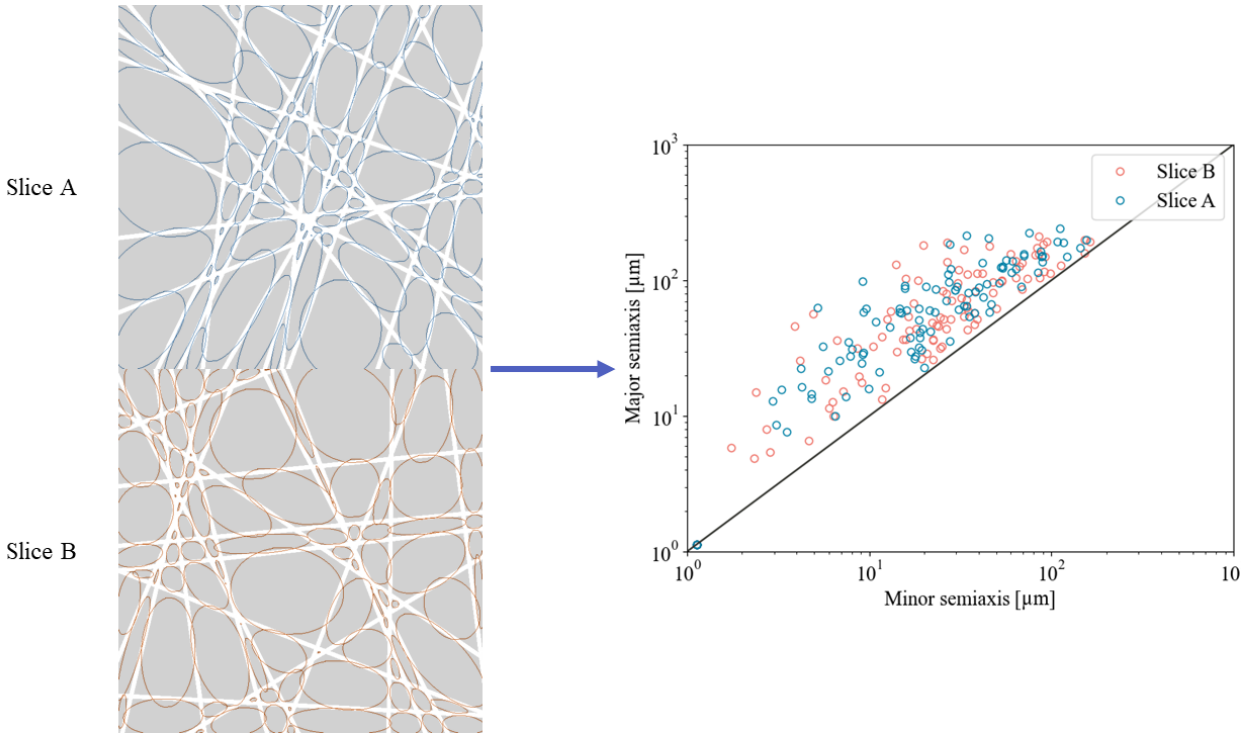

Figure 4.9 Fitted ellipses in pores of skeleton slices at selected TP distance. After having obtained the values of the two semiaxis for both the slices, these are plotted one against the other to highlight the skewness of the pores. The 45 degree line represents pores in which ellipses degenerating into circles have been fitted.

To test the hypothesis of neighboring layers influence, the two slices can be separately considered and binder addition can be performed on them using a 2D disk rather than a 3D sphere as a SE. By doing so, it turns out that the observed difference in the porosity is sensibly lower than what has resulted in the original case. By using a 3D SE, a $\Delta\varepsilon$ of 0.03 was observed, while the 2D SE results in a $\Delta\varepsilon$ three times lower. Overall, the binder is preferentially added in the regions of low porosity but a significant influence comes from the neighboring fiber layers and their fibers orientation within since it can significantly influence the amount of binder added in the TP direction.

Figure 4.10 shows the comparison between two experimentally determined sectional porosity plots and the respective microstructural reconstruction profiles. The difference between the experimental and numerical curves appears in the amplitude and the frequency of the oscillations. The oscillations are a direct consequence of the manufacturing process of carbon paper in which thin fiber sheets are compression molded to reach the desired thickness of the paper. In this sense the virtual geometry

reconstruction captures, even if not precisely, the alternating regions of high and low voidage.

The initial observation that can be made for describing the curves in Figure 4.10 regards the higher smoothness of the experimentally derived curve. This can be attributed mainly to the resolution employed in experimental measurements. In fact, the resolution employed in μCT scans is lower compared to the resolution used in the numerical modeling (e.g., Xiao et al. used 3 μm/voxel [115], whereas this work uses 1 μm/voxel). Consequently, by applying filtering techniques to the numerically obtained curve could potentially yield smoother profiles, aligning them more closely with experimental measurements. The second important observation resides in the amplitude of the oscillations. The simulated curve of figure **b** shows a higher variation in the porosity, ranging from 0.69 in x = 0.67 to 0.85 in x = 0.67 ($\Delta\varepsilon$ = 0.16).

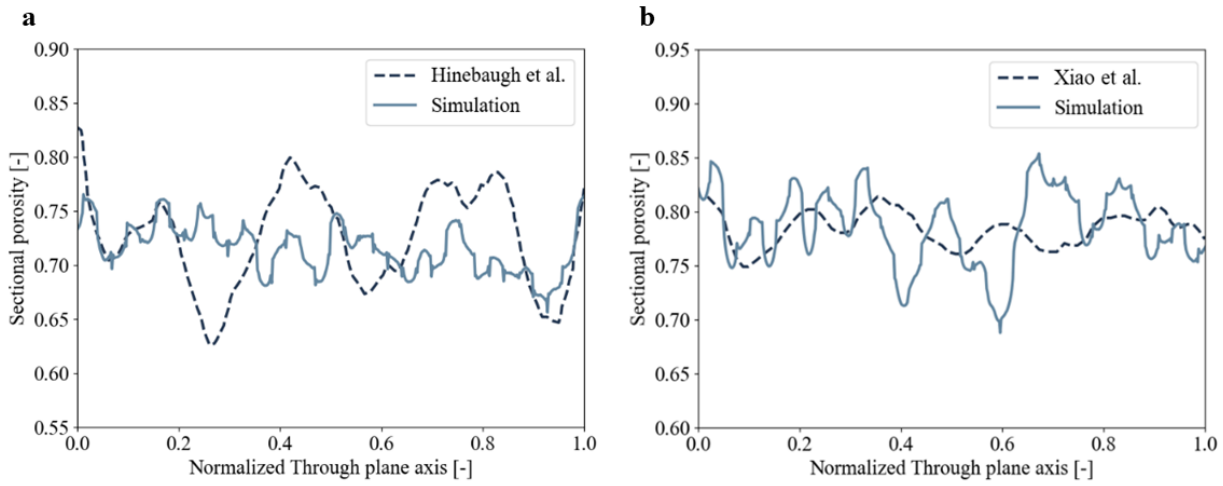

Figure 4.10 Sectional plot validation with selected literature GDL. **a**, Commercial GDL analyzed:Toray TGP-H 90, overall porosity equal to 0.74 *[69]*. **b**, Commercial GDL analyzed: SGL 39AA from Sigracell, overall porosity equal to 0.79 *[115]*.

By contrast, the simulated curve of Figure 4.10 **a** presents a maximum variation in the sectional porosity $\Delta\varepsilon$ = 0.10. The wider distribution of porosity is also reflected in a higher standard deviation of the sectional porosity, as pointed out in Table 5. To understand this behavior, it is important to consider the significant differences in porosity and BVF between the reconstructed geometries. For instance, the sample Figure 4.10 **b**, was reported to have a porosity of 0.79 and a BVF of 0.5. This implies that this structure requires an initial skeleton porosity, calculated using Equation 3.4, of 0.895.

Table 5 Sectional porosity metrics for the two selected geometries.

	Mean porosity ε (literature)	**Mean porosity ε (simulation)**	**Standard deviation (literature)**	**Standard deviation (simulation)**
Hinebaugh et al. [69]	0.7263	0.7151	0.0466	0.0225
Xiao et al. [115]	0.7847	0.7859	0.0161	0.0346

Due to the extremely high porosity of the skeleton, the construction of the geometry requires only a small number of fibers. Consequently, their distribution, although intended to be uniform, exhibits significant variation between different layers. In addition to the uneven distribution of fibers, a significant amount of binder is introduced, with a BVF of 0.5, which is one of the highest reported in the literature. This leads to further enhancement of porosity variation across the entire domain.

Lastly, it has to be considered that the two replicated GDL are manufactured from different firms. In particular, the sample in Figure 4.10 **a** [69] makes use of a Toray carbon paper while the sample in Figure 4.10 b [115] uses a SGL carbon paper. Although there can be specific manufacturing routes that are unique to a specific commercial GDL [45], the used reconstruction method is not capable of distinguishing between the two papers and the only discrimination in this case occurs, of course, by the means of the input parameters (e.g. BVF, fiber diameter and porosity).

The third and last step of the morphology validation involves the comparison of the pore size distribution (PSD). As highlighted in the methods section, the PSD obtained for the GDL geometry depends strongly on the chosen approach for calculating the PSD. Figure 4.11 highlights the difference obtained from assuming different geometrical definitions of PSD.

The image illustrates the difference between the discrete and continuous approaches into 2D and 3D calculations. In 2D calculations, the computation is performed on individual 2D slices of the geometry rather than on the complete three-dimensional

structure and this of course brings to a substantial difference in the computation of the pores radii. Among the five curves it is worth commenting on the results obtained with the discrete 3D definition. Recalling the concept of discrete, each individual pore is treated as a distinct entity with its own volume. The volume is calculated by determining the number of voxels enclosed by the pore and multiplying it by the volume of a single voxel (1 μm^3 in this study). The pore equivalent diameter is then derived using the volume definition of a sphere. The results (cyan curve) clearly show the presence of a single large pore identified by the algorithm, estimated to have an equivalent diameter of approximately 500 μm. This outcome indicates that the void space, consisting of interconnected cavities, is fully connected, meaning that each cavity can be accessed from any location within the pore network. As a result, it can be concluded that the discrete 3D approach provides a quick and effective method for assessing the connectivity of a 3D porous material.

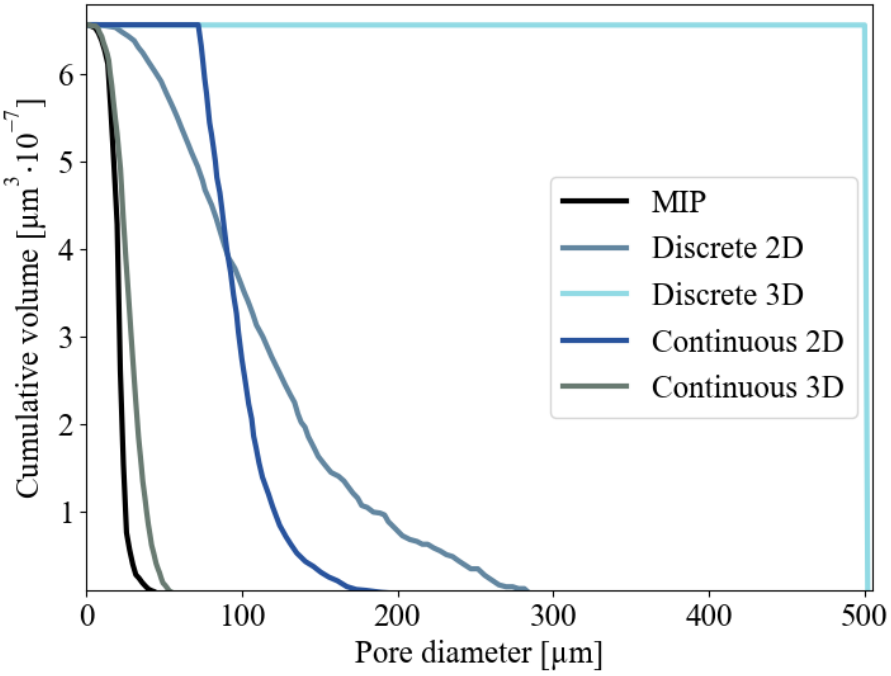

Figure 4.11 Cumulative pore size distribution for a reconstructed sample using different geometrical definitions of PSD.

Two additional observations can be made based on Figure 4.11. Firstly, the MIP and continuous 3D methods demonstrate a strong agreement in their results. This is not surprising, as both methods utilize the same PSD definition (what has been previously

referred to as "continuous" pore size distribution). Secondly, the 2D continuous method detects larger pore diameters compared to the 3D continuous method. This means that the pores are extended more in the x-y plane than in the z direction , as seen in Figure 4.12. This is because as soon as the algorithm tries to fit a sphere in the pore volume, it encounters a solid boundary in the z direction, much before the x and y directions. Therefore, if the semi-axes a, b, and c of a generic ellipse in the 3D continuous approach were not constrained to be equal (as if for a sphere), the computed pore sizes would be larger.

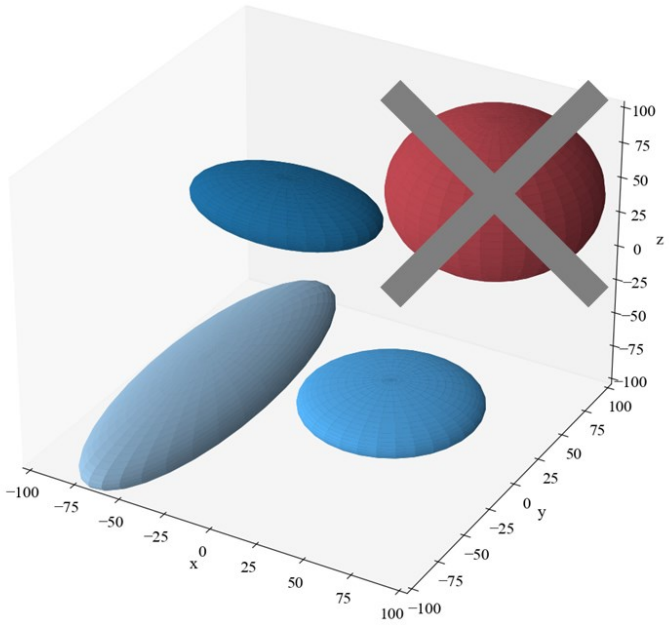

Figure 4.12 Expected pores shape from a "continuous" PSD. The pores are tipically more extended in the x-y direction than in the z directions. Therefore, it is unlikely to have spherical pores (red ball).

To conclude the morphology validation section, the GDLs of selected works in literature were virtually reproduced and the cumulative PSD of the reconstructed geometries was measured with the simulated MIP technique. Figure 4.13 shows the results while Table 6 collects relevant metrics extracted from the PSD (obtained by numerically differentiating the cumulative PSD curve). In the Figure 4.13, although the experimental and simulated curves do not completely overlap, the former define a range (gray shaded area representing an experimental spread in the data) of cumulative PSD, within which the simulated PSD consistently fits. This observation is particularly significant considering that all the studied GDLs are identical commercial GDLs (Toray

TGP-H). This also indicates that the experimental studies are not fully consistent among themselves, even though the analyzed carbon paper comes from the same manufacturer.

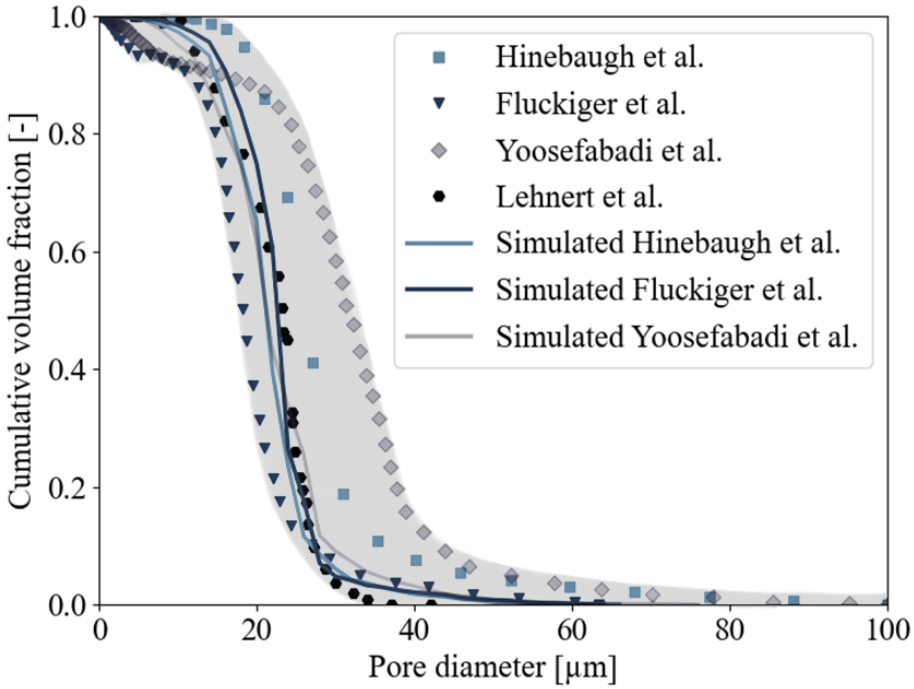

Figure 4.13 Cumulative pore size distribution of selected GDLs. Experimentally measured curves (dotted lines) compared to MIP simulation of the virtual reconstructions (full lines). Experimental data from *[69]*, *[61]*, *[64]*, *[45]*. Lehnert geometry has been added for comparison without any reproduction being constructed.

The MIP measurement method raises a question about its ability to predict varying ranges of PSD when significantly different microstructural parameters are employed. The input parameters used for the geometry reconstruction for obtaining the simulated curves were quite similar, limiting the extent of changes in the computed PSD. Future research will extensively investigate the capability of the methodology by manipulating microstructural parameters. As a preliminary insight into this study, Figure 4.14 presents the cumulative pore size distribution of a GDL reconstruction before and after the binder addition. It can be observed that the curve's shape remains largely unchanged up to a pore diameter of 20 μm. This behavior implies that the binder has predominantly affected the smaller pores, by obstructing their accessibility while leaving the pore space above 20 μm unaffected. Consequently, the total volume of intruded mercury, which represents the overall void space, has experienced a reduction of approximately 12%. Such a change is not negligible and it shows that the MIP simulation method is capable of predicting

changes in the pore space when parameters as the BVF are significantly altered (in future work the effect of the fiber diameter and porosity on the computed PSD will also be assessed).

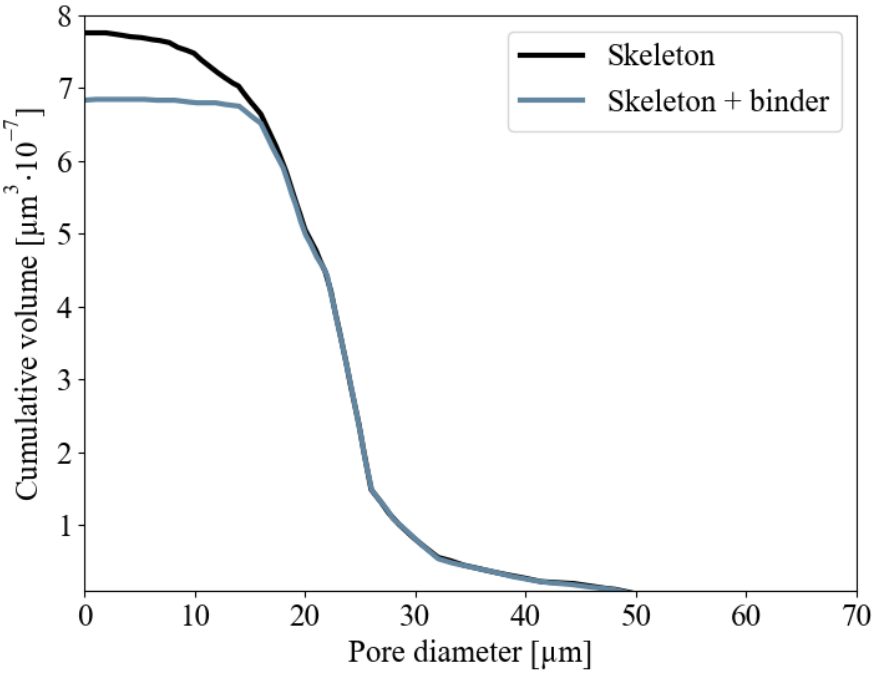

Figure 4.14 Cumulative PSD of a reconstructed GDL sample before and after the binder addition. The existence of smaller pores is suppressed by the closure due to the binder added.

The closure of pores has practical implications for the GDL. It leads to a reduction in the effective diffusivity of the sample as the gas encounters more obstacles and experiences increased tortuosity during diffusion. On the other hand, it results in an increase in the effective conductivity of the GDL due to enhanced connectivity. Additionally, although not specifically evaluated in this study, the closure of pores can also lead to an increase in the saturation of the GDL as the larger average pore dimensions require a lower capillary pressure for penetration from the aqueous electrolyte.

Overall, the conducted morphology validation shows that the virtual GDL generation framework is capable of replicating real carbon paper geometries, at least from a morphological perspective.

Table 6 Pore size distribution metrics for the three selected geometry.

	Mean pore diameter [μm] (literature)	Mean pore diameter [μm] (simulation)	Standard deviation [μm] (literature)	Standard deviation [μm] (simulation)
Hinebaugh et al. [69]	26	21.4	28.1	22.3
Yoosefabadi et al. [64]	34.2	21.9	42.7	23.3
Fluckiger et al. [61]	18	22.6	34.7	23.4

4.2. Geometry validation: transport

In this section, we evaluate the validation of the transport properties in the virtual GDL. Specifically, we analyze the thermal/electrical conductivity and species diffusivity of the GDL using the effective medium approximation. This approach enables us to treat the heterogeneous medium (composed of a solid phase and a gas phase) as a homogeneous medium with well-defined effective transport properties. As discussed in the methods section, it is crucial to ensure that the condition of representative elementary volume is met. The results of the geometrical REV analysis, conducted on a skeleton geometry of 2400x2400x200 μm^3 are reported in Figure 4.15. The candlestick plot allows to visualize the change in the measured porosities when a subdomain is sampled multiple times by cropping the parent geometry. In this case, the skeleton was analyzed for the REV as adding binder with morphological image closing to the parent geometry requires impractical computational resources. In particular, as anticipated in the methods section, since the uncertainty bar (grey area) was reasonably constant in its width by increasing

the domain size starting from 600x600x200, this size was deemed to be reasonable to be taken as geometrical REV, in its statistical connotation.

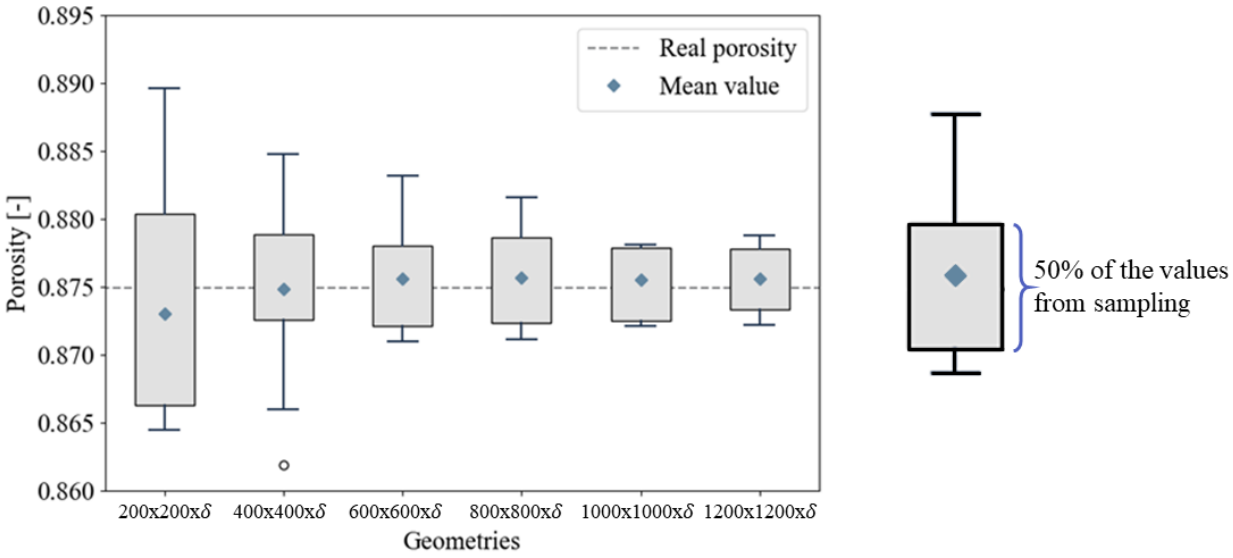

Figure 4.15 Geometrical REV analysis of the skeleton only . The boxplot for each subdomain is the result of different sampling acquired across all around the parent geometry of dimensions 2400x2400xδ μm^3 (with $\delta = 200$ μm). On the right, the Boxplot legend shows that the grey area, or uncertainty bar, collects the 50% of all the values recorded.

The porosity analysis provides a geometrical REV whereas an alternative interpretation in terms of the physical REV analysis can also be derived. The ultimate objective of the study is to establish an equation that correlates the GDL effective transport properties with its microstructural features. To accomplish this, it is essential to uniquely associate a set of morphological properties with a single value of an effective transport property. In other words, regardless of the sample size, the effective transport property under investigation should remain constant for a given set of morphological properties (Equation 4.1).

$$\frac{k_{eff}}{k} = f\left(\varepsilon, size\right) = f\left(\varepsilon\right) \qquad 4.1$$

That is, as long as we use a sufficiently large domain size, there is no functional dependence of the effect transport property on the sample size. This condition is one of

the requirements for establishing correlations, and it can be verified by generating multiple samples with the same porosity but increasing dimensions. If the effective transport property remains unchanged as the sample size varies, then its dependency can be disregarded. The results of this analysis are reported in Table 7 where it can be observed how the transport properties are not significantly affected by the changes in the domain size. A slight deviation is observed for the TP effective conductivity, where the largest changes are observed.

Table 7 Assessing the dependency of the effective transport properties on the domain size.

	200x200x225 ε **= 0.7419**	**300x300x225** ε **= 0.7420**	**400x400x225** ε **= 0.7420**	**500x500x225** ε **= 0.7420**	**600x600x225** ε **= 0.7382**	**640x640x225** ε **= 0.7420**
TP k_{eff}/k	0.0523	0.0521	0.0553	0.0591	0.0651	0.0639
IP k_{eff}/k	0.1799	0.1819	0.1809	0.1802	0.1843	0.1793
TP D_{eff}/D	0.3820	0.3723	0.3769	0.3865	0.3782	0.3859
IP D_{eff}/D	0.4505	0.4629	0.4689	0.4592	0.4451	0.4505

Next, the experimental data on effective transport properties were selected to cover all the effective transport properties needed (TP & IP conductivity and diffusivity). A difficulty arising in this selection procedure was that not all the authors reported in their study the required structural specifications of the GDL needed for its reconstruction. In this sense, the available literature data set was significantly restrained. Virtual reconstruction of these samples was completed and transport simulations were run upon them to compare the results with the empirically acquired values (Table 8). The table shows 5 selected experimental studies. For these, in the second column the structural parameters (ε, Fiber diameter, BVF) are reported and then in the third (conduction) and fourth (diffusion) columns the comparison among simulation and literature value of all the effective transport property ratios is shown.

The primary challenge in conducting this type of analysis arises when it is necessary to obtain accurate information about the morphological parameters to be used, such as fibers diameter and BVF. As shown in the table, there is relatively good agreement

in reporting average fiber diameters around 7-8 μm. However, the reported values for BVF exhibit significant variation, as previously mentioned in the methods section. Concerning the effective diffusivity ratios, both calculated and obtained from literature, generally exhibit a consistent behavior in relation to porosity. As porosity decreases, the effective diffusivity tends to decrease as well, indicating a physical trend. However, the Yoshimune geometry [116] deviates from this pattern, displaying a relatively high diffusivity despite its lower porosity compared to other geometries. On the other hand, the conductivity values show less consistent correlations with porosity. In theory, conductivity should increase as porosity decreases, but this is not always observed in the table. For instance, Yoosefabadi et al. [64] report a TP conductivity ratio of 0.0162 (with porosity of 0.75), while Becker et al. [62] report a value of 0.0122 for the same quantity (with $\varepsilon = 0.74$). Similarly, the simulated geometries of Yoosefabadi et al., Becker et al., and García-Salaberri et al. [112] exhibit poor consistency in IP conductivity ratios. It is also true that, despite this, the computed values generally are within the reported range of values, with few exceptions (such as the diffusivity values computed for the García-Salaberri et al. geometries).

At this stage, it is challenging to determine an exact threshold for what qualifies as "close." To comprehensively assess the impact of changes in effective transport properties on the gas diffusion electrode's performance, a sensitivity analysis with a macroscopic model of the reactor could be conducted. However, by considering the range of variation reported in experimental measurements of effective diffusivity and effective conductivity (10-20 %), the computed values can be considered in agreement with the experimentally observed properties (note that in one case, specifically for the TP conductivity proposed by García-Salaberri et al. , a variation of 150% is reported).

The lack of precise values for the structural parameters at this stage adds an additional level of complexity to the interpretation of the results. Due to the absence of an experimental counterpart in this study, future research would greatly benefit from having access to both microstructural parameters and measured effective transport properties, as they would provide a more reliable basis for validation and analysis. Despite these inherent challenges, the obtained results are physically sound and exhibit a reasonable level of consistency with the corresponding experimental values.

Table 8 Validation of effective conductivity and effective diffusivity predicted by the virtual GDL reconstruction. Legend: STPC = Simulation TP conductivity; LIPD = Literature IP diffusivity; *Fiber diameter and BVF assumed due to missing data; ǂ Values from numerical models.

	ε	Fiber diameter [μm]	BVF	STPC	LTPC	SIPC	LIPC	STPD	LTPD	SIPD	LIPD
Yoshimune et al.* [116]	0.74	8	40%	-	-	-	-	0.3859	0.36±0.02	-	-
Yoosefabadi et al. [64]	0.75	7	45%	0.0114	0.0162	0.1716	0.1587 - 0.1846 ǂ	0.2794	0.26-0.32	0.5821	0.557-0.586ǂ
Becker et al. [62]	0.74	7	50%	0.0140	0.0122	0.1466	0.142	0.2328	0.29	0.5781	0.51
Fluckiger et al. [61]	0.78	8	30%	-	-	-	-	0.4481	0.37	0.5912	0.587
García-Salaberri et al. [112]	0.75	8	40%	0.0140	0.0087 -0.022	0.1715	0.159-0.177	0.3945	0.28-0.34	0.5056	0.52-0.6

4.3. Transport properties correlations

As discussed in the methods section, in order to develop a correlation for the effective transport properties, the functional dependences on the investigated parameters (number of fibers per layer, fiber diameter, binder volume fraction and porosity) must be assessed. Following the procedure depicted in Figure 3.17, it has to be verified if the

effective conductivity and diffusivity ratios, both for the TP and IP directions, can be expressed as a unique function of the porosity (Figure 4.16).

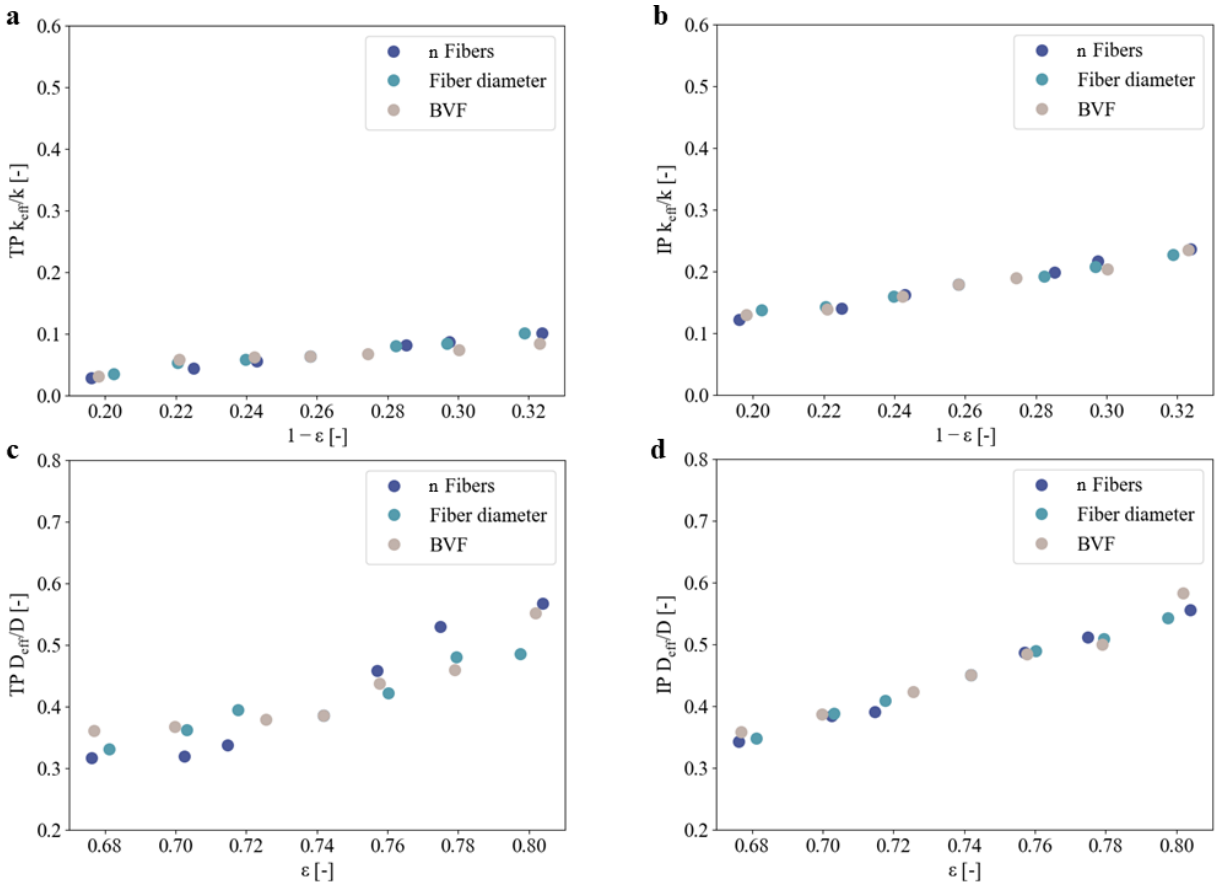

Figure 4.16 Calculated effective transport property ratios when varying different structural parameters. **a**, TP conductivity. **b**, IP conductivity. **c**, TP diffusivity. **d**, IP diffusivity. To ensure a fair comparison among the different plots, a fixed Δy of 0.6 has been used in all the 4 cases.

It is worth noting that, particularly for the IP properties, the points from the three different data sets give similar values of the effective ratio over the whole range of porosities investigated. This is an indication of the fact that for the IP transport, using a correlation uniquely dependent on the porosity of the sample may be sufficient to properly describe the transport phenomena. This unique porosity dependence indicates that regardless of how a change in porosity is achieved (whether through altering d, BVF, or n), the resulting morphology of the geometry in the IP direction will not present changes able to justify a discrepancy in the transport efficacy among the three data sets. Regarding IP heat conduction, it can be observed that increasing the number of fibers has a similar effect on heat transfer as increasing the fiber diameter. Both actions result in

enlarging the cross-sectional area available for heat transfer across the geometry (Figure 4.17). When considering this hypothesis, it is important to note that increasing the number of fibers "n" by one unit entails the inclusion of one more fiber per fiber layer in the GDL. Consequently, the increase in n results in the presence of both additional fibers in the heat flow direction (which significantly contribute to increased heat transfer) and fibers oriented transversely to the heat flow (which marginally contribute to increased heat transfer).

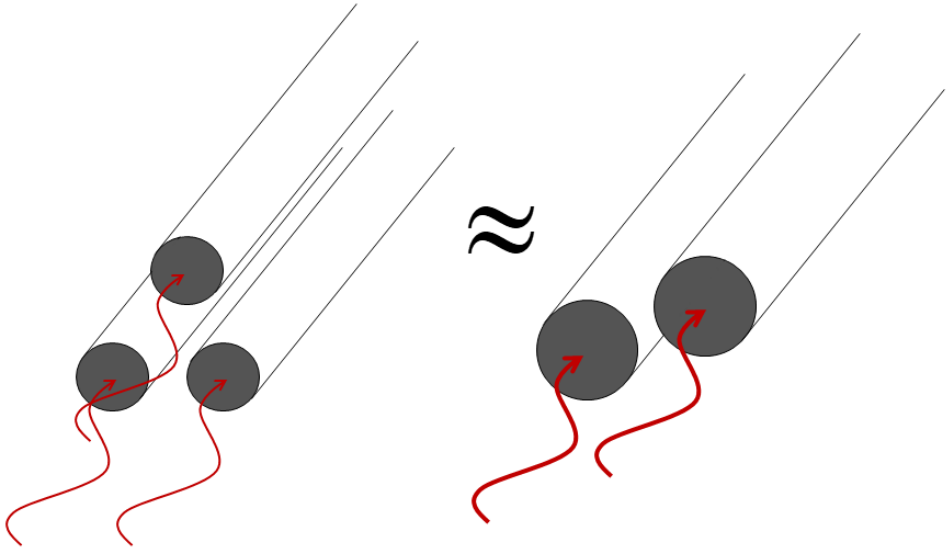

Figure 4.17 Depiction of the equivalence between fiber adding and fiber diameter enlargement for IP transport.

Similarly, the addition of binder has an impact comparable to that of increasing the fiber diameter and number, that is, providing an increased cross section available for heat transfer in the IP direction. This can be visualized in Figure 4.18, where a cross-sectional cut in the x-z plane demonstrates how the binder covering the fibers enhances the available cross-sectional area for conducting heat. The hypothesis that binder addition acts similarly to fibers number or diameter increasing, looks particularly reasonable when considering the presence of fiber bundles that traverse the sample from one side (at a fixed temperature $T_{1)}$ to the other (at a fixed temperature T_2) in the generated geometries (as also visible in Figure 4.7). This arrangement provides an opportunity for the binder to form structures that connect the opposing surfaces at fixed temperatures, facilitating the heat flow. Moreover, the result obtained is valid when assuming that the binder has the same bulk thermal conductivity of the PAN fibers, say when the solid

phases are treated as a unique phase. Therefore, while the effect of n and d would remain the same, when accounting for the intrinsic composite solid character of the GDL by considering two different thermal conductivities for the binder and skeleton, a further dependence on the BVF may be introduced.

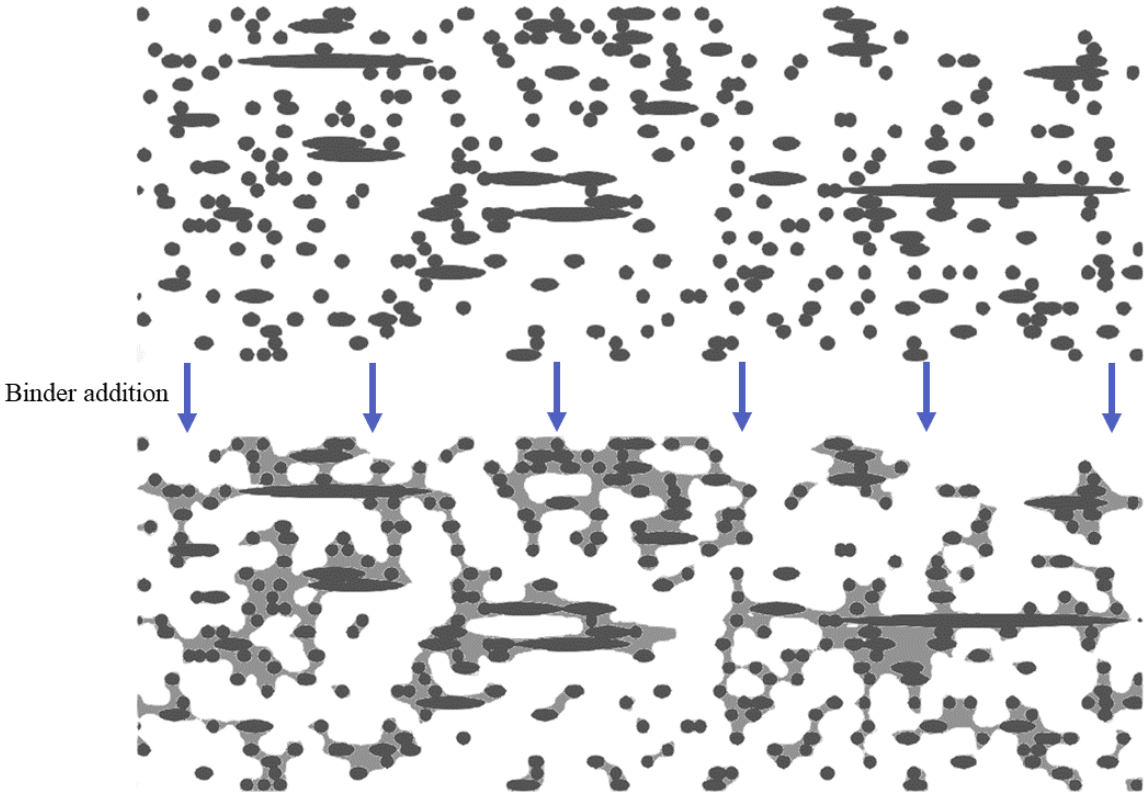

Figure 4.18 Cross section enhancement due to binder addition. 640x640x225 μm^3, # Fibers = 18, d = 8 μm, BVF = 40%.

Coming to the TP transport, the data points for a fixed porosity show higher scattering, especially in the case of gas phase diffusion (Figure 4.16 **c**). For the TP diffusion, a multifactorial correlation may be needed, in which the effective diffusivity ratio is not only a function of the porosity, but also depends on the fiber diameter and the BVF. and further analysis is proposed in this direction as future work. As an anticipation of a possible study conducted in order to rationalize the different behavior of the TP and IP direction when acting on the 3 investigated microstructural parameters, Figure 4.19 has been obtained by taking the 3 reconstructed geometries at ε = 0.8, and plotting the sectional porosity plot in the TP and IP direction. The sectional porosity, that provides an indication of how the solid is distributed along a given direction, does not show

significant differences between the TP and the IP direction. Hence the difference between the two directions in the possibility of expressing the effective properties as a function of the porosity only, has to be searched somewhere else, for example in the connectivity of the geometry, a metric for which the sectional porosity plots do not provide any information.

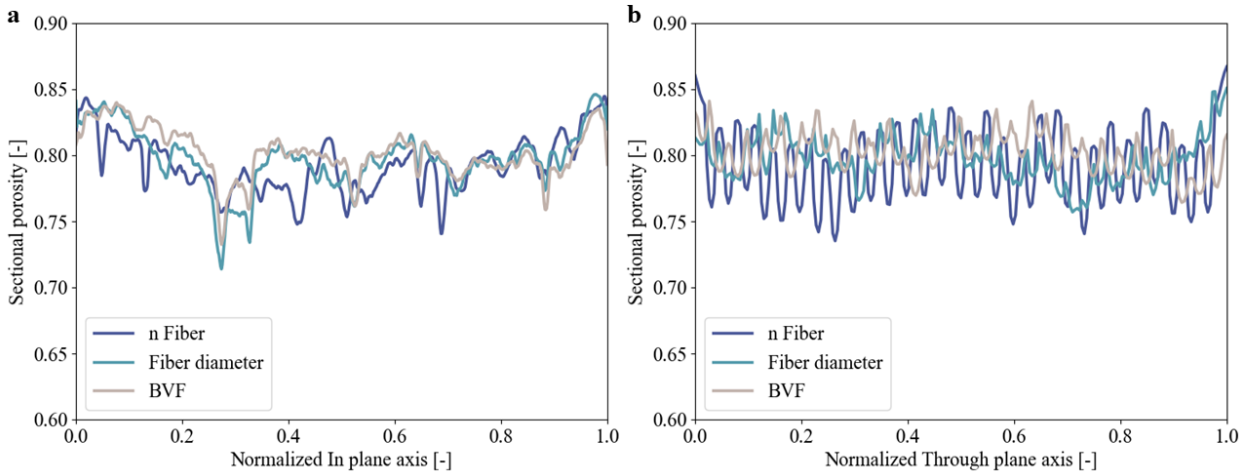

Figure 4.19 Sectional porosity plot of a virtual GDL with $\varepsilon = 0.8$, achieved by acting on n Fiber , Fiber diameter and BVF. **a**, IP sectional porosity. **b**, TP sectional porosity.

In general, the data points adhere to the principles of conduction and diffusion in porous media, indicating that as porosity increases, the effective conductivity tends to decrease, while the effective diffusivity increases.

After this analysis it has been decided to develop a porosity-based monofunctional correlation of the type:

$$\frac{D_{eff}}{D} = a\left(\varepsilon\right)^{m} \tag{4.2}$$

$$\frac{k_{eff}}{k} = a\left(1-\varepsilon\right)^{n} \tag{4.3}$$

for the effective diffusivity and effective conductivity, respectively.

Using these functional forms will also allow to make comparisons with existing correlations, which are mostly based on ε descriptors. Therefore, before extracting the

actual correlations, in Figure 4.20 the data points obtained from the simulation campaign are superimposed over the effective transport property values predicted by correlations selected from literature, over the range of investigated porosities. Although only a few correlations have been selected, it is important to highlight that, to the knowledge of the author, there is a relatively greater availability of correlations for effective diffusivity compared to effective conductivity.

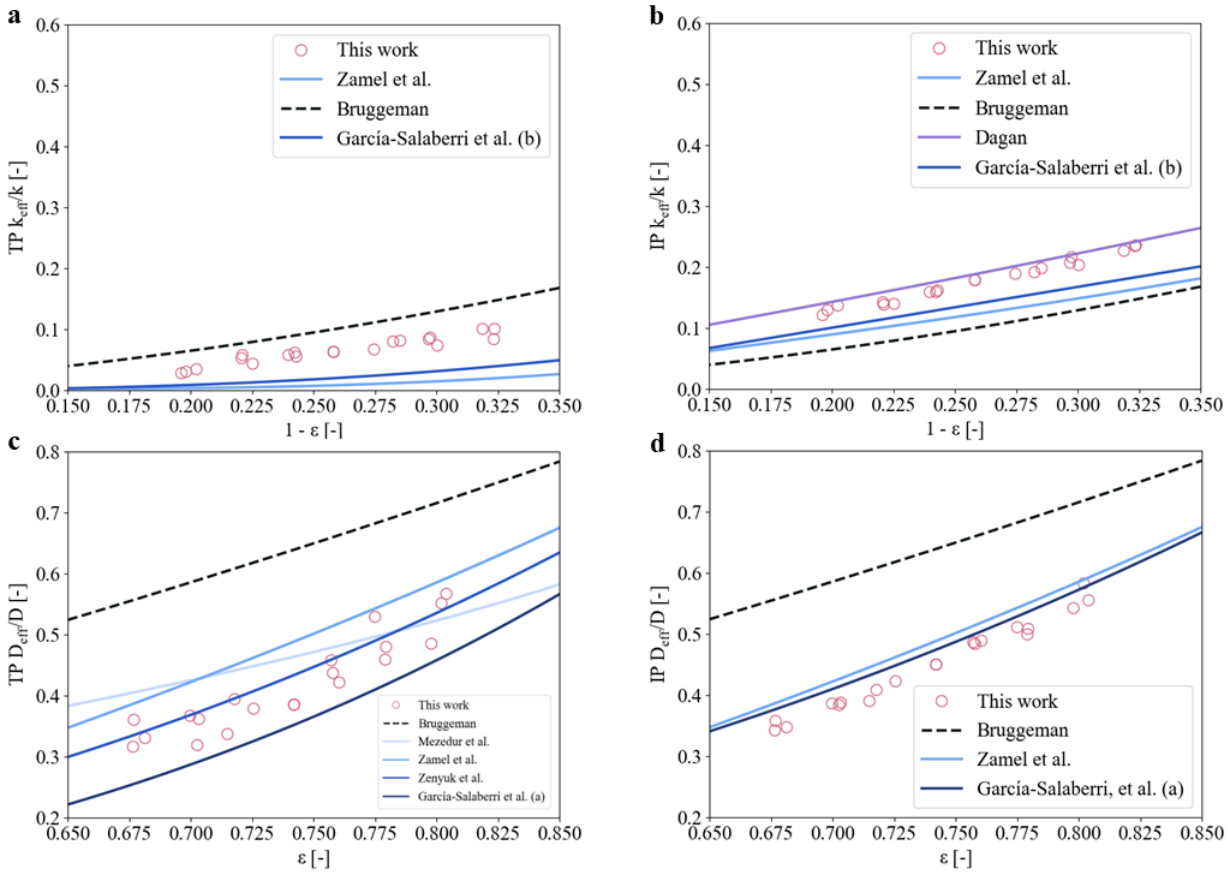

Figure 4.20 Calculated effective transport property ratios vs selected literature correlations. **a**, TP conductivity. **b**, IP conductivity. **c**, TP diffusivity. **d**, IP diffusivity. The correlations are available here *[118]*, *[77]*, *[112]*, *[119]*, *[128]*, *[121]*, *[122]*, *[117]*. For the Bruggeman correlation, m and n of Equations 4.1 and 4.2 are equal to 1.5.

In general, a good agreement is observed with the chosen correlations, which further supports the possibility of relying solely on the porosity as a basis for the entire functional relationship. To be precise, these correlations could also be interpreted in the context of ε/τ models, where being the tortuosity factor τ expressed as a function of ε (Equation 4.4), the latter is the only parameter figuring in the correlation.

$$\frac{D_{eff}}{D} = \left(\frac{\varepsilon}{\tau}\right) = \left(\frac{\varepsilon}{\varepsilon^{p}}\right) = \left(\varepsilon\right)^{1-p} \qquad 4.4$$

The tortuosity factor models the obstruction to free-space transport caused by the geometry of a sample [78]. Due to the fact that the exponent m < 0, it is clear how the tortuosity factor contributes to an additional reduction of the ratio between the effective transport property and its bulk value.

Another interesting feature to highlight is that, contrarily to what has been proposed in the current work, the literature correlations are usually obtained either by compressing a real GDL sample, obtaining a virtual reconstruction at each compression level (each of which entails a different porosity, decreasing as the compression increases) and then simulating the transport via numerical methods [117] or by exclusively varying the amount of fibers inside the domain [118]. Apart from this, all the correlations have been derived specifically for GDLs except for [119], where the correlation is derived theoretically for an isotropic medium of spherical particles. The method employed though, as long as the hypothesis on the unique functionality of the GDL porosity is not relaxed, is not relevant to the development of the correlation.

In the plots, when predicting the effective diffusivity, it is evident that the Bruggeman correlation tends to significantly overestimate its value in both the TP and IP directions. In terms of ε/τ models, this means that the Bruggeman correlation typically predicts less tortuosity (p = - 0.5). On the other hand, when predicting the effective conductivity, the correlation shows an overestimation in one case (TP direction) and an underestimation in the other case (IP direction), although the discrepancies are relatively smaller for both transport properties.

With these premises, the dataset is now utilized to establish effective property correlations. As shown in Figure 4.21 Equations 4.2 and 4.3 have been used for the procedure, apart for the IP conduction, where a better fit was achieved using a simple linear equation. Additionally, for all the curves asymptotical constraints were added to provide more physically sound correlations. In particular for the power laws (Equations 4.2 and 4.3) the multiplicative coefficient "a" was forced to be 1 in order to give consistency when the porosity assumes the values 0 and 1, while for the linear equation of the IP conductivity the only constraint assumed was that the effective conductivity ratio must be equal to 0 when ε goes to 1 (choosing both the asymptotical constraints for

a linear equation would have resulted in a completely determined line with no additional degree of freedom available for the optimization).

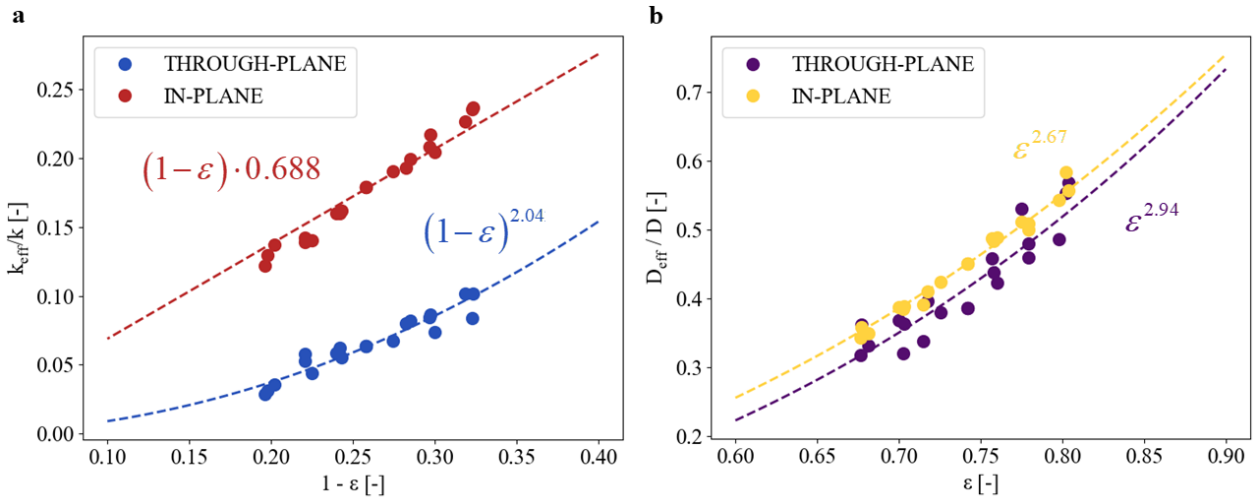

Figure 4.21 Correlations for effective transport properties in gas diffusion layer. a, Effective conductivity ratio. b, Effective diffusivity ratio.

For what concerns the effective conductivity, two main observations can be made. At first, due to the anisotropic character of the analyzed geometry the IP effective conductivity is higher than the TP one (from 2 to 4 times higher depending on the porosity considered). The heat in fact, travels a diverse path whether flowing in the IP or TP direction. In the IP direction, the problem can be effectively thought as heat flowing longitudinally in straight wires from one side of the geometry to the other (with the additional complication of fibers aligned perpendicularly to the heat flux). In the TP direction instead, heat flow through a constricted fiber intersection to reach the subsequent fiber layer, a situation which naturally entails then a longer path to be travelled when considering many fiber layers stacked over each other. This difference could be explained in terms of "tortuosity" of the path the heat has to travel, which is the extent of the deviation from a straight path. Where fibers are oriented parallel to the x-y plane, one can expect higher tortuosity in the TP direction, which in fact is captured by the different functional form of the correlations. These results are also similar to what has been achieved by Garcìa-Salaberri et al. [112], where a linear equation has been used to describe the IP conductivity and a power law for the TP one. In their work though, the asymptotical value for $\varepsilon = 1$ has not been enforced, bringing to a negative conductivity when the porosity is higher than 0.95.

Interestingly, differently to what has been consistently found for porous media, the multiplicative coefficient of the proposed correlation for the IP conductivity is about 2/3 (0.688) while in previous works it has been shown how for porous media approaching the unitary porosity, the multiplicative coefficient is rather 1/3 (due to the tortuosity τ approaching the value of 3) [120].

For what concerns the effective diffusivity instead, the effect of the porosity is rather similar for both the TP and IP direction. Moderately higher values are achieved for the IP case, showing how the void path in this direction may be less tortuous with respect to the TP one. This result is slightly in contrast to what has been found previously in literature. In fact, as seen in Figure 4.20**c**, apart from the Zenyuk correlation [117] which is in accordance with the data points from the simulations (and consequently shows a similar functional form: $D_{eff}/D = \varepsilon^{2.8}$ vs $D_{eff}/D = \varepsilon^{2.94}$ of the current work), the others correlations (Zamel [121] and Garcìa-Salaberri [122]) span sensibly lower values in the TP direction, showing strong anisotropicity also for the gas diffusion. To visualize the anisotropic nature of the GDL transport properties in the two investigated directions, it is convenient to plot their ratio as a function of the porosity (Figure 4.22).

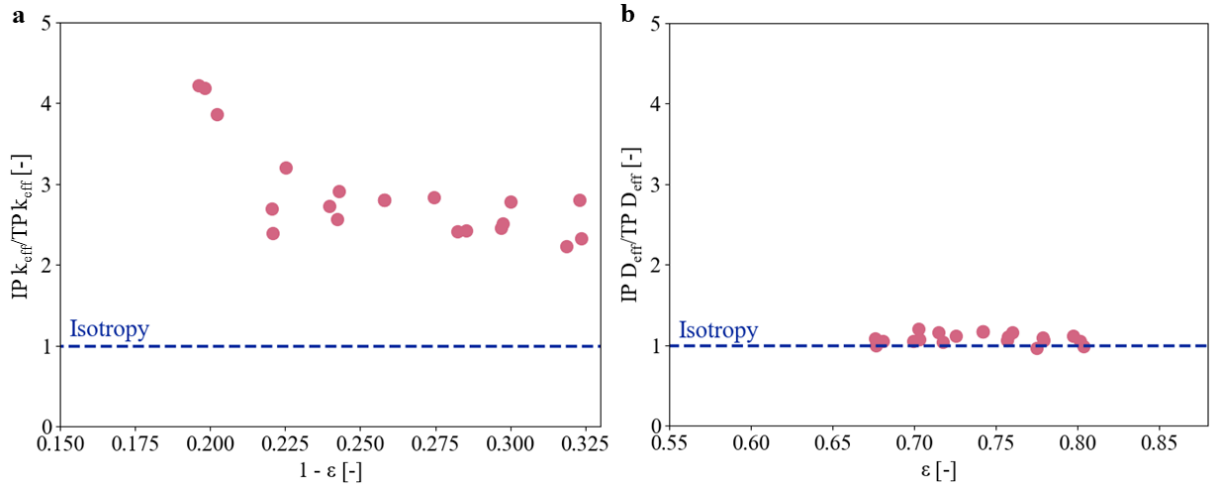

Figure 4.22 Anisotropicity visualized. Ratio between the IP and TP effective transport properties. **a**, Heat/electrons conduction. **b**, Gas diffusion.

It is particularly evident in this case, how for the effective diffusivity all the data points show a ratio around 1. As previously stated, this result is in contrast with what has been observed in previous literature experimental studies. One possibility for this discrepancy could be that in the current work the binder material has been added with approximately spherical structuring element, thus resulting in binder being added not only in the x-y plane but also in the TP direction. Without direct observation through

tomographic scans, it is challenging to infer whether this occurs in physical samples of GDLs. However, if binder is mainly spread in the x-y plane this would explain the lower effective diffusivity observed for the TP direction, due to the lower cross-sectional area available for the species to diffuse. This hypothesis will be addressed in future works by generating geometries with binder added mostly in the x-y plane and eventually by a careful inspection of 3D tomographic scans.

On the contrary, the effective conductivity is clearly anisotropic. As a result, the IP transport is much more higher than the TP one. Additionally, a clear decreasing pattern is observed in the conduction plot, meaning that as soon as the porosity is decreased (say $1 - \varepsilon$ is increased) the geometry becomes more and more isotropic. In the limit of ε reaching zero, say when there is no more void space and the geometry is a mere solid block of carbon, the ratio IP/TP effective conductivity also goes to one, as a unique value has been used for describing the bulk thermal conductivity of carbon. Note that also this assumption could be subject of further analysis as in principle, depending on its allotropic form, carbon may have different thermal conductivities according to the selected spatial direction [123].

Appendix B provides the numerical results of the simulation campaign developed for obtaining the correlations. The samples analyzed are ordered in a way which reflects the parameters varied and those kept constant for each data set (e.g. first n is changed, than the fiber diameter and lastly the BVF).

Additionally, in Table 9, metrics for assessing the accuracy of the derived correlations are also reported. As exemplified by the R^2 values, the approximation of porosity dependent effective transport properties seems once again reliable. In fact, except for the TP effective diffusivity which shows an R^2 coefficient of 0.86, all the other R^2 are higher or equal to 0.90. Hence, considering that all the other transport properties can be accurately described solely in terms of porosity, it is reasonable to consider conducting additional simulations in the future to evaluate whether the approximation still holds true for estimating TP diffusivity. This would further support the generality of the approach followed.

To conclude this section, the macroscopic model presented in chapter 3.4 is used to show the effect of using different correlations in the prediction of the partial current density achieved at a given applied potential. Of course, in order to see how the effective diffusivity affects the performance of the GDE, the system has to be forced to work in mass transfer regime.

Table 9 Accuracy of the transport properties correlations. * The maximum distance of the simulation points from the fitted line.

	TPC	IPC	TPD	IPD
R^2	0.90	0.94	0.86	0.98
Maximum relative distance*	24.54%	10.98%	12.27%	4.83%
Mean square error	4.12e-5	6.68-5	7.57e-4	8.78e-5

To this purpose, while in thermal systems one typically acts on the temperature to increase the reaction rate and to observe a depletion of the species concentration in correspondence of the catalytic surface, in electrochemical systems, as seen with the expression of the reaction kinetics by Tafel (Equation 2.39), it is possible to act on the overpotential, i.e the difference between the real electrical potential applied to the cell and the thermodynamic potential, to produce a similar effect. The overpotential is just a function of the potential applied to the GDL and of the pH (for the liquid potential a value of 0 V has been assumed for simplicity).

In Table 10, the partial current densities obtained at different potential either when using the Bruggeman correlation or the proposed correlation are shown. It can be seen from the table that up to -1.7 V, no differences are present in term of the achieved CO current density (or reaction rate). This means that the cell is still working in chemical regime, with no effect of transport limitations in the GFL. When the potential applied is lower than -1.8 V, it is possible to observe how the two predicted current densities start to diverge.

As anticipated, the Bruggeman correlation tends to overestimate the effective diffusivity at a specific porosity, leading to higher current density when applied. Conversely, when using the developed correlation, the current density obtained is lower. The final remark is that, in practice, gas diffusion electrodes reach their mass transfer regime earlier than what is predicted by the Bruggeman correlation.

Table 10 Carbon monoxide partial current density predicted by the macroscopic model. Effect of the Bruggeman correlation and the developed correlation for the effective diffusivity of the gas diffusion layer.

ϕ_{SHE} [V]	j_{CO} (Bruggeman) [mA/cm²]	j_{CO} (this work) [mA/cm²]
-0.9	9.34e-2	9.34e-2
-1.2	3.77	3.77
-1.7	15.31	15.31
-1.8	118.97	104.07
-1.9	396.74	237.33
-2.0	1220.74	446.12
-2.1	2951.72	2336.41

5 Conclusion

In this work, the effective solid thermal conductivity and effective gaseous diffusivity of gas diffusion layers commonly employed in vapor-fed CO_2 electrolyzer, have been analyzed by means of 3D computational fluid dynamics simulations on virtually-generated GDL samples.

The developed geometry generation framework, a microstructural parameters-based stochastic reconstruction of the GDL, has been tested and validated using literature-available morphological data. The reconstructed samples have been endowed with two solid phases, the polyacrylonitrile carbon fibers and the phenolic binder, the latter needed to stick together the fibers bundle. The Teflon coating (PTFE) used for increasing the hydrophobicity of the paper was excluded from the reconstruction.

The geometrical representative elementary volume (REV) has been determined in its statistical interpretation, and the resulting domain size, used in the next analyses was 600x600x200 μm^3. For what concerns the physical REV, a simplified analysis have shown how using a domain size of 600x600x200 μm^3 allows for excluding the dependence of the effective transport properties on the domain size.

Morphological metrics such as the sectional porosity profile and the pore size distribution of the resulting samples were analyzed. Particularly with respect to the PSD, a thorough analysis revealed that PSD of the generated geometries is comparable to the ones reported in literature for the Toray TGP commercial GDL. Parallelly to this analysis, the importance of univocally establish the geometrical definition of pore size distribution in order to achieve meaningful comparisons with experimentally obtained PSD curves has also been highlighted. Further geometry validation has followed, based on the calculation of effective transport properties of real carbon paper previously analyzed in literature. Also in this case the simulated values were comparable to the literature reported transport properties.

After the validation, engineering correlations for the effective conductivity and diffusivity were developed. The initial aim was to assess the dependence of the effective transport properties on structural microparameters such as the fiber diameter, the binder

volume fraction, the number of fibers per fiber layer and the porosity. After having conducted a detailed simulation campaign, a negligible dependence for all the parameters except from the porosity has been found. This was particularly true for the In-plane effective transport properties for which the coefficient of determination R^2 of the fitted correlations were indeed high enough to exclude other dependencies from the investigated parameters. Further analysis has to be conducted on the diffusive TP transport properties, for which the assumption of porosity-dependent transport was less consistent with the observed results. Next, correlations for describing the effective properties of the GDL as a function of the porosity were determined and compared with empirically derived and theoretically based correlations for GDL porous media. The Bruggeman correlation, typically employed in the description of transport in porous media has been shown to be substantially inaccurate in the prediction of GDLs effective transport properties. To further emphasize the latter result, when the Bruggeman and the developed effective diffusivity correlations were used in a macroscopic model of a vapor-fed CO_2 electrolyzer, the predicted CO partial current density was observed to vary substantially. This discrepancy was due to the fact that the Bruggeman correlation significantly overpredicts the effective diffusivity of gaseous species in the GDL, allowing for less resistance to the species transport in this medium and consequently higher reaction rates achieved in the catalyst layer.

Before concluding this study, the author recommends exploring the following research paths as potential opportunities for future work.

At first, since the geometry generation framework has been validated, the tool can be used by fine-tuning the microstructural parameters, to find the structure of the GDL that can simultaneously optimize species diffusion and electricity/heat transport based on the operating conditions and target yields of interest. In order to conduct this analysis a macroscopic model which solves for both the solid conduction and gaseous diffusion is needed to understand which of the two phenomena assumes a major relevance in optimizing the desired KPI of the cell.

Moreover, for extending the validity of the present analysis in terms of the calculated effective conductivity, two solid phase conduction simulations can be carried out to account for the different bulk thermal conductivity of the fibers and the binder. By doing so it will be possible to assess the dependence of the effective conductivity on the binder volume fraction more accurately.

The geometry reconstruction can be used, following a methodology perfectly analogous to the one used for determining the effective conductivity and diffusivity, to find the effective permeability of the GDL. By solving the Navier-Stokes equations which

describe the momentum balance on a microscopic level, the Darcy's law allows for the calculation of the effective permeability in the creeping flow regime, where the viscous interactions between the porous solid and the fluid dominates the pressure drops.

Finally, it is important to note that this study did not examine the influence of microstructural factors such as pore connectivity and pore size distribution, as well as the hydrophobicity of the gas diffusion layer, on the saturation of the GDL. Therefore, for a comprehensive understanding of GDL physics, it is crucial to account for these factors as they play a significant role in determining the optimal structure of the substrate and should be considered in the microstructure optimization process.

Apart from the specific results achieved in the current work, from a methodological standpoint, this study presents a unified simulation framework to generate virtual electrode structures to replicate the overall characteristics of physical gas diffusion layers, simulating transport processes and hierarchically refining the macroscopic lumped parameters, facilitating the precise investigation of the effective transport properties. As such, the study is deemed to be insightful in enhancing the understanding of GDLs structure-dependent properties, a knowledge that is particularly useful when thinking of engineering the gas diffusion media of electrochemical cells.

Bibliography

[1] R. P. Feynman, R. B. Leighton and M. Sands, The Feynman Lectures on Physics, Basic Books, 2011.

[2] C. McFadden, "The Kardashev Scale: How Far Can Humanity Advance as a Civilization?," Interesting Engineering, 2019. [Online]. Available: https://interestingengineering.com/science/sizing-up-a-civilization-with-the-kardashev-scale. [Accessed 26 03 2023].

[3] V. Smil, How The World Really Works, Dublin: Penguin Random House UK, 2022.

[4] H. Ritchie, M. Roser and P. Rosado, "Energy Production and Consumption," Our World in Data, 2022. [Online]. Available: https://ourworldindata.org/energy-production-consumption. [Accessed 26 03 2023].

[5] U. N. ""World Population From Year 0 to Stabilization"," in *The World at Six Billions*, 1999, p. 5.

[6] R. J. Fragaszy, J. C. Santamarina, A. Amekudzi, D. Assimaki, R. Bachus, S. E. Burns, M. Cha, G. C. Cho, D. D. Cortes, D. N. Espinoza, L. Garrow, H. Huang, J. Jang, J. W. Jung, S. Kim, K. Kurtis, C. Lee, C. Pasten, H. Phadnis, G. Rix, H. S. Shin, M. C. Torres and C. Tsouris, "Sustainable Development and Energy Geotechnology− Potential Roles for Geotechnical Engineering," *KSCE Journal of Civil Engineering,* vol. 15, no. 4, pp. 611-621, 2011.

[7] C. Pasten and J. C. Santamarina, "Energy and quality of life," *Energy Policy,* vol. 49, pp. 468-476, 2012.

[8] World Commission on Environment and Developement, "Report of the World Commission on Environment and Development: Our Common Future," Oxford University Press, 1987.

[9] Y. Kaya and K. Yokobori, Environment, energy, and economy: Strategies for sustainability, Tokyo: United Nations University Press, 1997.

[10] S. Carrà, "The role of energy in technological dynamics," *Structural Change and Economic Dyanmics,* vol. 61, pp. 486-494, 2022.

[11] World Economic Forum, "Energy Vision 2013, Energy transitions: Past and Future," January 2013. [Online]. Available: https://www3.weforum.org/docs/WEF_EN_EnergyVision_Report_2013.pdf. [Accessed 30 03 2023].

[12] N. Muralidharan, E. C. Self, M. Dixit, Z. Du, R. Essehli, R. Amin, J. Nanda and I. Belharouak, "Next-Generation Cobalt-Free Cathodes – A Prospective Solution to the Battery Industry's Cobalt Problem," *Advanced Energy Materials,* vol. 12, p. 2103050, 2022.

[13] Engineering Toolbox, "Fossil and Alternative Fuels - Energy Content," 2008. [Online]. Available: https://www.engineeringtoolbox.com/fossil-fuels-energy-content-d_1298.html. [Accessed 30 03 2023].

[14] T. F. Jaramillo, "Tom Jaramillo , Developing Sustainable Pathways to Fuels and Chemicals, Energy Seminar," Stanford Energy, 21 09 2015. [Online]. Available: https://www.youtube.com/watch?v=E2ZaOTBYS3Q.

[15] International Energy Agency, "The Future of Petrochemicals, Towards more sustainable plastics and fertilisers," 2018.

[16] R. Ayres, "Gaps in Mainstream Economics: Energy, Growth, and Sustainability," in *Green Economy Reader. Studies in Ecological Economics*, Cham, Springer, 2017, pp. 39-53.

[17] Canada Energy Regulator, "Market Snapshot: Petrochemical products in everyday life," 17 10 2018. [Online]. Available: https://www.cer-rec.gc.ca/en/data-analysis/energy-markets/market-snapshots/2018/market-snapshot-petrochemical-products-in-everyday-life.html. [Accessed 31 3 2023].

[18] V. Smil, "What we need to know about the pace of decarbonization," *Substantia,* vol. 3, no. 2, pp. 69-73, 2019.

[19] NASA, "Earth Orbit Environmental Heating," 1999. [Online]. Available: https://llis.nasa.gov/lesson/693. [Accessed 31 03 2023].

[20] J. Nørskov, "Catalysis for sustainable energy , Energy@Stanford and SLAC," 08 09 2014. [Online]. Available: https://www.youtube.com/watch?v=NoYxxygZm3s. [Accessed 31 03 2023].

[21] D. Leythaeuser, "Volume 1. Exploration, Production and Transport," in *ENI Encyclopedia of Hydrocarbons*, Treccani, 2005, pp. 65-73.

[22] O. Wilhelm, "Catalysis," *Zeitschrift für Elektrochemie,* vol. 7, pp. 995-1003, 1901.

[23] R. I. Masel, Chemical Kinetics and Catalysis, Wiley Interscience, 2001.

[24] A. Alvarez, M. Borges, J. J. Corral-Pérez, J. G. Olcina, L. Hu, D. Cornu, R. Huang, D. Stoian and A. Urakawa, "CO2 Activation over Catalytic Surfaces," *ChemPhysChem,* vol. 18, no. 22, pp. 3084-3285, 2017.

[25] C. Pappijn, M. Ruitenbeek, M.-F. Reyniers and K. Van Geem, "Challenges and Opportunities of Carbon Capture and Utilization: Electrochemical Conversion of CO2 to Ethylene," *Frontiers in Energy Research,* vol. 8:557466, 2020.

[26] United Nations Framework Convention on Climate Change, "Background paper on decarbonization technologies for sustainable road mobility," Technology Executive Committee, 2022.

[27] IEA, "Net Zero by 2050," IEA, Paris, 2021. [Online]. Available: https://www.iea.org/reports/net-zero-by-2050. [Accessed 25 04 2023].

[28] S. Nitopi, E. Bertheussen, S. B. Scott, X. Liu, A. K. Engstfeld, S. Horch, B. Seger, I. E. L. Stephens, K. Chan, C. Hahn, J. K. Nørskov, T. F. Jaramillo and I. Chorkendorff, "Progress and Perspectives of Electrochemical CO2 Reduction on Copper in Aqueous Electrolyte," *Chemical Reviews,* vol. 119, pp. 7610-7672, 2019.

[29] M. Gattrell, N. Gupta and A. Co, "A review of the aqueous electrochemical reduction of CO2 to hydrocarbons at copper," *Journal of Electroanalytical Chemistry,* vol. 594, pp. 1-19, 2006.

[30] H. R. M. Jhong, S. Ma and P. J. A. Kenis, "Electrochemical conversion of CO2 to useful chemicals: current status, remaining challenges, and future opportunities," *Current Opinion in Chemical Engineering,* vol. 2, pp. 191-199, 2013.

[31] J. Yu, J. Wang, Y. Ma, J. Zhou, Y. Wang, P. Lu, J. Yin, R. Ye, Z. Zhu and Z. Fan, "Recent Progresses in Electrochemical Carbon Dioxide Reduction on Copper-Based Catalysts toward Multicarbon Products," *Advanced Functional Materials,* vol. 31, p. 2102151, 2021.

[32] Eurostat Statistics Explained, "Electricity price statistics," EU, 2022. [Online]. Available: https://ec.europa.eu/eurostat/statistics-explained/index.php?title=Electricity_price_statistics#Electricity_prices_for_non-household_consumers. [Accessed 25 04 2023].

[33] J. Newman and K. E. Thomas-Alyea, Electrochemical Systems, Hoboken, New Jersey: Wiley-Interscience, 2004.

[34] D. M. Weekes, D. A. Salvatore, A. Reyes, A. Huang and C. P. Berlinguette, "Electrolytic CO2 reduction in a Flow Cell," *Accounts of Chemical Research,* vol. 51, pp. 910-918, 2018.

[35] S. Garg, M. Li, A. Z. Weber, L. Ge, L. Li, V. Rudolph, G. Wang and T. E. Rufford, "Advances and challenges in electrochemical CO2 reduction processes: an engineering and design perspective looking beyond new catalyst materials," *Journal of Materials Chemistry A,* vol. 8, pp. 1511-1544, 2020.

[36] D. Higgins, C. Hahn, C. Xiang, T. F. Jaramillo and A. Z. Weber, "Gas-Diffusion Electrodes for Carbon Dioxide Reduction: A New Paradigm," *ACS Energy Letters,* vol. 4, pp. 317-324, 2019.

[37] S. Hernandez-Aldave and E. Andreoli, "Fundamentals of Gas Diffusion Electrodes and Electrolysers for Carbon Dioxide Utilisation: Challenges and Opportunities," *Catalysts,* vol. 10, no. 6, 2020.

[38] L.-C. Weng, A. T. Bell and A. Z. Weber, "Modeling gas-diffusion electrodes for CO2 reduction," *Phisycal Chemisty Chemical Physics,* vol. 20, pp. 16973-16984, 2018.

[39] J. Lin, S. Yan, C. Zhang, Q. Hu and Z. Cheng, "Electroreduction of CO2 toward High Current Density," *Processes,* vol. 10, p. 826, 2022.

[40] S. Verma, X. Lu, S. Ma, R. I. Masel and P. J. A. Kenis, "The effect of electrolyte composition on the electroreduction of CO2 to CO on Ag based gas diffusion electrodes," *Physical Chemistry Chemical Physics,* vol. 18, p. 7075, 2016.

[41] T. Burdyny and W. A. Smith, "CO2 reduction on gas-diffusion electrodes and why catalytic performance must be assessed at commercially-relevant conditions," *Energy & Environmental Science,* vol. 12, p. 1442, 2019.

[42] M. G. Kibria, J. P. Edwards, C. M. Gabardo, C.-T. Dinh, A. Seifitokaldani, D. Sinton and E. H. Sargent, "Electrochemical CO2 reduction into Chemical Feedstocks: From Mechanistic Electrocatalysis Models to System Design," *Advanced Materials,* vol. 31, 2019.

[43] N. P. Brandon and D. J. Brett, "Engineering porous materials for fuel cell applications," *Philosophical Transactions of The Royal Society A,* vol. 364, 2006.

[44] NIST Chemistry WebBook, NIST Standard Reference Database Number 69, "Carbon Dioxide," [Online]. Available: https://webbook.nist.gov/cgi/cbook.cgi?ID=C124389&Units=SI&Mask=10#Refs. [Accessed 22 04 2023].

[45] M. Mathias, J. Roth, J. Fleming and W. Lehnert, "Diffusion media materials and characterisation," in *Handbook of Fuel Cells – Fundamentals, Technology and Applications*, vol. 3, Wiley, 2003.

[46] H. Rabiee, L. Ge, X. Zhang, S. Hu, M. Li and Z. Yuan, "Gas diffusion electrodes (GDEs) for electrochemical reduction of carbon dioxide, carbon monoxide, and dinitrogen to value-added products: a review," *Energy & Environmental Science,* vol. 14, p. 1959, 2021.

[47] J. Becker, C. Wieser, S. Fell and K. Steiner, "A multi-scale approach to material modeling of fuel cell diffusion media," *International Journal of Heat and Mass Transfer,* vol. 54, pp. 1360-1368, 2011.

[48] R. Hussain, J. H. Blank and N. O. Elbashir, "Modeling the Fixed-Bed Fischer-Tropsch Reactor in Different Reaction Media," in *12th International Symposium on Process Systems Engineering and 25th European Symposium on Computer Aided Process Engineering*, Copenhagen, Denmark, 2015.

[49] M. P. Dudukovic, "Frontiers in Reactor Engineering," *Science,* vol. 325, no. 5941, pp. 698-701, 2009.

[50] P. Silvestroni, Fondamenti di Chimica, Roma: Libreria Eredi Virgilio Veschi, 1968.

[51] G. D. Wehinger, M. Ambrosetti, R. Cheula, Z.-B. Ding, M. Isoz, B. Kreitz, K. Kuhlmann, M. Kutscherauer, K. Niyogi, J. Poissonnier, R. Réocreux, D. Rudolf, J. Wagner, R. Zimmermann, M. Bracconi, H. Freund, U. Krewer and M. Maestri, "Quo vadis multiscale modeling in reaction engineering? – A perspective," *Chemical Engineering Research and Design,* vol. 184, pp. 39-58, 2022.

[52] S. Rebughini, M. Bracconi, A. G. Dixon and M. Maestri, "A hierarchical approach to chemical reactor engineering: an application to micro packed bed," *Reaction Chemistry & Engineering,* vol. 3, pp. 25-33, 2018.

[53] A. G. Dixon and B. Partopour, "Computational Fluid Dynamics for Fixed Bed Reactor Design," *Annual Review ofChemical and Biomolecular Engineering,* vol. 11, pp. 109-130, 2020.

[54] M. Maestri and A. Cuoci, "Coupling CFD with detailed microkinetic modeling in heterogeneous catalysis," *Chemical Engineering Science,* vol. 96, pp. 106-117, 2013.

[55] M. Bracconi, "Intensification of catalytic reactors: A synergic effort of Multiscale Modeling, Machine Learning and Additive Manufacturing," *Chemical Engineering & Processing: Process Intensification* , vol. 181, p. 109148, 2022.

[56] M. Maestri, "Escaping the trap of complication and complexity in multiscale microkinetic modelling of heterogeneous catalytic processes," *Chemical Communications,* vol. 53, p. 10244, 2017.

[57] M. Bracconi, M. Maestri and A. Cuoci, "In Situ Adaptive Tabulation for the CFD Simulation of Heterogeneous Reactors Based on Operator-Splitting Algorithm," *AIChE Journal,* vol. 63, no. 1, pp. 95-104, 2017.

[58] M. Salsiccioli, M. Stamatakis, S. Caratzoulas and D. G. Vlachos, "A review of multiscale modeling of metal-catalyzed reactions: Mechanism development for complexity and emergent behavior," *Chemical Engineering Science,* vol. 66, pp. 4319-4355, 2011.

[59] S. Rebughini, A. Cuoci and M. Maestri, "Hierarchical analysis of the gas-to-particle heat and mass transfer in micro packed bed reactors," *Chemical Engineering Journal,* vol. 289, pp. 471-478, 2016.

[60] M. Bracconi, M. Ambrosetti, M. Maestri, G. Groppi and E. Tronconi, "A fundamental investigation of gas/solid mass transfer in open-cell foams using a combined experimental and CFD approach," *Chemical Engineering Journal,* vol. 352, pp. 558-571, 2018.

[61] R. Flückiger, S. A. Freunberger, D. Kramer, A. Wokaun, G. G. Scherer and F. N. Büchi, "Anisotropic, effective diffusivity of porous gas diffusion layer materials for PEFC," *Electrochimica Acta,* vol. 54, pp. 551-559, 2008.

[62] J. Becker, R. Flückiger, M. Reum, F. N. Büchi, F. Marone and M. Stampanoni, "Determination of Material Properties of Gas Diffusion Layers: Experiments and Simulations Using Phase Contrast Tomographic Microscopy," *Journal of The Electrochemical Society,* vol. 156, no. 10, pp. B1175-B1181, 2009.

[63] M. M. Daino and S. G. Kandlikar, "3D phase-differentiated GDL microstructure generation with binder and PTFE distributions," *International Journal of Hydrogen Energy,* vol. 37, no. 6, pp. 5180-5189, 2012.

[64] Z. Tayarani-Yoosefabadi, D. Harvey, J. Bellerive and E. Kjeang, "Stochastic microstructural modeling of fuel cell gas diffusion layers and numerical determination of transport properties in different liquid water saturation levels," *Journal of Power Sources,* vol. 303, pp. 208-221, 2016.

[65] M. El Hannach and E. Kjeang, "Stochastic Microstructural Modeling of PEFC Gas Diffusion Media," *Journal of The Electrochemical Society,* vol. 161, no. 9, pp. F951-F960, 2014.

[66] V. P. Schulz, J. Becker, A. Wiegmann, P. P. Mukherjee and C.-Y. Wang, "Modeling of Two-Phase Behavior in the Gas Diffusion Medium of PEFCs via Full Morphology Approach," *Journal of The Electrochemical Society,* vol. 154, no. 4, pp. B419-B426, 2007.

[67] R. Thiedmann, F. Fleischer, C. Hartnig, W. Lehnert and V. Schmidt, "Stochastic 3D modeling of the GDL structure in PEMFCS based on thin section detection," *Journal of The Electrochemical Society,* vol. 155, no. 4, pp. B391-B399, 2008.

[68] S. Simaafrookhteh, M. Shakeri, M. Baniassadi and A. A. Sahraei, "Microstructure Reconstruction and Characterization of the Porous GDLs for PEMFC Based on Fibers Orientation Distribution," *Fuel Cells,* vol. 18, no. 2, pp. 160-172, 2018.

[69] J. Hinebaugh, J. Gostick and A. Bazylak, "Stochastic modeling of polymer electrolyte membrane fuel cell gas diffusion layers – Part 2: A comprehensive substrate model with pore size distribution and heterogeneity effects," *International Journal of Hydrogen Energy,* vol. 42, no. 24, pp. 15872-15886, 2017.

[70] F. Kubannek, T. Turek and U. Krewer, "Modeling Oxygen Gas Diffusion Electrodes for Various Technical Applications," *Chemie Ingenieur Technik,* vol. 91, no. 6, pp. 720-733, 2019.

[71] C. Delacourt and N. John, "Mathematical Modeling of CO2 Reduction to CO in Aqueous Electrolytes," *Journal of The Electrochemical Society,* vol. 157, pp. B1911-B1926, 2010.

[72] L.-C. Weng, A. T. Bell and A. Z. Weber, "Towards membrane-electrode assembly systems for CO2 reduction: a modeling study," *Energy & Environmental Science,* vol. 12, p. 1950, 2019.

[73] M. Löffelholz, J. Osiewacz, A. Lüken, K. Perrey, A. Bulan and T. Turek, "Modeling electrochemical CO2 reduction at silver gas diffusion electrodes using a TFFA approach," *Chemical Engineering Journal,* vol. 435, p. 134920, 2022.

[74] R. Kas, A. G. Star, K. Yang, T. Van Cleve, K. C. Neyerlin and W. A. Smith, "Along the Channel Gradients Impact on the Spatioactivity of Gas Diffusion Electrodes at High Conversions during CO2 Electroreduction," *ACS Sustainable Chemistry & Engineering,* vol. 9, pp. 1286-1296, 2021.

[75] E. W. Lees, B. A. W. Mowbray, F. G. L. Parlane and C. P. Berlinguette, "Gas diffusion electrodes and membranes for CO2," *Nature Reviews Materials,* vol. 7, pp. 55-64, 2022.

[76] M. Jouny, W. Luc and F. Jiao, "General Techno-Economic Analysis of CO2 Electrolysis Systems," *Industrial & Engineering Chemistry Research,* vol. 57, pp. 2165-2177, 2018.

[77] D. A. G. Bruggeman, "Berechnung verschiedener physikalischer Konstanten von heterogenen Substanzen. I. Dielektrizitätskonstanten und Leitfähigkeiten der

Mischkörper aus isotropen Substanzen," *Annalen der Physik,* vol. 416, no. 7, pp. 636-664, 1935.

[78] B. Tjaden, S. J. Cooper, D. J. L. Brett, D. Kramer and P. R. Shearing, "On the origin and application of the Bruggeman correlation for analysing transport phenomena in electrochemical systems," *Current Opinion in Chemical Engineering,* vol. 12, pp. 44-51, 2016.

[79] MIT Libraries, "Distinctive Collection Spotlights, Electricity, The Voltaic Pile," MIT, [Online]. Available: https://libraries.mit.edu/collections/vail-collection/topics/electricity/the-voltaic-pile/#:~:text=The%20voltaic%20pile%2C%20invented%20by,his%20experiments%20on%20frog%20legs.. [Accessed 30 04 2023].

[80] P. Mazzoldi, M. Nigro and C. Voci, Fisica Volume 2, Edises, 2001.

[81] E. Hall, "On a New Action of the Magnet on Electric Currents," *American Journal of Mathematics,* vol. 2, 1879.

[82] Wikipedia, "Daniell Cell," Wikimedia, 13 03 2023. [Online]. Available: https://en.wikipedia.org/wiki/Daniell_cell. [Accessed 01 05 2023].

[83] P. Atkins and J. De Paula, Physical Chemistry, Oxford, New York: Oxford university press, 2006.

[84] M. Devengenzo, "Standard Electrodes," LibreTexts Chemistry, [Online]. Available: https://chem.libretexts.org/Bookshelves/Analytical_Chemistry/Supplemental_Modules_(Analytical_Chemistry)/Electrochemistry/Electrodes/Standard_Hydrogen_Electrode. [Accessed 01 05 2023].

[85] P. Atkins and J. De Paula, "Chapter 7.8 Standard potentials," in *Physical Chemistry*, Oxford, New York, Oxford University Press, 2006, pp. 222-223.

[86] G. Jerkiewicz, "Standard and Reversible Hydrogen Electrodes: Theory, Design, Operation, and Applications," *ACS Catalysis,* vol. 10, pp. 8409-8417, 2020.

[87] C. H. Hamann, A. Hamnett and W. Vielstich, Electrochemistry, Weinheim: Wiley-VCH, 2007.

[88] A. J. Bard and L. R. Faulkner, Electrochemical Methods, New York: Wiley, 2001.

[89] R. B. Bird, W. E. Stewart and E. N. Lightfoot, Transport Phenomena, New York: Wiley, 1960.

[90] D. Stroud, "The effective medium approximations: Some recent developments," *Superlattices and Microstructures* , vol. 23, no. 3/4, pp. 567-573, 1998.

[91] OpenSCAD, "OpenSCAD The Programmers Solid 3D CAD Modeller," 05 2010. [Online]. Available: https://openscad.org/index.html. [Accessed 04 06 2023].

[92] J. Schindelin, I. Arganda-Carreras, E. Frise, V. Kaynig, M. Longair, T. Pietzsch, S. Preibisch, C. Rueden, S. Saalfeld, B. Schmid, J.-Y. Tinevez, D. J. White, V. Hartenstein, K. Eliceiri, P. Tomancak and A. Cardona, "Fiji: an open-source platform for biological-image analysis," *Nature Methods,* vol. 9, pp. 676-682, 2012.

[93] D. Legland, I. Arganda-Carreras and P. Andrey, "MorphoLibJ: integrated library and plugins for mathematical morphology with ImageJ," *Bioinformatics,* vol. 32, no. 22, pp. 3532-3534, 2016.

[94] R. Haase, L. A. Royer, P. Steinbach, D. Schmidt, A. Dibrov, U. Schmidt, M. Weigert, N. Maghelli, P. Tomancak, F. Jug and E. W. Myers, "CLIJ: GPU-accelerated image processing for everyone," *Nature Methods,* vol. 17, pp. 5-6, 2020.

[95] P. Chhikara, "Understanding Morphological Image Processing and Its Operations," Medium, 30 03 2022. [Online]. Available: https://towardsdatascience.com/understanding-morphological-image-processing-and-its-operations-7bcf1ed11756. [Accessed 16 05 2023].

[96] Wikipedia, "Somma di Minkowski," Wikimedia , [Online]. Available: https://it.wikipedia.org/wiki/Somma_di_Minkowski. [Accessed 04 06 2023].

[97] Wikipedia, "Minkowski addition," Wikimedia, [Online]. Available: https://en.wikipedia.org/wiki/Minkowski_addition. [Accessed 17 06 2023].

[98] MathWorks, "Types of Morphological Operation," The MathWorks, Inc., 2023. [Online]. Available: https://www.mathworks.com/help/images/morphological-dilation-and-erosion.html. [Accessed 16 05 2023].

[99] S. Didari, A. Asadi, Y. Wang and T. A. L. Harris, "Modeling of composite fibrous porous diffusion media," *International Journal of Hydrogen Energy,* vol. 39, no. 17, pp. 9375-9386, 2014.

[100] L. Xiao, Z. Yin, M. Bian, N. Bevilacqua, R. Zeis, J. Yuan and P.-C. Sui, "Microstructure reconstruction using fiber tracking technique and pore-scale simulations of heterogeneous gas diffusion layer," *International Journal of Hydrogen Energy,* vol. 47, no. 46, pp. 20218-20231, 2022.

[101] B. Münch and L. Holzer, "Contradicting Geometrical Concepts in Pore Size Analysis Attained with Electron Microscopy and Mercury Intrusion," *Journal of the American Ceramic Society,* vol. 91, no. 12, pp. 4059-4067, 2008.

[102] B. Münch, "Xlib," ImageJ Docs, 12 2021. [Online]. Available: https://imagej.net/plugins/xlib/#pore-size-distribution. [Accessed 17 05 2023].

[103] E. J. Garboczi and D. P. Bentz, "Digitez Simulation of Mercury Intrusion Porosimetry," *Advances in Cementitious Materials,* vol. 16, pp. 365-379, 1991.

[104] Anton Paar Wiki, "Mercury Intrusion Porosimetry Basics: Measuring Pores in Solids," Anton Paar, [Online]. Available: https://wiki.anton-paar.com/it-it/mercury-intrusion-porosimetry-basics-measuring-pores-in-solids/. [Accessed 18 05 2023].

[105] H. Jasak, A. Jemcov and Z. Tuković, "OpenFOAM: A C++ Library for Complex Physics Simulations," in *International Workshop on Coupled Methods in Numerical Dynamics*, Dubrovnik, Croatia, 2007.

[106] OpenFOAM , "Mesh generation witht the snappyHexMesh utility," OpenFOAM User Guide, [Online]. Available: https://www.openfoam.com/documentation/user-guide/4-mesh-generation-and-conversion/4.4-mesh-generation-with-the-snappyhexmesh-utility. [Accessed 28 05 2023].

[107] W. J. Drugan and J. R. Willis, "A micromechanics-based nonlocal constitutive equation and estimates of representative volume element size for elastic composites," *Journal of The Mechanics and Physics of Solids,* vol. 44, no. 4, pp. 497-524, 1996.

[108] M. Bracconi, M. Ambrosetti, M. Maestri, G. Groppi and E. Tronconi, "A fundamental analysis of the influence of the geometrical properties on the effective thermal

conductivity of open-cell foams," *Chemical Engineering & Processing: Process Intensification,* vol. 129, pp. 181-189, 2018.

[109] J. Koestel, M. Larsbo and N. Jarvis, "Scale and REV analyses for porosity and pore connectivity measures in undisturbed soil," *Geoderma,* vol. 366, p. 114206, 2020.

[110] Y. Bachmat and J. Bear, "Macroscopic Modelling of Transport Phenomena in Porous Media. 1: The Continuum Approach," *Transport in Porous Media ,* vol. 1, pp. 213-240, 1986.

[111] D. Zhang, R. Zhang, S. Chen and W. E. Soll, "Pore scale study of flow in porous media: Scale dependency, REV, and statistical REV," *Geophysical Research Letters,* vol. 27, no. 8, pp. 1195-1198, 2000.

[112] P. A. García-Salaberri, I. V. Zenyuk, A. D. Shum, G. Hwang, M. Vera, A. Z. Weber and J. T. Gostick, "Analysis of representative elementary volume and through-plane regional characteristics of carbon-fiber papers: diffusivity, permeability and electrical/thermal conducitivity," *International Journal of Heat and Mass Transfer,* vol. 127, pp. 687-703, 2018.

[113] P. Virtanen, R. Gommers, T. E. Oliphant, M. Haberland, T. Reddy, D. Cournapeau, E. Burovski, P. Peterson, W. Weckesser, J. Bright, S. J. Van Der Walt, M. Brett, J. Wilson, K. J. Millman, N. Mayorov, A. R. J. Nelson, E. Jones, R. Kern, C. J. Carey, I. Polat, Y. Feng, E. W. Moore and J. VanderPlas, "SciPy 1.0: fundamental algorithms for scientific computing in Python," *Nature Methods,* vol. 17, pp. 261-272, 2020.

[114] ImageJ Docs, "Particle Analysis," ImageJ, [Online]. Available: https://imagej.net/imaging/particle-analysis. [Accessed 05 06 2023].

[115] L. Xiao, L. Zhu, C. Clökler, A. Grünzweig, F. Wilhelm, J. Scholta, R. Zeis, Z.-G. Shen, M. Luo and P.-C. Sui, "Experimental validation of pore-scale models for gas diffusion layers," *Journal of Power Sources,* vol. 536, p. 231515, 2022.

[116] W. Yoshimune, S. Kato, M. Inagaki and S. Yamaguchi, "A simple method to measure through-plane effective gas diffusivity of a gas diffusion layer for polymer electrolyte fuel cells," *International Journal of Heat and Mass Transfer,* vol. 191, p. 122887, 2022.

[117] I. V. Zenyuk, D. Y. Parkinson, L. G. Connolly and A. Z. Weber, "Gas-diffusion-layer structural properties under compression via X-ray tomography," *Journal of Power Sources,* vol. 328, pp. 364-376, 2016.

[118] N. Zamel, X. Li and J. Shen, "Numerical estimation of the effective electrical conductivity in carbon paper diffusion media," *Applied Energy,* vol. 93, pp. 39-44, 2012.

[119] G. Dagan, Flow and Transport in Porous Formations, Berlin: Springer-Verlag, 1989.

[120] R. Lemlich, "A Theory for the Limiting Conductivity of Poilyhedral Foam at Low Density," *Journal of Colloid and Interface Science,* vol. 64, no. 1, pp. 107-110, 1978.

[121] N. Zamel, X. Li and J. Shen, "Correlation for the Effective Gas Diffusion Coefficient in Carbon Paper Diffusion Media," *Energy Fuels,* vol. 23, pp. 6070-6078, 2009.

[122] P. A. García-Salaberri, J. T. Gostick, G. Hwang, A. Z. Weber and M. Vera, "Effective diffusivity in partially-saturated carbon-fiber gas diffusion layers: Effect of local saturation and application to macroscopic continuum models," *Journal of Power Sources,* vol. 296, pp. 440-453, 2015.

[123] R. H. Perry, D. W. Green and M. Z. Southard, Perry's Chemical Engineers' Handbook. 9th Edition, New York: McGraw-Hill Education, 2018.

[124] S. H. Fogler, Elements of Chemical Reaction Engineering, Philadelphia, PA: Prentice Hall, 1999.

[125] I. Aldama, V. Barranco, M. Kunowsky, J. Ibañez and J. M. Rojo, "Contribution of Cations and Anions of Aqueous Electrolytes to the Charge Stored at the Electric Electrolyte/Electrode Interface of Carbon-Based Supercapacitors," *The Journal of Physical Chemistry C,* vol. 121, no. 22, pp. 12053-12062, 2017.

[126] C. Graves, S. D. Ebbesen, M. Mogensen and K. S. Lackner, "Sustainable hydrocarbon fuels by recycling CO2 and H2O with renewable or nuclear energy," *Renewable and Sustainable Energy Reviews,* vol. 15, pp. 1-23, 2011.

[127] N. Khajeh-Hosseini-Dalasm, T. Sasabe, T. Tokumasu and U. Pasaogullari, "Effects of polytetrafluoroethylene treatment and compression on gas diffusion layer

microstructure using high-resolution X-ray computed tomography," *Journal of Power Source,* vol. 266, pp. 213-221, 2014.

[128] M. M. Mezedur and M. Kaviany, "Effect of Pore Structure, Randomness and Size on Effective Mass Diffusivity," *AIChe Journal,* vol. 48, no. 1, pp. 15-24, 2022.

Appendix A: Laplace equation residual

The Laplace equation has to be solved for the scalar field ϕ:

$$\nabla^2\phi = 0$$

Using a second order differencing scheme the Laplace equation brings to a set of algebraic equations whose form is the following (for the volume cell i,j,k):

$$\frac{\phi_{i+1,j,k} - 2\phi_{i,j,k} + \phi_{i-1,j,k}}{\Delta x^2} + \frac{\phi_{i,j+1,k} - 2\phi_{i,j,k} + \phi_{i,j-1,k}}{\Delta y^2} + \frac{\phi_{i,j,k+1} - 2\phi_{i,j,k} + \phi_{i-1,j,k-1}}{\Delta z^2} = R_{i,j,k}$$

where due to the discretization error the residual $R_{i,j,k}$ for the correspondent volume cell has been introduced. The total residual, accounting for the error in the solution of the algebraic equation in all the domain cells, is obtained by summing R over all the cells:

$$R_{tot} = \sum_i \sum_j \sum_k R_{i,j,k}$$

Additionally the residual can also be normalized to make it independent of the scale of problem being analyzed. Defining n as the normalization factor, the convergence condition is written as:

$$\frac{1}{n} R_{tot} < tolerance$$

where in our case a tolerance value of 10^{-12} has been used.

Appendix B: Simulation campaign for the transport properties correlations

Table 11 Results of simulation campaign conducted to extract the effective transport properties correlations from the stochastic reconstruction of GDLs.

N° sample	ε	n Fibers	Fiber diameter [μm]	BVF	TPC	IPC	TPD	IPD
Data set obtained varying n Fibers								
1	0.7	21	8	40%	0.0865	0.2171	0.3174	0.3840
2	0.72	20	8	40%	0.0822	0.1990	0.3199	0.3912
3	0.74	18	8	40%	0.0639	0.1793	0.3859	0.4505
4	0.76	17	8	40%	0.0556	0.1620	0.4578	0.4874

5	0.78	15	8	40%	0.0437	0.1400	0.5416	0.5118
6	0.80	13	8	40%	0.0288	0.1216	0.5679	0.5563
Data set obtained varying the Fiber diameter								
7	0.70	18	9.2	40%	0.0847	0.2082	0.3624	0.3883
8	0.72	18	8.6	40%	0.0799	0.1927	0.3953	0.4091
9	0.74	18	8	40%	0.0639	0.1793	0.3859	0.4505
10	0.76	18	7.5	40%	0.0587	0.1601	0.4222	0.4809
11	0.78	18	6.6	40%	0.0528	0.1423	0.4801	0.5085
12	0.80	18	6	40%	0.0355	0.1374	0.4554	0.5430

Data set obtained by changing BVF								
13	0.70	18	8	48.46%	0.0735	0.2042	0.3678	0.3870
14	0.72	18	8	43.2%	0.0672	0.1902	0.3797	0.4235
15	0.74	18	8	38.29%	0.0639	0.1793	0.3859	0.4505
16	0.76	18	8	34.84%	0.0622	0.1598	0.4383	0.4838
17	0.78	18	8	27.72%	0.0580	0.1389	0.4593	0.4998
18	0.80	18	8	20.4%	0.0310	0.1297	0.5524	0.5828

List of Figures

List of Tables

List of Abbreviations

Abbreviation	Meaning	Page
GDL	Gas diffusion layer	11
HDI	Human development index	14
HHV	Higher heating value	16
IEA	International energy agency	17
PES	Potential energy surface	20
OER	Oxygen evolution reaction	27
GDE	Gas diffusion electrode	29
IEM	Ionic exchange membrane	29
KPI	Key performance indicator	29
CL	Catalyst layer	30
PSD	Pore size distribution	32
SEM	Scanning electron microscope	33
PAN	Polyacrylonitrile	35
PTFE	Polytetrafluoroethylene	35
PRCFD	Particle resolved computational fluid dynamics	37
DFT	Density functional theory	39
μCT	Micro computed tomography	41
LBM	Lattice Boltzmann methods	42
EMA	Effective medium approximation	44
CO_2RR	CO_2 reduction reaction	46
SHE	Standard hydrogen electrode	56
RHE	Reversible hydrogen electrode	56
HER	Hydrogen evolution reaction	56
STL	Stereolithography	76
SE	Structuring element	79
BVF	Binder volume fraction	82
MIP	Mercury intrusion porosimetry	84
BSE	Back-scattered electron	84
TP	Through-plane	89

IP	In-plane	89
REV	Representative elementary volume	92

Acknowledgements

I have to express my gratitude to many people without whom this work would have not been possible.

At first I would like to thank my thesis advisor, the Professor Matteo Maestri for the guidance he provided me throughout my year spent in the lab. Thanks for the professionalism and the availability, both inside and outside the context of the Master's thesis. I hope we will have the chance to collaborate again in the future.

Then I have to express my gratitude for the co-advisor of my thesis, Dr. Kaustav Niyogi. Thanks to Kaustav I learnt the basis of how research has to be conducted. I improved my capabilities in the systematical analysis of scientific problems and in the formulation of reasonable explanations for physical and chemical phenomena observed. Kaustav has also been a point of reference in different other aspect, and I will never forget his teachings. Finding another mentor like him will undoubtedly be a challenging task. Thanks for your patience Kaustav, and thanks for having taught me the rules of the infinite game.

Remaining in the academic environment I would like to extend my gratitude to Professor Mauro Bracconi for his meticulous guidance and his expertise in the field of numerical simulations, which formed the foundation of my work. In this sense I also would like to thank the PhD students of the LCCP group, in particular Daniele Micale, Davide Cafaro and Claudio Ferroni. Their support throughout my time in Bovisa has been important in overcoming many challenges that emerged during my work.

Outside of the university I have to be grateful to my family. Thank you Bruno Patrizia Oreste and Gaia for being my safe place, everyday, since the first day.

Finally, I would like to express my gratitude to all my friends, those I have here in Milan, in Rome and those who are in Abruzzo. Thank you for having brought joy and lightness to my life.